Stony Brook University

OFFICIAL COPY

The official electronic file of this thesis or dissertation is maintained by the University Libraries on behalf of The Graduate School at Stony Brook University.

© All Rights Reserved by Author.

Development of New Generation of Perovskite Based Noble Metal/Semiconductor Photocatalysts for Visible-light-driven Hydrogen Production

A Dissertation Presented

by

Peichuan Shen

to

The Graduate School

in Partial Fulfillment of the

Requirements

for the Degree of

Doctor of Philosophy

in

Materials Science and Engineering

Stony Brook University

August 2013

Copyright by
Peichuan Shen
2013

Stony Brook University

The Graduate School

Peichuan Shen

We, the dissertation committee for the above candidate for the

Doctor of Philosophy degree, hereby recommend

acceptance of this dissertation.

Alexander Orlov – Dissertation Advisor
Assistant Professor, Department of Materials Science and Engineering

Jonathan Sokolov – Chairperson of Defense
Professor, Department of Materials Science and Engineering

Clive Clayton
Leading Professor, Department of Materials Science and Engineering

Dong Su
Associate Scientist, Center of Functional Nanomaterials, Brookhaven National Laboratory

This dissertation is accepted by the Graduate School

Charles Taber
Interim Dean of the Graduate School

Abstract of the Dissertation

Development of Perovskite Structure and Noble Metal/Semiconductor Photocatalysts for Visible-light-driven Hydrogen Production

by

Peichuan Shen

Doctor of Philosophy

in

Materials Science and Engineering

Stony Brook University

2013

In recent decades, semiconductor photocatalysis has attracted a growing attention as a possible alternative to existing methods of hydrogen production, hydrocarbon conversion and organic compound oxidation. Many types of photocatalysts have been developed and tested for photocatalytic applications. However, most of them do not have notable activity in visible light region, which limits their practical applications. Development of photocatalysts, which can be activated by visible light provides a promising way forward to utilize both UV and visible portions of solar spectrum. In this thesis, two main methods to advance visible light driven photocatalysis, such as bandgap modification through doping and co-catalyst development, are investigated. The photocatalysts studied in this thesis included CdS and $SrTiO_3$, which were extensively investigated and characterized.

Rhodium doped strontium titanate was synthesized through different preparation methods. The synthesized samples have been investigated by various characterization techniques including XRD, TEM, STEM, XPS and UV-Vis spectroscopy. The effect of preparation conditions, such as doping concentration, calcination temperature and pH have been investigated and optimized. In addition, the photocatalytic activities for hydrogen production of the samples synthesized by different preparation methods were also studied. Among the preparation methods, polymerizable complex (PC) method was found to be the most effective synthesis method for $SrTiO_3$: Rh. The

samples prepared by PC method had higher photocatalytic activity as compared to that of samples synthesized by solid state reaction method and hydrothermal method. The reasons might be attributed to more effective doping and higher surface area. The results of this work suggest that PC method can also be applied to develop other perovskite materials for photocatalytic applications.

Co-catalyst development for enhancement of photocatalytic hydrogen production is also described in this dissertation. Noble metal nanoparticles have been proved to be effective co-catalysts due to their unique physical and chemical properties. Au and Pt nanoparticles with different sizes were synthesized and deposited on CdS. Sub-nanometer Au and Pt were found to be promising co-catalysts for photocatalytic hydrogen production reaction. Specifically, sub-nm Au and sub-nm Pt nanoparticles were found to enhance the photocatalytic activity in hydrogen production of CdS by 35 and 15 times respectively. Other noble metal co-catalysts, such as Ru, Pd and Rh were also deposited on CdS and their photocatalytic activities were investigated.

Additionally, a novel chamber for photocatalytic reactions was developed as a part of this dissertation. The reaction chamber has several unique features allowing different reactions and measurements. The reactor was proved to be suitable for future projects in photocatalysis such as photocatalytic CO_2 conversion into hydrocarbons.

Table of Contents

List of Figures

Figure

List of Tables

Table

List of Abbreviation

wt. %	Weight %
at. %	Atom %
BG	Bandgap
CB	Conduction band
VB	Valence band
XRD	X-ray diffraction
TEM	Transmission electron microscopy
EDX	Energy-dispersive X-ray spectrometry
SEM	Scanning electron microscopy
STEM	Scanning transmission electron microscopy
XPS	X-ray photoelectron spectroscopy
GC	Gas chromatography
TCD	Thermal conductivity detector
Au NPs	Au nanoparticles
PC method	Polymerizable complex method
SSR method	Solid state reaction method
NHE	Normal hydrogen electrode
PEC	Photoelectrochemical
UV	Ultraviolet

Vis	Visible
QE	Quantum efficiency
TON	Turnover number

Acknowledgements

I would first like to thank my advisor, Professor Alexander Orlov, who has been a fantastic mentor throughout my studies in Stony Brook University. He was always supportive when I proposed new research topics and ideas. He also gave me the opportunity to attend many conferences, which significantly benefited my academic career. I would also like to thank my committee members, Prof. Clive Clayton, Prof. Jonathon Sokolov and Dr. Dong Su. The comments provided during my preliminary exam, on the written dissertation and during the thesis defense have been extremely helpful and have resulted in a significantly improved dissertation.

I would thank my collaborators. Prof. Peter Khalifah and Dr. Limin Wang from Department of Chemistry helped me when I first started my study in photocatalysis. The discussion with them broadened my understanding in my research topics. Prof. Michael White guided me on surface analysis of various samples related to my research. His patience and passion for research really inspired me on my academic career. I also want to thank Prof. White's student, John C. Lofaro Jr for XPS analysis and useful discussion. Many thanks go to Prof. John Praise group, especially William Worner, for his help on sample preparation and XRD analysis. I would like to thank many scientists and researchers in Center of Functional Nanomaterials at Brookhaven National Laboratory. I want to thank Dr. Dong Su, not only for his analysis and interpretation of all the electron microscopy images and the supports to my research, but also for being a good friend. I also worked with Dr. Yan Li, I want to thank her for all the computational work provided and research methodologies developed.

I would like to thank all the current members of Prof. Orlov group for their help. I want to thank Shen Zhao, Girish Ramakrishnan, Qiyuan Wu, Raul Tejerina and James Ging. We have been experienced a lot of meetings, group activities, fun and as well as hard time. I also want to thank all my friends that I met during my graduate school.

Finally, I want to give all my thanks to my family. Without their love and encouragement, I would not be able to finish my study. Thank you for always being there to share my excitement, joys as well as the challenges.

Publications

P. Shen, S. Zhao, D. Su, Y. Li, A. Orlov, Outstanding activity of sub-nm Au clusters for photocatalytic hydrogen production, *Applied Catalysis B: Environmental* 126 (2012) 153-160

P. Shen, J. C. Lofaro Jr, W. R. Woerner, M. G. White, A. Orlov, Photocatalytic activity of hydrogen evolution over Rh doped $SrTiO_3$ prepared by polymerizable complex method, *Chemical Engineering Journal*, 223 (2013) 200-208

P. Shen, Q. Wu, S. Zhao, S. Xiong, Y. Li, M. G. White, A. Orlov, Development of sub-nm Pt clusters as co-catalyst for photocatalytic hydrogen production, *Chemical Communication*, in preparation

Additional publications related to this work

S. Zhao, G. Ramakrishnan, **P. Shen**, D. Su, A. Orlov, The first experimental demonstration of the beneficial effects of sub-nanometer platinum particles for photocatalysis, *Chemical Engineering Journal*, 217 (2013) 266-272.

Presentations arising from this work

P. Shen, Q. Wu, J. C. Lofaro Jr, W. R. Woerner, D. Su, A. Orlov, (2013) Development of novel nanostructured biomimetic ceramics for sustainable energy applications. American Chemical Society. Indianapolis, IN.

P. Shen, J. C. Lofaro Jr, W. R. Woerner, M. G. White, (2013) Photocatalytic activity of hydrogen evolution over Rh doped $SrTiO_3$ prepared by polymerized complex method. American Chemical Society. New Orleans, LA.

P. Shen, S. Zhao, D. Su, Y. Li, A. Orlov, (2012) Development of highly efficient noble metals co-catalysts for solar hydrogen production on semiconductor surfaces. American Chemical Society. Philadelphia, PA.

P. Shen, S. Zhao, G. Ramakrishnan, D. Su, Y. Li, A. Orlov. (2012) Understanding extraordinary activity of sub-nm noble metal particles of different sizes in hydrogen production: photocatalytic and DFT studies. 19th international conference on photochemical conversion and storage of solar energy. Pasadena, CA.

P. Shen, S. Zhao, G. Ramakrishnan, D. Su, Y. Li, A. Orlov, (2012) Development of a new generation of sub-nanometer noble metals catalysts for environmental and energy applications. Metro New York Catalysis Society - 2012 Annual Symposium. ExxonMobil, Annandale, NJ.

P. Shen, S. Zhao, A. Orlov. (2011) Utilizing Au11 clusters for photocatalytic water splitting reactions. American Chemical Society. Denver, CO.

Additional presentation related to this work

Y. Li, S. Zhao, **P. Shen**, D. Su, A. Orlov, (2012) Enhanced photocatalytic H_2 production by sub-nanometer Au nanoparticles, American Physical Society, Boston, MA

Chapter 1

Prologue

1.1 Summary

It is a well known fact that the global energy consumption increases every year. Among the limited energy production methods, fossil fuel still domains the current energy market. However, since fossil fuels are neither renewable nor eco-friendly, development of renewable energy options has become an urgent necessity. Utilizing solar energy has several notable advantages, such as being renewable, clean and abundant. More specifically, using solar energy to produce hydrogen is attracting more attention as recent advances in catalysts synthesis and increases in quantum efficiency of the reaction are advancing this approach into being a notable method for renewable hydrogen production. In this chapter, such technology is discussed and the outline of this dissertation is detailed.

1.2 Global energy production

Over the past decades, world population has increased significantly. In 1990, the world population was 5.27 billion. This number was refreshed to 7.087 billion on March 12, 2012, reported by the United States Census Bureau (USCB) [1]. Another projection reported by the United Nations Population Fund indicated that the world population reached 7 billion benchmark on October 31, 2011 [2]. Table 1-1 lists the world population in the past and estimates in the future based on different population growing rates.

Table 1-1 World population (thousands) in the past and in the future (1990-2040) [3].

Year	Medium variant	High variant	Low variant	Constant-fertility variant
1990	5306425			
1995	5726239			
2000	6122770			
2005	6506649			
2010	6985889			
2015	7284296	7350953	7217275	7323598

2020	7656528	7832370	7480225	7772757
2025	8002978	8316521	7689135	8231506
2030	8321380	8776486	7867332	8700336
2035	8611867	9225306	8006642	9191971
2040	8874041	9679064	8096725	9722061

Since the world population is still growing rapidly, the demand for energy is becoming an ever more critical challenge. According to U. S. Energy Information Administration Report in 2011 [4], the total global energy production in 2009 was approximately equivalent to 503.8 quadrillion BTU while 82.6 % of the primary energy production came from fossil fuels (oil, coal and natural gas), as shown in Figure 1-1. At the same time, renewable sources accounted for only 5%, with the majority coming from hydroelectric generation (Figure 1-2).

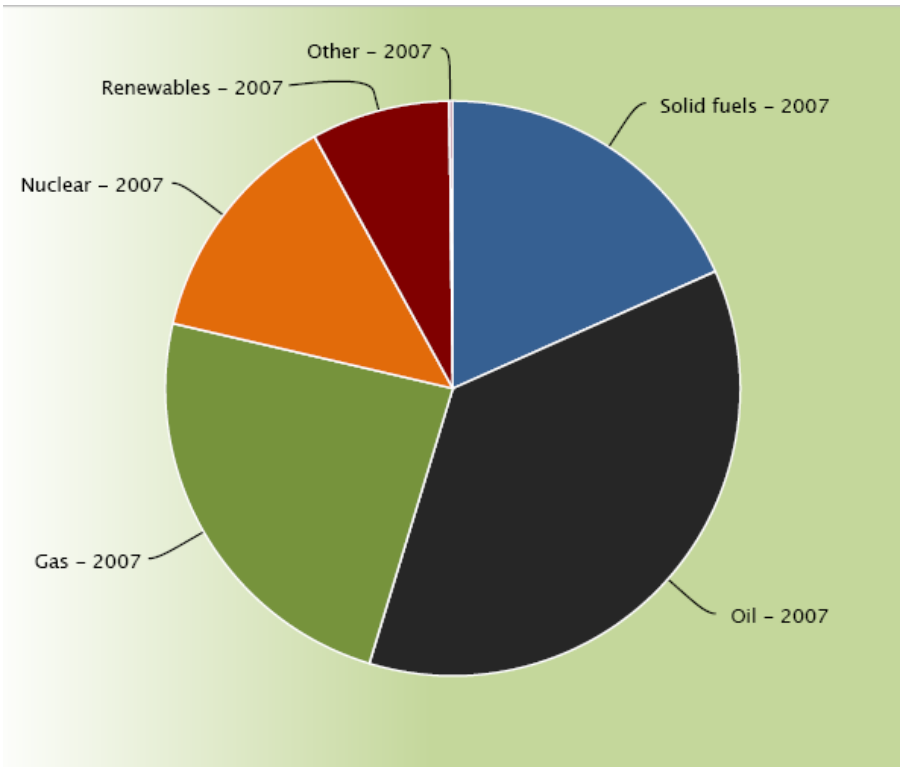

Figure 1-1 Distribution of world energy production from various sources in 2009.

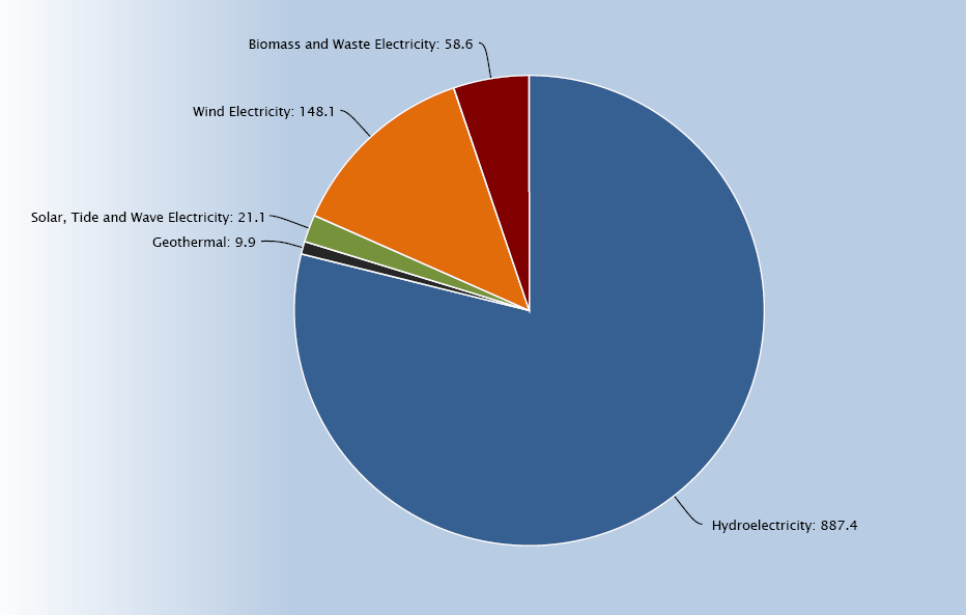

Figure 1-2 Distribution of world energy production from renewable energy in 2009 (installed capacity, million kilowatts).

Estimation and prediction of the energy demand by several different institutions, including (IEA), the U.S. Energy Information Administration (EIA), and the revealed that the estimates of remaining non-renewable worldwide energy resources vary [4-7]. Among them, the total remaining fossil fuels (oil and natural gas) is about 0.4 YJ (1 YJ = 10^{24} J) and the available nuclear fuel such as uranium exceeding 2.5 YJ. These reports also pointed out if the estimates of reserves of methane clathrates are accurate, and a series of technically challenges can be solved, the total remaining fossil fuel (oil, natural gas and methane clathrates) will be ranged from 0.6 to 3 YJ. Fossil fuel ultimately came from the solar energy. For comparison purpose, the total energy flux from the sun to the surface of the earth is about 3.8 YJ/yr, dwarfing all non-renewable resources.

1.3 Fossil fuel and renewable energy usage

Many estimate research reported that if the world consume energy at a constant rate of 30 TW (1 TW= 10^{12} W) per year, the proven reserves of conventional fossil fuels can supply the world for another several centuries. For example, it was believed that, there are approximately 50–150 years of proven crude oil and natural gas reserves as well as an additional 200–500 years of natural gas reserves if oceanic methane clathrates are included if the world consumes energy based on 1998 rates of consumption according to the *World Energy Assessment* reported by the

United Nations Development Programme [8]. Furthermore, the report indicated 1,000 to 2,000 years of other fossil fuel resources (coal, oil shale and tar sands).

Even though prediction revealed the conventional fossil fuels has the potential to provide us energy for another several decades or centuries, continuing our current energy policy which relies on fossil fuels will result in several potential problems. First, as the oil prices are keeping going up, the question about whether we can afford expensive fossil fuel remains unanswered. The oil price is estimated to be approximately $125-200 per barrel by the year 2035, which rockets from only $80 per barrel in 2008 [4]. If inflation is taken into account, the increase rate will be more than 56-150%. Oil price is becoming an economic burden for every oil dependent industry.

Second, continuing heavy usage of fossil fuels has the potential to deteriorate the environment. Combustion of conventional fossil fuels emits carbon dioxide, which is also considered one of the major green house gases. Human activity has increased the amount of greenhouse gases in the atmosphere since industrial revolution. The concentration of carbon dioxide increased from 315 ppmv in 1960 to 386 ppmv in 2010. The concentration change rate has achieved highest increase rate during the last 800,000 years [9]. In 2011, the estimated global CO_2 emission from fossil fuels was 34.8 billion tonnes, increased CO_2 emission in 1990 by 54% [10].

Global warming is a major environmental problem. To cap carbon emissions at current rates, and prevent future increases as global energy consumption continues to increase, it is projected that at least 10 TW of energy will need to be provided by carbon-neutral sources by 2050 [11]. Furthermore, to limit global temperature rise, 75% decline in carbon emissions in industrial countries is needed by 2050, that requires that a total of 30 TW of energy is produced by carbon-neutral sources, based on some carbon reduction plans [12, 13]. Although fossil fuels are the main energy production source currently, it is clear that gradually reduce our heavy reliance on fossil fuels is very necessary from environmental protection perspectives. Development of renewable energy (which is carbon neutral) is becoming one of the most important challenges over the world.

Renewable energy is defined as natural resources including sunlight, wind, rain, tides, and geothermal heat, which are renewable (naturally replenished) [14]. Based on current reports and research, in 2010, about 16% of global final energy consumption comes from renewables, with

10% coming from traditional biomass, which is mainly used for heating, and 3.4% from hydroelectricity. New renewables (small hydro, modern biomass, wind, solar, geothermal, and biofuels) accounted for another 2.8% and are growing very rapidly [15]. The share of renewables in electricity generation is around 19%, with 16% of global electricity coming from hydroelectricity and 3% from new renewable [16]. Among various advantages of renewable energy, replenishment is the most important label. At the same time, renewable energy is suited to generate electricity in remote areas where are far away from the main power grid.

Through technological development and benefits of mass production, renewable energy is getting cheaper. Various reports estimated by 2030, the cost of renewable energy will be comparable with conventional fossil fuels [4, 17].

1.4 Solar energy and solar fuel

Solar energy is one of major sources of renewable energy, which utilizes the energy from the solar radiation to generate electricity or to convert it into chemical energy. Solar energy includes various options such as solar heat, photovoltaics and biomass. The energy contained in two hours sunlight is much higher the total world energy consumption for the entire year of 2008 (5 exajoules), given that the average energy rate from the sunlight striking the earth's surface is 120,000 TW [11]. The International Energy Agency projected that solar power could provide "a third of the global final energy demand after 2060, while CO_2 emissions would be reduced to very low levels [14].

However, although solar energy has various advantages including being renewable, clean, abundant and suitable for remote areas, the practical applications are still limited. Currently only approximately 1.5% of global energy production comes from a solar source, and most of it is through biomass [18]. Numerous organizations within the academic universities, federal agencies, non-profit organizations and commercial sectors are conducting advanced research in the field of solar energy utilization, in both laboratory and pilot plant scale. For example, the maximum energy output of biomass could be 5-10 TW, given that mankind can efficiently utilize the surface of the earth to grow energy crops (e.g. elephant grass) [19]. Biomass can further be turned into ethanol which enables a cellulosic ethanol future [20-22]. However, achieving this future still remains a challenge and needs continuous research. Photovoltaic is another interesting practical example to directly turn solar light into electricity. Many solar photovoltaic power stations have been built all over the world. The energy production from photovoltaic power has

reached 67.4 GW in 2011 [23] and is accelerating based on several projections [24-26]. Nevertheless, the drawbacks of photovoltaic energy cannot be neglected. One problem with PV energy is that a separate storage technology is required to overcome natural temporal and spatial variations of solar flux, and it is not clear what the best options are [27-29]. Significant increases in PV and storage efficiency, and even large improvements in cost reduction, are required to make the technology practical, but this is certainly an avenue worth serious pursuit.

Another particularly promising solar energy technology, and the focus of this dissertation, is the direct production of solar fuel (hydrogen) using sunlight, which is widely known as artificial photosynthesis [30, 31]. Hydrogen has been considered as an alternative energy carrier which has several distinct advantages including environment friendly, high energy density and being renewable. However, the primary hydrogen production method used in current market is through steam reforming, which consumes non-renewable sources to produce hydrogen (Equation 1-1 and 1-2).

$$CH_4 + H_2O \rightleftharpoons CO + 3H_2 \quad (1\text{-}1)$$

$$CO + H_2O \rightarrow CO_2 + H_2 \quad (1\text{-}2)$$

Currently, only 5 % of commercial hydrogen is produced renewably, primarily via water electrolysis with renewable electrical power source. However, the high expense of electrolysis limits its use to produce hydrogen. Thus, there is a raising demand to find an alternative method to produce hydrogen. Artificial photosynthesis mimics nature to produce hydrogen, more specifically, by using a photocatalyst that absorbs sunlight and converts the solar energy into chemical energy through photoelectrochemical reactions (the specific physical processes are discussed in Chapter 2). Figure 1-3 illustrated the basic idea of this artificial photosynthesis. The net effect is that solar energy can be used to directly transform a low energy compound such as water into a high energy one (hydrogen). Solar to hydrogen energy conversion could provide energy storage in a form easily used for stationary power generation, aviation, land transportation, heating and in remote areas.

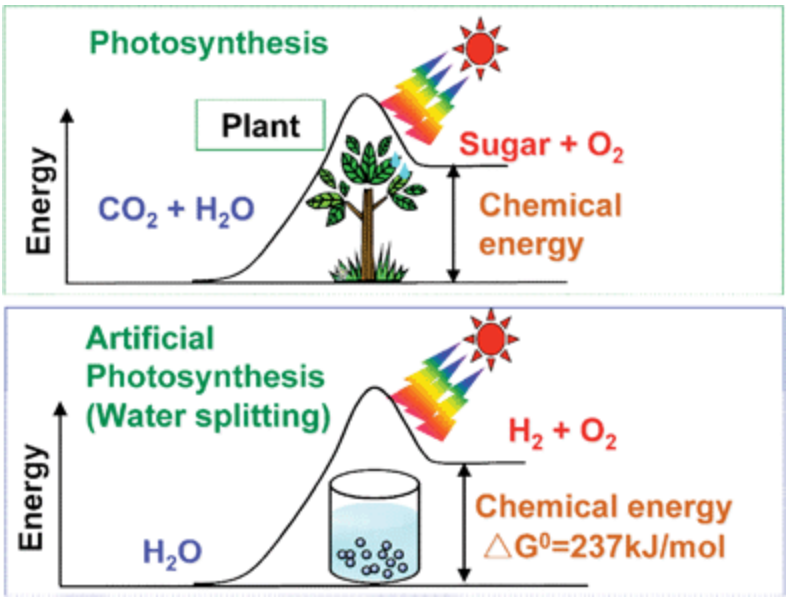

Figure 1-3 Natural photosynthesis versus artificial photosynthesis from ref [31].

1.5 Scope of the dissertation

Using solar light and semiconductors to split water for hydrogen and oxygen production, which is also known as water splitting, has been known for several decades. This phenomenon is called the Fujishima-Honda effect [32], which will be discussed in details in Chapter 2. Although mankind has spent decades of efforts to investigate this technology, the progress is still slow and the technology is not widely applicable. The rate of hydrogen production remains low due to lack of efficient semiconductor for water splitting.

More recent progress on water splitting photocatalysts includes perovskite structure materials development to increase photocatalytic activity. These efforts aimed at cation and anion doping to tailor the bandgaps of perovskite structure materials to efficiently utilize visible light for water splitting. Moreover, many reports on metal nanoparticles also demonstrated that the interaction between the metal nanoparticles and the conventional semiconductors is essential for photocatalytic activity enhancement. The detailed mechanisms for photocatalytic activity are not well known and need to be further investigated. In this dissertation, bandgap modification and co-catalyst development for photocatalytic activity enhancement are investigated. Experimental, computational and theoretical tools are used to investigate the underlying physical mechanisms. We demonstrate the synthesis and evaluation of the new co-catalysts as well as perovskite materials for photocatalytic hydrogen production. Additionally, we propose models that capture

and predict their behavior, which can be used to guide the design of optimized composite photocatalysts, especially when used in conjunction with other advances being pursued in parallel in other fields (for example, advanced synthesis techniques).

1.6 Structure of the dissertation

This short introduction is followed by Chapter 2 “Photocatalyic Water Splitting and Hydrogen Evolution”. Chapter 2 introduces the physical phenomena and mechanism of photocatalytic hydrogen and oxygen formation, which is called the Fujishima-Honda effect [11]. The chapter focuses on the photocatalytic splitting of water to form hydrogen and oxygen and photocatalytic hydrogen evolution. A list of requirements for development of an effective and efficient semiconductor photocatalysts is discussed. Finally, the chapter introduces major strategies for photocatalysts design.

Chapter 3 "Development of Photocatalysts Based on the Perovskite Structure for Photocatalytic Water Splitting and Hydrogen Evolution" demonstrates the perovskite structure development for photocatalytic water splitting and hydrogen evolution. The physical and chemical properties of the perovskite structure are introduced. The chapter also includes various bandgap modification techniques to shift the absorbance edge of perovskite structure to visible region, followed by major sample preparation techniques for perovskite structure photocatalyst. Finally, as a representative of perovskite, $SrTiO_3$ is introduced and the recent advances on $SrTiO_3$ are summarized.

Chapter 4 "Development of Noble Metal Nanoparticles for Photocatalytic Applications" introduces several import effects of noble metal nanoparticles such as quantum confinement effect and surface plasmon resonance effect. A brief introduction of noble metal nanoparticles is followed by major synthesis methods of noble metal nanoparticles. The applications of noble metal nanoparticles and important factors to affect their activities are presented.

Chapter 5 “Characterization, Experimental and Computational Methods” contains detailed descriptions of various methods used throughout the thesis (primarily Chapters 6, 7 and 8). The chapters themselves contain short methods sections, which present crucial information regarding methodology specific to that particular chapter, as well as references to specific sections within this chapter for further information.

Chapter 6 “$SrTiO_3$: Rh Catalyst Preparation and Characterization” includes the preparation and characterization methods of $SrTiO_3$: Rh prepared by SSR method, hydrothermal method and

PC method. The results obtained through various characterization methods are presented here. Chemical composition, particle size, morphology and electronic states are investigated and discussed. Moreover, a comparison of the electronic states of $SrTiO_3$: Rh synthesized by different preparation methods is also shown here.

Chapter 7 " Photocatalytic Hydrogen Production over $SrTiO_3$: Rh" follows by chapter 6 and presents the activity investigations of $SrTiO_3$: Rh prepared by SSR method, hydrothermal method and PC method. The effects of Rh dopant concentration, calcination temperature, pH as well as different synthesis methods are studied. These results provide comprehensive understandings of different preparation parameters.

Chapter 8 "Photocatalytic Hydrogen Evolution of Sub Nanometer Noble Metal Loaded CdS" gives an overview of sub nanometer noble metal loaded on CdS. This chapter includes the synthesis, characterization and photocatalytic activity testings of sub nanometer Au/CdS and sub nanometer Pt/CdS.

Chapter 9 "Conclusions Remarks and Future Projections" summarizes the mechanistic insights and results gained throughout the previous chapters. A few important factors that continue to challenge the future application of this technology are discussed. Potential strategies to improve overall efficiencies, problems and progress in large-scale implementation of the technology, and some basic economic considerations regarding broad use of water splitting as an energy production technology are presented.

References

[1] U.S. Census Bureau, World POP clock projection, 2012.

[2] BBC, Population seven billion: UN sets out challenges, October 26, 2011.

[3] United Nations. Dept. of Economic and Social Affairs. Population Division., World population prospects : the 2006 revision, United Nations, New York, 2007.

[4] J.R. Plunkett, Energy Information Administration, International energy outlook and projections, Nova Science Publishers, Hauppauge, NY, 2011.

[5] I.E. Agency, Annual report on energy research, Development and demonstration, Organisation for Economic Co-operation and Development, Paris.

[6] U.S. Energy Information Administration, Energy data report, U.S. Dept. of Energy, Washington, D.C.

[7] E.E. Agency, Energy and environment report 2008, European Environment Agency-Office for Official Publications of the European Communities, Copenhagen, Denmark, Luxembourg, 2008.

[8] J. Goldemberg, United Nations Development Programme, United Nations. Department of Economic and Social Affairs., World Energy Council., World energy assessment: Energy and the challenge of sustainability, United Nations Development Programme, New York, NY, 2000.

[9] EPA, Recent climate change: Atmosphere changes, in, United States Environmental Protection Agency, Climate Change Science Program, 2009.

[10] S.L. Piao, A. Ito, S.G. Li, Y. Huang, P. Ciais, X.H. Wang, S.S. Peng, H.J. Nan, C. Zhao, A. Ahlstrom, R.J. Andres, F. Chevallier, J.Y. Fang, J. Hartmann, C. Huntingford, S. Jeong, S. Levis, P.E. Levy, J.S. Li, M.R. Lomas, J.F. Mao, E. Mayorga, A. Mohammat, H. Muraoka, C.H. Peng, P. Peylin, B. Poulter, Z.H. Shen, X. Shi, S. Sitch, S. Tao, H.Q. Tian, X.P. Wu, M. Xu, G.R. Yu, N. Viovy, S. Zaehle, N. Zeng, B. Zhu, The carbon budget of terrestrial ecosystems in East Asia over the last two decades, Biogeosciences, 9 (2012) 3571-3586.

[11] D. Gust, T.A. Moore, A.L. Moore, Solar fuels via artificial photosynthesis, Accounts Chem Res, 42 (2009) 1890-1898.

[12] S. Jebaraj, S. Iniyan, A review of energy models, Renew Sust Energ Rev, 10 (2006) 281-311.

[13] J. Li, Towards a low-carbon future in China's building sector - A review of energy and climate models forecast, Energ Policy, 36 (2008) 1736-1747.

[14] REN21, Renewables 2011: Global status report, 2011, pp. 17, 18.
[15] M.Z. Jacobson, M.A. Delucchi, A Path to Sustainable Energy by 2030, Sci Am, 301 (2009) 58-65.
[16] M.Z. Jacobson, M.A. Delucchi, Providing all global energy with wind, water, and solar power, Part I: Technologies, energy resources, quantities and areas of infrastructure, and materials, Energ Policy, 39 (2011) 1154-1169.
[17] M.A. Delucchi, M.Z. Jacobson, Providing all global energy with wind, water, and solar power, Part II: Reliability, system and transmission costs, and policies, Energ Policy, 39 (2011) 1170-1190.
[18] U.S. Department of Energy, Annual energy outlook; Technical report, in, 2011.
[19] N.S. Lewis, D.G. Nocera, Powering the planet: Chemical challenges in solar energy utilization, P Natl Acad Sci USA, 103 (2006) 15729-15735.
[20] J.T. Landry, The clean tech revolution: The next big growth and investment opportunity, Harvard Bus Rev, 85 (2007) 34-34.
[21] L.R. Lynd, J.H. Cushman, R.J. Nichols, C.E. Wyman, Fuel ethanol from cellulosic biomass, Science, 251 (1991) 1318-1323.
[22] A.E. Farrell, R.J. Plevin, B.T. Turner, A.D. Jones, M. O'Hare, D.M. Kammen, Ethanol can contribute to energy and environmental goals, Science, 311 (2006) 506-508.
[23] E.P.I. Association, Market Report 2011, in, 2012.
[24] E. Figueres, G. Garcera, J. Sandia, F. Gonzalez-Espin, J.C. Rubio, Sensitivity study of the dynamics of three-phase photovoltaic inverters with an LCL grid filter, Ieee T Ind Electron, 56 (2009) 706-717.
[25] Q. Li, P. Wolfs, A review of the single phase photovoltaic module integrated converter topologies with three different DC link configurations, Ieee T Power Electr, 23 (2008) 1320-1333.
[26] W.H. Li, X.N. He, Review of nonisolated high-step-up DC/DC converters in photovoltaic grid-connected applications, Ieee T Ind Electron, 58 (2011) 1239-1250.
[27] S.J. Chiang, K.T. Chang, C.Y. Yen, Residential photovoltaic energy storage system, Ieee T Ind Electron, 45 (1998) 385-394.

[28] C.R. Lung, S. Miyake, H. Kakigano, Y. Miura, T. Ise, T. Momose, H. Hayakawa, DC-linked hybrid generation system with an energy storage device including photovoltaic generation and gas engine cogeneration for residential houses, Electr Eng Jpn, 182 (2013) 29-46.
[29] J.M. Pearce, Expanding photovoltaic penetration with residential distributed generation from hybrid solar photovoltaic and combined heat and power systems, Energy, 34 (2009) 1947-1954.
[30] J.R. Bolton, Solar photoproduction of hydrogen: A review, Sol Energy, 57 (1996) 37-50.
[31] A. Kudo, Y. Miseki, Heterogeneous photocatalyst materials for water splitting, Chemical Society Reviews, 38 (2009) 253-278.
[32] A. Fujishima, K. Honda, Electrochemical photolysis of water at a semiconductor electrode, Nature, 238 (1972) 37-38.

Chapter 2

Photocatalytic Water Splitting and Hydrogen Evolution

2.1 Introduction

It is believed that the amount of energy that reaches the earth surface from the sun on a yearly basis is more than 3×10^{24} joules, or more specifically, more than 10,000 times than that of the world energy consumption in 2008 [1]. The enormous amount of the solar light that falls on the surface of the earth can be very beneficial for renewable clean energy production [2]. However, effective and efficient utilization of solar energy depends on the availability of materials that can capture the energy from the sunlight and then convert it into heat, electricity or chemical energy.

Over the past several decades, many efforts have been focused on some conventional methods for solar energy conversion and utilization, such as solar thermal and photovoltaics. However, these techniques still have significant technical challenges which need to be overcome, such as limited capability to efficiently store energy over periods longer than a few hours [3].

Another alternative method to utilize solar energy is to convert solar energy into chemical energy. For example, there is a very promising method to produce hydrogen from water by using solar light (photocatalytic reactions) [4]. Hydrogen is regarded as the next-generation carrier and has significant potential to produce energy (through combustion or via the fuel cells) in a clean and sustainable manner [5, 6]. Additionally, solar to hydrogen energy conversion could provide energy storage in a form easily used for stationary power generation, aviation, land transportation, heating and in remote areas [7, 8].

2.2 Mechanism of semiconductor photocatalytic water splitting

Photocatalytic reactions are classified into two categories: "down-hill" and "up-hill" reactions [9]. Figure 2-1 illustrates the two categories photocatalytic reactions.

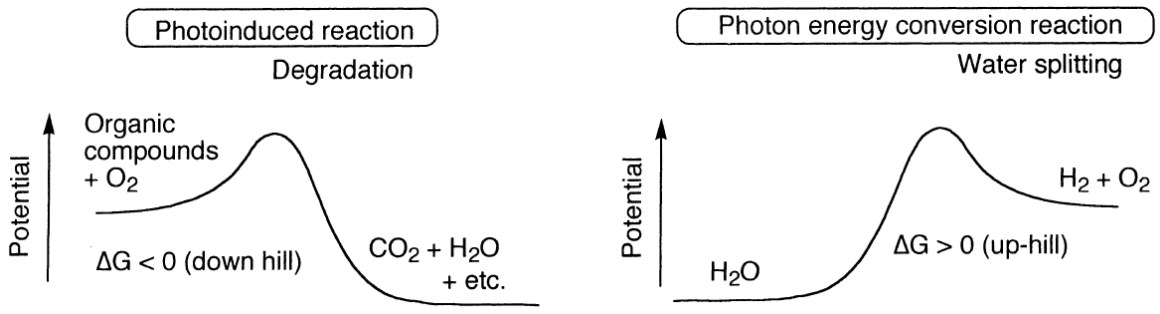

Figure 2-1 Types of photocatalytic reactions from ref [9].

Degradation reaction, for example, photo-oxidation of organic compounds, is commonly recognized as a down-hill reaction. The reaction proceeds irreversibly. In this reaction, a photocatalyst works as a trigger to produce O^{2-}, OH, and H^{+} as active species for the oxidation reaction at the initial stage. This type of reaction is regarded as a photo-induced reaction and has been extensively studied using a titanium dioxide photocatalyst [10]. Another category for photocatalytic reactions is “up-hill” reactions. Water splitting is a good example of this kind of reactions which is accompanied by a large positive change in Gibbs free energy. In this reaction, photon energy is converted into chemical energy (e.g. H_2). This reaction mimics a natural process, which is called artificial photosynthesis [11].

Photocatalytic water splitting over semiconductors has become one of the fastest growing interests in the recent decades [12-15]. Fujishima and Honda explored the possibilities for water splitting by using TiO_2 and Pt electrodes in 1971 [16]. The photocatalytic water splitting process was successfully demonstrated and their discovery was named as "Fujishima-Honda effect". Since then, many researchers have attempted to increase the quantum efficiency (QE, defined as the ratio between the number of reacted electrons and the number of incident photons) of this reaction [17-19]. However, a success in these efforts, especially in achieving decomposition of water into H_2 and O_2 in a stoichiometric amount with a high QE in visible light region, has not been discovered [20, 21].

How does the "Fujishima-Honda effect" work? In general, an effective photocatalyst requires the photon energy to be equal to or higher than the bandgap. When the photocatalyst is illuminated by the light, the absorption of the photons results in electrons excitement from the valence band to the conduction band, leaving behind an empty state in the valence band (also called a "hole", denoted by h^{+}). By this process, electron-hole pairs are formed [22]. The generated electron and hole drives the chemical process in a non-spontaneous (uphill) direction. For the water splitting reaction, water molecules are reduced by the electrons to form H_2 and oxidized by the holes to form O_2. This process can be presented via two half reactions at electrically opposite electrodes [23]:

$$2OH^- + 2h^+ \rightarrow H_2O + \frac{1}{2}O_2 \quad (2\text{-}1)$$

$$2H_2O + 2e^- \rightarrow H_2 + 2OH^- \quad (2\text{-}2)$$

Reaction (2-1) is an oxidation reaction that happens in the anode, reaction (2-2) is a reduction reaction that happens in the cathode. These reactions are referred to as half-reactions. The standard reduction potential (E^0) for water electrolysis is 1.23 eV at pH=0, measured under standard conditions (25 ℃, 1 atm, pH=7). However, the actual reduction potential is strongly dependent on the concentrations of H^+ and OH^- ions, reaction temperature and pressure. The Nernst Equation can be used to calculate the actual reduction potential (Equation 2-3).

$$E = E^0 - \frac{RT}{nF} \ln \left(\frac{C_{Ox}}{C_{Red}}\right) \quad (2\text{-}3)$$

In Equation 2-3, E is the actual reduction potential, E^0 is the standard reduction potential, R is the gas constant, T is the temperature, F is faraday constant, n is the number of the reacted electrons, and C_{Ox} and C_{Red} are the concentrations of oxidation and reduction species respectively. For photocatalytic reactions, temperature and pressure can be precisely controlled. Therefore, the actual reduction potential becomes pH dependent and can be calculated by Equation 2-4,

$$E = E^0 \pm 0.059\text{pH} \quad (2\text{-}4)$$

where "+" and "-" are used to calculate reduction half reaction and oxidation half reaction, respectively. Therefore, the actual reduction potential can be adjusted by pH. For instance, when pH=7, the reduction potential for the hydrogen evolution reaction is -0.42 eV and the reduction potential for the oxygen evolution reaction is 0.82 eV.

If we combine Equation 2-1 and 2-2 together, we can get overall water splitting reaction:

$$2H_2O + 2e^- + 2h^+ \rightarrow 2H_2 + 2OH^- \quad (2\text{-}5)$$

The overall water splitting reaction is the sum of the oxygen evolution and hydrogen evolution half reactions, as shown in Equation 2-5.

The Gibbs free energy required for overall water splitting is 237.1 kJ/mol at the standard temperature and pressure (25 ˚C, 1 atm) [24]. As discussed above, the minimum bandgap for a photocatalyst to drive the water splitting reaction is 1.23 eV [22, 25], corresponding to a wavelength of 1008 nm, which is located in the near infrared region, as illustrated in Figure 2-2.

This means a large proportion of the solar light spectrum has sufficient energy to separate an electron-hole pair and excite an electron from the valence band to the conduction band by a successful photocatalyst.

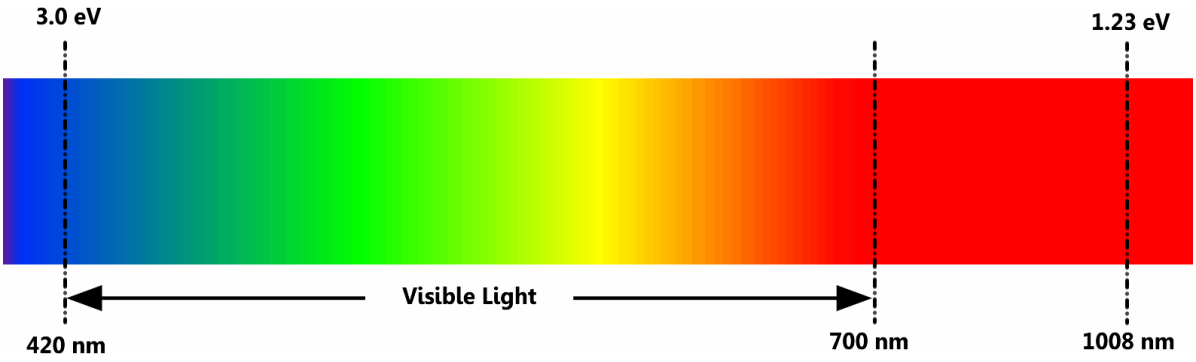

Figure 2-2 Solar light spectrum and the minimum bandgap for a successful photocatalyst for water splitting reaction.

However, water can absorb some parts of infrared light and make infrared light impractical to split water efficiently. To utilize visible light, the bandgap has to be narrower than 3.0 eV [4] (Figure 2-2).

The process of the water splitting reaction can be divided into three parts: (1) absorption of the photons and generation of the carriers, (2) separation and migration of the photo-generated carriers, (3) and the evolution of the surface reactions into hydrogen and oxygen. Proper bandgap is just one of the many necessary requirements to drive the water splitting reaction. Other factors, such as bandgap positions, charge separation and migration and surface chemical reactions also play very important roles in photocatalytic processes [26-28]. These properties are strongly affected by bulk properties of the material such as crystallinity and surface properties such as surface area and active reaction sites [29, 30].

First, to absorb the photons and to generate carriers, an effective photocatalyst needs to have proper bandgap and bandgap positions. The bottom level of the conduction band (CB) has to be more negative than the reduction potential of H^+/H_2 (0V vs. NHE), while the top level of the valence band (VB) has to be more positive than the oxidation potential of O_2/H_2O (NHE vs. 1.23v) [31, 32] (Figure 2-3). It is obvious that the bandgap of an effective photocatalyst must exceed 1.23 V, however, from the chemical kinetics point of view, the conduction band edge should be above the reduction potential by 0.4 to 0.8 eV, and the valence band edge should be

below the oxidation potential by 0.4 to 0.8 eV. Therefore, the minimum bandgap of practical photocatalysts is between 2.0 and 2.5 eV.

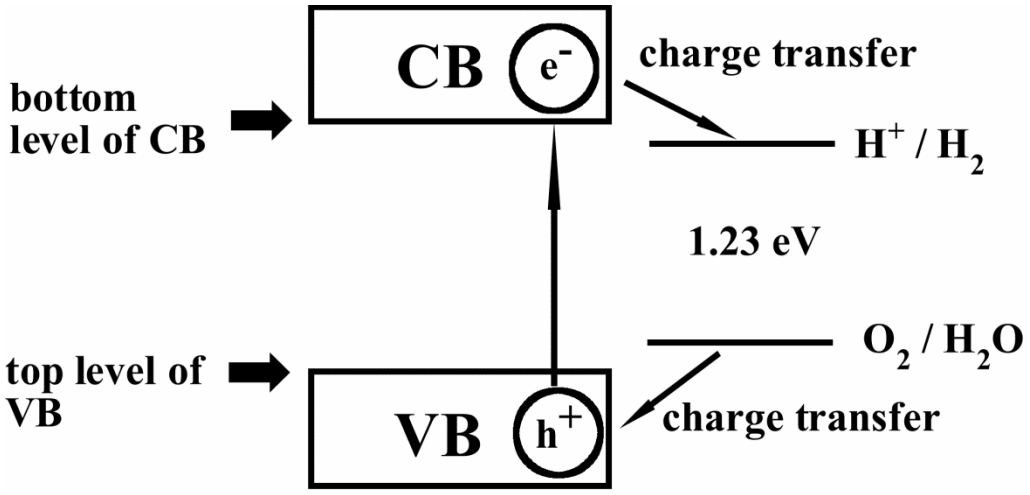

Figure 2-3 Bandgap position requirements for photocatalytic water splitting.

Second, carrier separation and migration are very important for photocatalytic water splitting reactions [33, 34]. The separated charges migrate to surface reaction sites and react with water. The recombination of electron-hole pairs suppresses the photocatalytic water splitting reaction. Crystallinity strongly affects the recombination. Photocatalysts with high crystalline quality have small amounts of defects. Because the defects act as trapping and recombination centers for photogenerated electrons and holes, they result in a decrease in photocatalytic activity.

After electron-hole pairs have evolved, charge carrier migration needs to be considered. The migration distances of photogenerated electrons and holes to reaction sites are based on the particle size of the photocatalyst. Nanoparticles have the advantage of having larger surface areas and shorter migration distances before reaching surface reaction sites for photogenerated charge carriers. When the particle size becomes smaller, the chance that a photogenerated charge carrier meets the boundaries and defects is lower, which results in a decreased probability of recombination. Moreover, the width of the space charge region of nanoparticles is narrower than that of bulk materials. The space charge region is the location where the photogenerated charge carriers are separated. A smaller space charge region has a lower potential drop for charge carriers, which results in a lower recombination rate.

Third, hydrogen and oxygen eventually evolve on the surface of the photocatalysts [35, 36]. Surface character (active sites) and quantity (surface area) strongly affect this step. The photo-generated electrons and holes will recombine with each other even if they carry thermodynamically sufficient potentials for water splitting, when the active sites for redox reactions do not exist on the surface. Therefore, surface chemical reactions play key roles in photocatalytic reactions. Co-catalyst loading increases the number of the active sites and decreases the activation energy for hydrogen and oxygen evolution, thus it is a commonly used method to modify the surface of the photocatalysts.

2.3 Water splitting systems

Water splitting reactions are investigated in two main categories of experimental setups: Photoelectrochemical (PEC) cell system and particle-based water splitting system [4, 11, 16, 37], as illustrated in Figure 2-4.

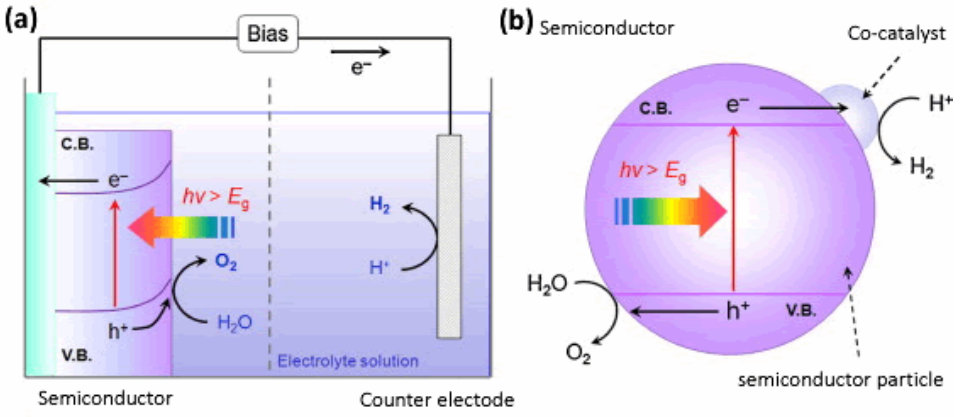

Figure 2-4 Experimental setups for water splitting reactions (Figure reproduced from reference [38]); (a) Photoelectrochemical cell system, (b) Particle-based water splitting system.

Using PEC cell for photocatalytic water splitting investigation has a very long history. It was first used by Fujishima and Honda, the pioneers for photocatalytic water splitting [16] (Figure 2-4 (a)). In their work, a TiO_2 electrode and a Pt counter electrode were connected through an external electrical circuit. After illuminating the system with light, O_2 was found in the TiO_2 electrode and H_2 was found in the Pt counter electrode. Since then, a lot of accomplishment was discovered in photocatalytic water splitting by using PEC [39-42]. In general, the working electrode is typically constructed of a semiconductor deposited on a conductive substrate and this

is connected electrically to a counter electrode (typically Pt). A reference electrode must also be employed in order to determine electric potentials on an absolute scale. PEC cell carries an outstanding advantage of relatively high efficiency because the photogenerated electrons and holes are separated to different electrodes spatially. This minimizes the possibility of photogenerated electron-hole pair recombination. Moreover, hydrogen and oxygen are evolved in cathode and anode, respectively, diminishing the back reaction of water formation.

The second way to perform water splitting is to directly suspend powdered photocatalysts in water or water/sacrificial reagents mixtures [43, 44] (Figure 2-4 (b)). Compared to PECs, this method is more straightforward and the cost of developing this configuration is lower. In principle, if a photocatalyst can separate electrons and holes efficiently and those electron-hole pairs can migrate to the surface without recombination, both hydrogen reduction and oxygen oxidation reactions can happen on the surface of the photocatalyst simultaneously. However, single component photocatalysts are generally not able to meet all of the necessary requirements for overall water splitting. It is common to introduce co-catalyst to facilitate the reactions. The role of the co-catalyst will be discussed in Chapter 2.4.2. Briefly, a co-catalyst can help to separate the charge carriers and prevent recombination and to improve the kinetics of the hydrogen evolution half-reaction, the oxygen evolution half-reaction, or both. The biggest drawback of a particulate system for photocatalytic water splitting is that it suffers from poor monitoring and controlling in terms of photocurrent and external potential bias, making understanding of the mechanism of the photocatalytic water splitting reactions more challenging [22, 37].

Chemical addictives are commonly used in both experimental configurations for photocatalytic water splitting. They work as electron or hole scavengers so that only one of the water splitting half reactions occurs at one time. This provide advantages to learn about the either hydrogen reduction or oxygen oxidation half reaction, though both are useful to investigate which half reaction determines the rate of overall water splitting reaction [45-47]. Moreover, sacrificial reagents can significantly increase the catalyst activity. The detailed discussion on chemical addictives can be found in Chapter 2.5.

2.4 Photocatalyst modification techniques to increase photocatalytic activity

Although photocatalytic water splitting phenomena has been discovered several decades ago, the process of commercialization is moving slowly. A limited number of current commercial

scale projects use ideas of photocatalysis which include sun-activated self-cleaning surfaces [48-51], UV-light induced purification and sterilization applications [52-54], etc. The reasons for the slow motion in commercialization can be attributed to renewable energy legislation imperfection, lacking of proper incentives and economical high cost [55]. Most importantly, the efficiency of the most successful photocatalyst at the current moment is still low and is not suitable for large scale applications. Thus, it is a must to develop highly efficient photocatalysts for photocatalytic water splitting reactions [4, 56].

To design a successful particle-based photocatalyst for water splitting reactions, five processes need to be considered [27, 57]:

1. Absorption of photons.
2. Formation of electron-hole pairs.
3. Recombination between photoexcited electrons and holes.
4. H_2 and O_2 evolution on the surface of the photocatalysts.
5. Stability of the photocatalysts.

Figure 2-5 illustrates the surface reactions during photocatalytic water splitting reaction of a particle-based system.

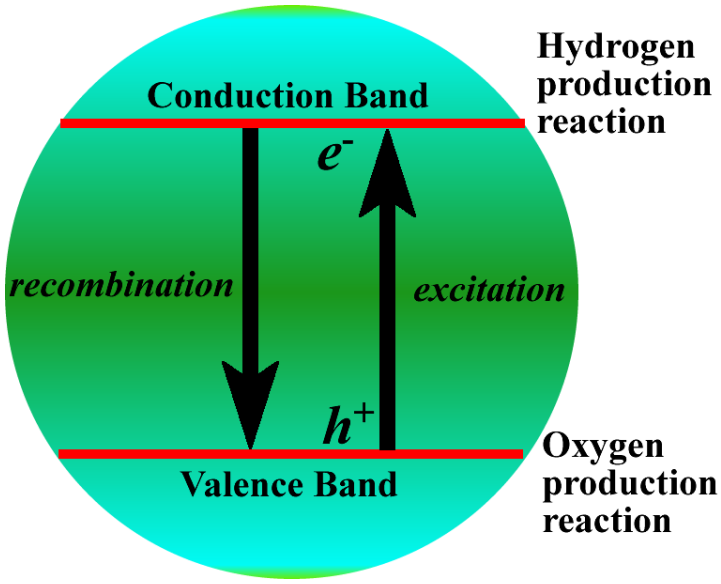

Figure 2-5 H_2 and O_2 evolution reactions in a typical water splitting cycle of a particle-based system.

In the five processes above, (1) (2) (3) are the most important points to make a photocatalyst work for water splitting under visible irradiation.

First, the bandgap of a working photocatalyst needs to be bigger than the minimum bandgap requirement for water splitting. In order to respond to visible light, the bandgap of the photocatalyst must be smaller than 3.0 eV. Moreover, the conduction and valence band positions should satisfy the energy requirements set by the reduction and oxidation potential, respectively. Second, a working photocatalyst needs to have good charge separation ability. After the electron-hole pairs appear, recombination needs to be prevented. Defect act as recombination centers resulting in a loss of the photocatalytic activity. Thus, defects need to be considered. Third, surface character (active sites) and quantity (surface area) are essential as even if the photogenerated electrons and holes possess sufficient thermodynamic potentials for water splitting, they will have to recombine with each other if the active sites for redox reactions do not exist on the surface. Therefore, the surface chemical reactions need to be taken into account.

In addition to the three processes described above, the stability of the developed photocatalyst needs to be considered. A lot of photocatalysts can drive a photocatalytic water splitting reaction for a short period of time. However, they are not chemically stable. They undergo corrosion and photocorrosion, and therefore lose photocatalytic activity quickly. These unstable photocatalysts can only be utilized to split water if they are well protected from degradation.

The following diagram (Figure 2-6) illustrates the bandgap positions of various semiconductor photocatalysts compared to the water splitting reaction bandgap position requirements which were discussed above. Some of these semiconductor photocatalysts will be discussed in details in the following chapters.

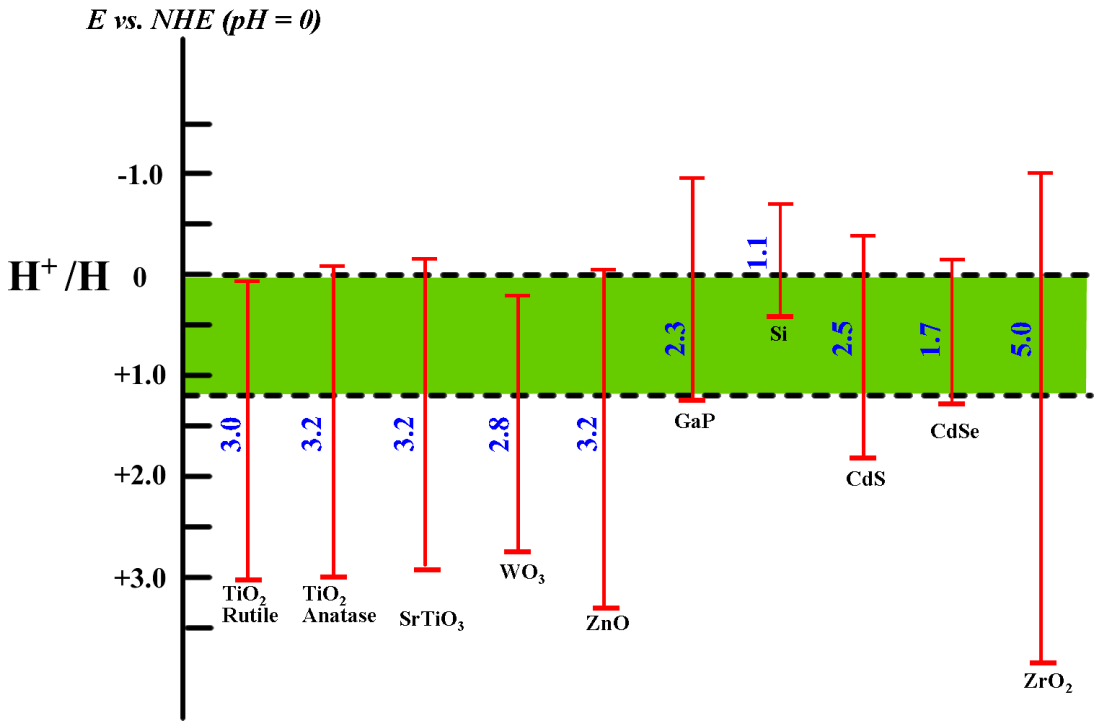

Figure 2-6 Bandgap and bandgap positions of various semiconductors.

Strategies for developing water splitting visible light driven photocatalysts can be various, but are mainly categorized into four methods [45, 58-60]:

1. Solid solution development.
2. Co-catalyst development.
3. Bandgap modification.
4. Composite photocatalyst development.

2.4.1 Solid solution method development and optimization

Energy structure can be controlled by formation of a solid solution between materials with wide and narrow bandgaps (Figure 2-7). This idea has been applied to develop various visible light-active photocatalysts, for example, Nb_2O_5-Bi_2O_3, Ga_2O_3-In_2O_3, $Sr_2Nb_2O_7$-$Sr_2Ta_2O_7$, etc [61-64]. Recently, GaN-ZnO and ZnO-$ZnGeN_2$ have exhibited the overall water splitting by visible light irradiation [56, 65]. One of the advantages of solid solution is that it often has more efficient absorption of visible light than that of doped wide-bandgap photocatalysts. Another advantage is that photo induced electrons and holes are efficiently transferred to the surface of the semiconductor through the continuous energy bands formed in a solid solution.

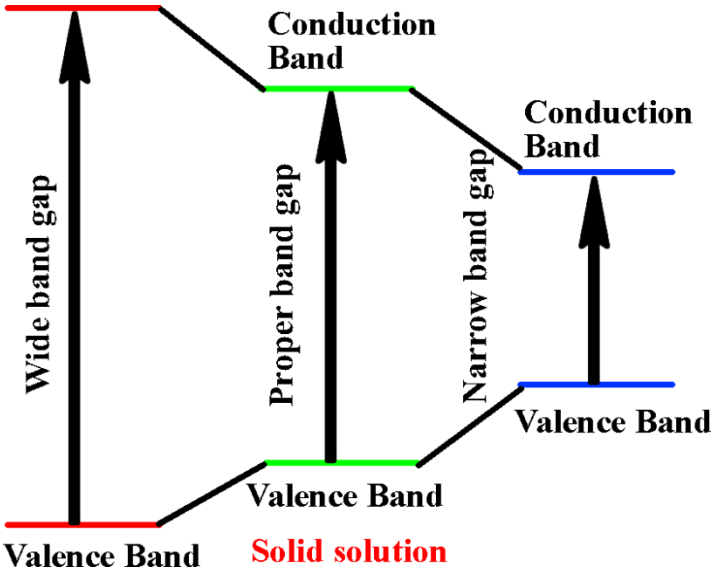

Figure 2-7 Schematic diagram of bandgap structure of solid solution materials.

2.4.2 Modification with co-catalysts

Co-catalyst can lower activation energy in a chemical reaction and serves as active sites for photocatalytic reactions. Noble metals, oxides and sulfides and core-shell structure can be used as effective and efficient co-catalysts (Figure 2-8).

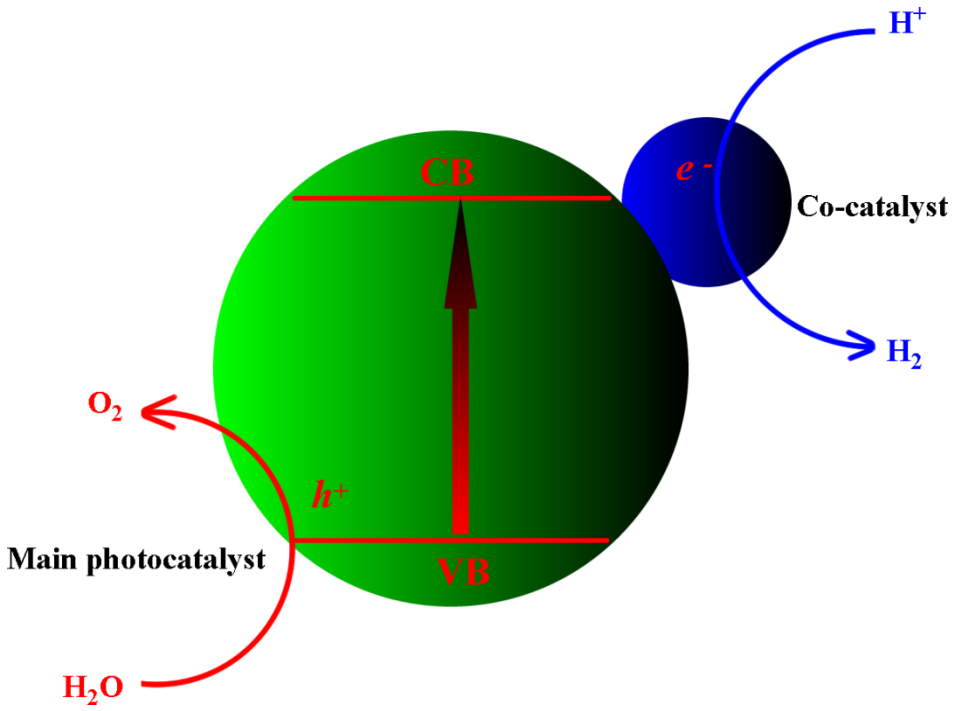

Figure 2-8 Schematic diagram of co-catalyst loading for photocatalytic water splitting.

Noble metals, including Pt [66, 67], Au [68-70], Pd [71, 72], and Rh [71, 73] have been reported to be very effective for enhancement of hydrogen yield. Noble metal/semiconductor heterogeneous photocatalyst can be obtained by randomly loading metallic nanoclusters onto the surface of semiconductor particles. The noble metal nanoclusters play an important role and enhance photocatalytic activity from three different perspectives. First, when noble metals are loaded on the semiconductor, a Schottky barrier can be formed. The Fermi levels of these noble metals are lower than that of semiconductor materials. As a result of the equilibrium alignment of the fermi level of the metal and semiconductor materials, the photo-excited electrons can be transferred from CB to noble metal particles deposited on the surface of the semiconductor, while photo-generated VB holes remain in the semiconductor [74, 75]. These activities greatly reduce the possibility of electron-hole recombination, resulting in more favorable photocatalytic reactions. Second, the noble metals can function as active sites and reduce the over potential for surface electrochemical reactions or gas evolution processes. Early example when Pt is deposited on TiO_2 surface, the H_2 production is significantly enhanced [76, 77] (Though TiO_2/Pt still shows low H_2 production). Recently, Au and Ru nanoparticles have been reported as efficient co-catalyst in creating active sites for H_2 evolution with much lower back-reaction rate between H_2 and O_2 to produce water in comparison to that with Pt nanoparticles [78, 79]. Third, the light absorption of semiconductor can be enhance through a plasmonic enhancement effect when noble metal/semiconductor heterostructure is formed [80]. The metallic nanostructure can strengthen the absorption of the semiconductor attached through two possible mechanisms. First, the metallic nanostructure can serve as scattering center and trap light propagating within the semiconductor materials, this increases the chance of photon-semiconductor interaction. Second, the optical excitation of metallic nanostructure can create local surface plasmon resonance (LSPR), that is, a coherent oscillation of the free electrons in resonance with the electrical field component of the incoming electromagnetic irradiation. LSPR can induce strong absorption of the electromagnetic energy, thereby enhance the semiconductor light absorption. It should be noted that although the loading of noble metal can reduce recombination to some extent, hydrogen production from pure water-splitting is difficult to achieve, because: (1) Recombination cannot be completely eliminated; (2) backward reaction of H_2 and O_2 to form H_2O is thermodynamically favorable. Therefore, electron donors or carbonate salts as well as other mediators are required to avoid the above listed problems (see Chapter 2.5).

Some metal oxide (eg. RuO_2, NiO) [32] , metal sulfide (eg. MoS_2) [81, 82] and core/shell structure (eg. Rh core/Cr_2O_3 shell) [22] can also work as effective co-catalyst to facilitate the surface electrochemical reactions. These co-catalysts improve the photocatalytic activity through enhanced charge separation and suppression of the recombination of photogenerated charge carriers. In addition, these co-catalysts can act as an outside layer to improve the stability of the photocatalyst. For example, Maeda et. al. reported that the photocatalytic H_2 evolution on GaN: ZnO can be greatly enhanced by loading Rh core/Cr_2O_3 shell as co-catalyst under visible light irradiation [22]. The enhancement can attribute to efficient charge separation and suppression of water formation.

2.4.3 Bandgap tuning

As shown in Figure 2-5, some semiconductors process very wide bandgap and make them only responsive under UV light. One of the most widely used methods is doping of wide bandgap semiconductor with dopants to modify their bandgap structures. This strategy is often used for band engineering of semiconductors. Dopants can form donor levels in the forbidden band to change the electron excitation of the host semiconductors, as shown in Figure 2-9. This process can largely increase the photo-response of the host semiconductors under visible light irradiation [14, 83, 84]. Doping of semiconductors include cation doping and anion doping.

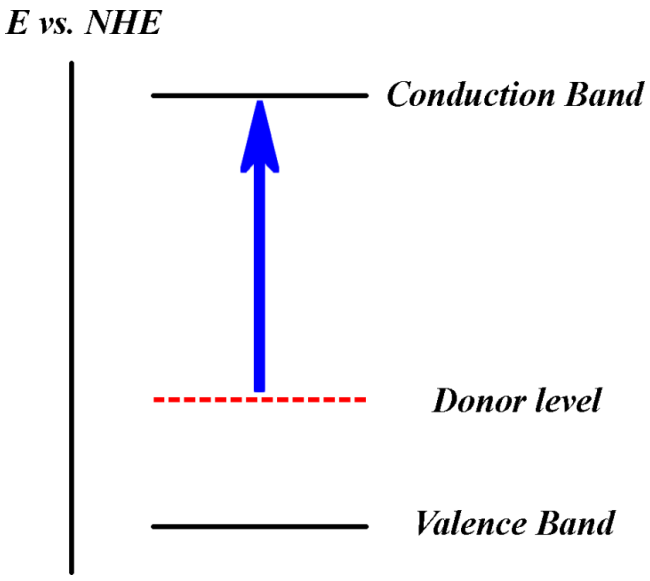

Figure 2-9 Schematic diagram of bandgap modification.

2.4.3.1 Cation doping

Cation doping was proved to be one of the most effective methods and has been extensively investigated for photocatalytic water splitting reaction [85-87]. Most attempts of cation doping were generally doped into host materials by means of lattice substitution. These metal cations can tailor the electronic structures and thus to extend the light response range of the host materials.

When metal cations are successfully doped into the lattice of the semiconductor, the dopants can form impurity energy levels in the bandgap of the host material, as shown below [20]:

$$M^{n+} + hv \rightarrow M^{(n+1)+} + e_{cb}^{-} \quad (2\text{-}6)$$

$$M^{n+} + hv \rightarrow M^{(n+1)+} + h_{vb}^{-} \quad (2\text{-}7)$$

In the equations, M and M^{n+} represent metal and the metal ion dopant, respectively. Moreover, electron-hole recombination can be changed by charge transfer between metal ions and semiconductor, as shown below:

$$\text{Electron trap: } M^{n+} + e_{cb}^{-} \rightarrow M^{(n-1)+} \quad (2\text{-}8)$$

$$\text{Hole trap: } M^{n+} + h_{vb}^{+} \rightarrow M^{(n-1)-} \quad (2\text{-}9)$$

In general, the desired energy level of the dopant should in between of the valance bandgap and the conduction bandgap of the host material, that is, the energy level of $M^{n+}/M^{(n-1)+}$ should be less negative than that of the CB edge, while the energy level of $M^{n+}/M^{(n+1)+}$ should be less positive than that of the VB edge.

Various cations were investigated as dopants in different host photocatalysts including oxide, sulfide and oxynitride. Ru, Rh and Ir were proved to be effective dopants for photocatalytic activity enhancement [88-92]. TiO_2 and $SrTiO_3$ doped with Ru, Rh and Ir possessed intense absorption bands in the visible light region due to excitation from the discontinuous levels formed by the dopants [90, 93]. Pt/$SrTiO_3$: Rh photocatalyst reached an AQY of 5.2 % for the H_2 evolution with the presence of sacrificial reagent under visible light irradiation, mainly due to the contribution from Rh species to form visible light absorption band and provide surface reaction sites [88, 94, 95].

In addition, cation doping works not only to extend the light response, but also to enhance the photocatalytic activity. In another research [86] $SrTiO_3$ photocatalyst development, doping of Na^+ cation with valence lower than that of the host lattice cation (Sr^{2+}) was demonstrated effectively enhanced photocatalytic activity. However, when Ta^{5+} was doped into the lattice to substitute Ti^{4+}, the photocatalytic activity of the sample was suppressed, because the doping of a lower valence cation introduced oxygen vacancies and decreased Ti^{3+}. This provided us some essential ideas of choosing dopants for active photocatalysts design [86].

A lot of investigations initiated by different groups reported that for a certain host material, there exists an optimum cation doping concentration [96-98]. Dopants can introduce in some intermediate energy levels which allow electrons to be excited from valance bandgap to conduction bandgap by smaller excitation energy, thus greatly narrow the bandgap of the host materials and/or tailor the bandgap structure of the host materials, however, overly dope the host materials with cations can introduce recombination centers at the same time . The photocatalytic activity can be compromised due to the increase in electron-hole recombination [99].

2.4.3.2 Anion doping

The use of anion doping to improve hydrogen production under visible light is rather a new method with few investigations reported in open literature. Doping of anions (N, F, C, S etc.) in semiconductors could shift its photo-response into visible spectrum [100-104]. Unlike metal ions (cations), anions less likely form recombination centers and, therefore, it is an effective to enhance the photocatalytic activity.

2.4.4 Development of heterojunction photocatalyst

Different materials can be coupled to form multi-component composites. Development of heterojunction semiconductor composites is another major method to utilize visible light for hydrogen production [105-107]. There are various semiconductor composites types, mainly include metal- semiconductor composites, semiconductor-semiconductor composites and dye-semiconductor composites [4]. When coupled together, due to the components in the photocatalyst have different bandgap characteristics, light absorption can be extended. In addition, the separation of photogenerated charge carriers can also be accelerated. Figure 2-10 shows the schematic diagram of heterojunction photocatalyst for photocatalytic water splitting.

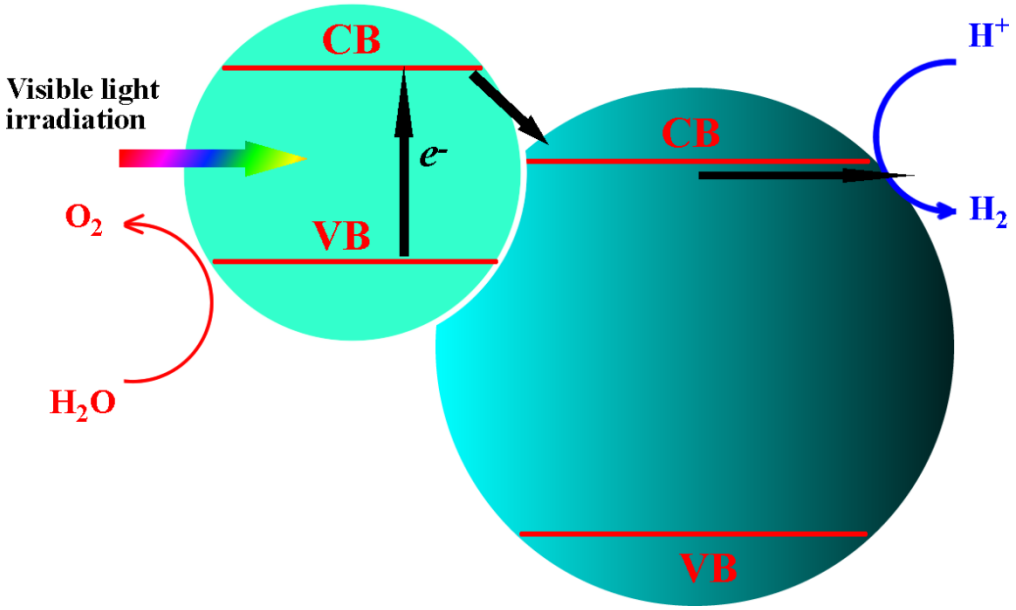

Figure 2-10 Schematic diagram of heterojunction photocatalyst for photocatalytic water splitting.

A general method to produce heterojunction is to couple two semiconductor with different bandgaps. When the composite is irradiated by visible light, the small bandgap semiconductor can injects electrons into the large bandgap semiconductor. High photocatalytic activity in water splitting can be achieved when a semiconductor heterojunction photocatalyst couple by two semiconductors which meet several criteria:

(1) semiconductors should be stable after electron-hole transfer (photocorrosion free), (2) the small bandgap semiconductor can be excited by visible light, (3) the conduction band position of the small bandgap semiconductor lies more negative than that of the large bandgap semiconductor, (4) the conduction band position of the large bandgap semiconductor lies more negative than E_{H_2/H_2O} and (5) electron injection should be fast as well as efficient.

2.5 Chemical additives for H_2 production enhancement

It is difficult to achieve overall water splitting due to various challenges as discussed in the previous chapters. Addition of electron donors and hole scavengers is often employed to facilitate the photocatalytic reactions [108-110] as well as to expedite the evaluation of half-reactions. With the existence of electron donors, the photogenerated holes are consumed by the electron donors quickly and the photogenerated electrons have less chance to recombine with the holes, thus leave abundant electrons to react with hydrogen ions to form hydrogen. Therefore, the hydrogen production can be enhanced. Similarly, oxygen production can be enhanced with

the assistance of electron scavengers. Since these chemical reactions have irreversible nature, continual addition of sacrificial reagents to sustain the reaction is necessary.

Among various sacrificial reagents, alcohol and hydrocarbon are very common ones for hydrogen evolution. EDTA, methanol, ethanol, CN, lactic acid and formaldehyde have been tested and proved to be effective to enhance hydrogen production [76, 81, 111-113]. Some investigations showed that the enhancement capacity for hydrogen production of above reagents followed the sequence as EDTA > methanol > ethanol > lactic acid. However, different report argued methanol was the most efficient sacrificial reagent to promote hydrogen production reaction. These reports are not necessary discrepant. In fact, for different photocatalyst system, the enhancement capacity for these alcohols and hydrocarbons might be different.

Other inorganic ions, such as S^{2-}/SO_3^{2-}, and IO_3^-/I^- were used as sacrificial reagents for hydrogen production when CdS is used as the photocatalyst for photocatalytic hydrogen production [66, 114-117]. CdS has a suitable bandgap to achieve water splitting under visible light. However, it is not stable under irradiation due to photoanodic dissolution (one kind of photocorrosion). For instance, CdS can undergo the following reaction:

$$CdS^+ + 2h^+ \rightarrow Cd^{2+} + S \quad (2\text{-}10)$$

Serving as a sacrificial reagent, S^{2-} can react with 2 holes to form S. The aqueous SO_3^{2-} added can dissolve S into $S_2O_3^{2-}$ in order to prevent any detrimental deposition of S onto CdS. Therefore, photocorrosion of CdS is prevented. I^- (electron donor) and IO_3^- (electron acceptor) can work as a pair of redox mediator, as another example of using inorganic ions as chemical addition to facilitate photocatalytic water splitting and hydrogen evolution for CdS.

Sayama et al. reported that addition of Na_2CO_3 and $NaHCO_3$ could significantly enhance hydrogen and oxygen production on TiO_2 [118, 119]. The carbonate species can react with photogenerated holes to prevent electron-hole recombination (Equation 2-11 to 2-15).

$$CO_3^{2-} + H+ \rightleftharpoons HCO_3^- \quad (2\text{-}11)$$

$$HCO_3^- + h^+ \rightleftharpoons HCO_3^{\bullet} \quad (2\text{-}12)$$

$$HCO_3^{\bullet} \rightleftharpoons H^+ + CO_3^{-\bullet} \quad (2\text{-}13)$$

$$CO_3^{-\bullet} \rightleftharpoons C_2O_6^{2-} \quad (2\text{-}14)$$

$$C_2O_6^{2-} + 2h^+ \rightleftharpoons O_2 + CO_2 \quad (2\text{-}15)$$

The evolved CO_2 can dissolve into water to form CO_3^{2-} and HCO_3^- again to continue to react with photogenerated holes. Addition of Na_2CO_3 with proper amount can suppress the back reaction, however, excess addition of Na_2CO_3 can decrease the rate of hydrogen production since the absorbed carbonate ions on the surface of the photocatalyst can significantly affects the solar light absorption. Addition of iodide was also found to increase the hydrogen production [120]. It is believed that iodine adsorption on Pt can suppress reverse reaction of H_2 and O_2 recombination, thus enhancing the production of hydrogen and oxygen.

It is ideal to develop photocatalysts which can split water under visible light with high efficiency. Though a lot of groups have been working on discovering such photocatalysts, a lot of technical challenges need to be addressed. At the mean time, development of photocatalysts that work only for half reactions of water splitting in the presence of sacrificial reagents can help to understand the mechanism of the photocatalytic reactions. Moreover, these photocatalysts can be used to construct heterojunction semiconductors, as discussed in Chapter 2.4.4. In addition, if biomass and chemical wastes can be used as the electron donors, it will be even more practical to develop photocatalysts for hydrogen production half reaction.

2.6 Summary

Extensive efforts have been devoted for the development of various photocatalytic systems. Studies to date have shown that single component photocatalysts are less likely to achieve sufficient efficiency and stability for practical applications. The integrated heterogeneous system with multiple functional components could combine the advantages of different components to overcome the limitations of single component photocatalysts. A wide range of heterostructures, including metal/semiconductor, semiconductor/semiconductor, molecule/semiconductor, and multi hetero-nanostructures, have been explored for improved photocatalysts by increasing the light absorption, improving the charge separation and transportation, enhancing the catalytic activity and prolonging the functional lifetime. The present review gives a concise overview of heterogeneous photocatalysts with a focus on the relationship between the structural architecture and the photocatalytic activity and stability.

In general, the performance of the current heterogeneous photocatalysts is still far from satisfactory in terms of efficiency and stability, largely limited by the difficulties to control and balance the multiple competing processes, including carrier generation, charge separation and transportation, particularly under the highly corrosive conditions of photochemical reactions. Introducing one component into the photocatalysts to solve one deficiency can often create another set of new challenges. Studies on the heterogeneous photocatalysts are still at the primary stage and further systematic investigations are clearly needed. Rational design of complex heterostructures that can simultaneously facilitate efficient optical absorption, carrier generation, separation, transportation and utilizations is central for a new generation of highly efficient and robust photocatalysts. Significant challenges remain in the synthesis of such complex nanostructures with well designed architectures and optimized charge cascading processes.

References

[1] U.S. Department of Energy, Annual energy outlook, 2011.

[2] D. Gust, T.A. Moore, A.L. Moore, Mimicking photosynthetic solar energy transduction, Accounts of Chemical Research, 34 (2001) 40-48.

[3] B. Oregan, M. Gratzel, A low-cost, high-efficiency solar-cell based on dye-sensitized colloidal TiO_2 films, Nature, 353 (1991) 737-740.

[4] A. Kudo, Y. Miseki, Heterogeneous photocatalyst materials for water splitting, Chemical Society Reviews, 38 (2009) 253-278.

[5] M. Gratzel, Mesoscopic solar cells for electricity and hydrogen production from sunlight, Chemistry Letters, 34 (2005) 8-13.

[6] A. Melis, T. Happe, Hydrogen production: Green algae as a source of energy, Plant Physiology, 127 (2001) 740-748.

[7] N.Z. Muradov, T.N. Veziroglu, "Green" path from fossil-based to hydrogen economy: An overview of carbon-neutral technologies, International Journal of Hydrogen Energy, 33 (2008) 6804-6839.

[8] B. Sakintuna, F. Lamari-Darkrim, M. Hirscher, Metal hydride materials for solid hydrogen storage: A review, International Journal of Hydrogen Energy, 32 (2007) 1121-1140.

[9] A. Kudo, Photocatalyst materials for water splitting, Catalysis Surveys from Asia, 7 (2003) 31-38.

[10] A. Fujishima, T.N. Rao, D.A. Tryk, TiO_2 photocatalysts and diamond electrodes, Electrochimica Acta, 45 (2000) 4683-4690.

[11] A.J. Bard, M.A. Fox, Artificial photosynthesis - solar splitting of water to hydrogen and oxygen, Accounts of Chemical Research, 28 (1995) 141-145.

[12] A.J. Nozik, Photoelectrochemistry- Applications to solar-energy conversion, Annual Review of Physical Chemistry, 29 (1978) 189-222.

[13] Z.G. Zou, J.H. Ye, K. Sayama, H. Arakawa, Direct splitting of water under visible light irradiation with an oxide semiconductor photocatalyst, Nature, 414 (2001) 625-627.

[14] J.H. Park, S. Kim, A.J. Bard, Novel carbon-doped TiO_2 nanotube arrays with high aspect ratios for efficient solar water splitting, Nano Letters, 6 (2006) 24-28.

[15] F.E. Osterloh, Inorganic materials as catalysts for photochemical splitting of water, Chemistry of Materials, 20 (2008) 35-54.

[16] A. Fujishima, K. Honda, Electrochemical photolysis of water at a semiconductor electrode, Nature, 238 (1972) 37.

[17] H. Kato, K. Asakura, A. Kudo, Highly efficient water splitting into H_2 and O_2 over lanthanum-doped $NaTaO_3$ photocatalysts with high crystallinity and surface nanostructure, Journal of the American Chemical Society, 125 (2003) 3082-3089.

[18] A. Kudo, H. Kato, S. Nakagawa, Water splitting into H_2 and O_2 on new $Sr_2M_2O_7$ (M = Nb and Ta) photocatalysts with layered perovskite structures: Factors affecting the photocatalytic activity, Journal of Physical Chemistry B, 104 (2000) 571-575.

[19] M. Hara, T. Kondo, M. Komoda, S. Ikeda, K. Shinohara, A. Tanaka, J.N. Kondo, K. Domen, Cu_2O as a photocatalyst for overall water splitting under visible light irradiation, Chemical Communications, (1998) 357-358.

[20] M. Ni, M.K.H. Leung, D.Y.C. Leung, K. Sumathy, A review and recent developments in photocatalytic water-splitting using TiO_2 for hydrogen production, Renewable & Sustainable Energy Reviews, 11 (2007) 401-425.

[21] X.B. Chen, S.H. Shen, L.J. Guo, S.S. Mao, Semiconductor-based photocatalytic hydrogen generation, Chemical Reviews, 110 (2010) 6503-6570.

[22] K. Maeda, K. Domen, Photocatalytic water splitting: recent progress and future challenges, Journal of Physical Chemistry Letters, 1 (2010) 2655-2661.

[23] W.J. Youngblood, S.H.A. Lee, K. Maeda, T.E. Mallouk, Visible light water splitting using dye-sensitized oxide semiconductors, Accounts of Chemical Research, 42 (2009) 1966-1973.

[24] R. Abe, Recent progress on photocatalytic and photoelectrochemical water splitting under visible light irradiation, Journal of Photochemistry and Photobiology C-Photochemistry Reviews, 11 (2010) 179-209.

[25] M. Kitano, M. Matsuoka, M. Ueshima, M. Anpo, Recent developments in titanium oxide-based photocatalysts, Applied Catalysis A-General, 325 (2007) 1-14.

[26] K. Domen, J.N. Kondo, M. Hara, T. Takata, Photo- and mechano-catalytic overall water splitting reactions to form hydrogen and oxygen on heterogeneous catalysts, Bulletin of the Chemical Society of Japan, 73 (2000) 1307-1331.

[27] A. Kudo, H. Kato, I. Tsuji, Strategies for the development of visible-light-driven photocatalysts for water splitting, Chemistry Letters, 33 (2004) 1534-1539.

[28] M.D. Hernandez-Alonso, F. Fresno, S. Suarez, J.M. Coronado, Development of alternative photocatalysts to TiO_2: Challenges and opportunities, Energy & Environmental Science, 2 (2009) 1231-1257.
[29] R. van de Krol, Y.Q. Liang, J. Schoonman, Solar hydrogen production with nanostructured metal oxides, Journal of Materials Chemistry, 18 (2008) 2311-2320.
[30] T. Takata, A. Tanaka, M. Hara, J.N. Kondo, K. Domen, Recent progress of photocatalysts for overall water splitting, Catalysis Today, 44 (1998) 17-26.
[31] M. Matsuoka, M. Kitano, M. Takeuchi, K. Tsujimaru, M. Anpo, J.M. Thomas, Photocatalysis for new energy production - Recent advances in photocatalytic water splitting reactions for hydrogen production, Catalysis Today, 122 (2007) 51-61.
[32] Z.G. Zou, H. Arakawa, Direct water splitting into H_2 and O_2 under visible light irradiation with a new series of mixed oxide semiconductor photocatalysts, Journal of Photochemistry and Photobiology A-Chemistry, 158 (2003) 145-162.
[33] D. Gust, T.A. Moore, A.L. Moore, Solar fuels via artificial photosynthesis, Accounts of Chemical Research, 42 (2009) 1890-1898.
[34] G. Renger, T. Renger, Photosystem II: The machinery of photosynthetic water splitting, Photosynthesis Research, 98 (2008) 53-80.
[35] J. Nowotny, T. Bak, M.K. Nowotny, L.R. Sheppard, TiO_2 surface active sites for water splitting, Journal of Physical Chemistry B, 110 (2006) 18492-18495.
[36] M. Anpo, S. Dohshi, M. Kitano, Y. Hu, M. Takeuchi, M. Matsuoka, The preparation and characterization of highly efficient titanium oxide-based photofunctional materials, Annual Review of Materials Research, 35 (2005) 1-27.
[37] M.G. Walter, E.L. Warren, J.R. McKone, S.W. Boettcher, Q.X. Mi, E.A. Santori, N.S. Lewis, Solar water splitting cells, Chemical Reviews, 110 (2010) 6446-6473.
[38] K. Maeda, Photocatalytic water splitting using semiconductor particles: History and recent developments, Journal of Photochemistry and Photobiology C-Photochemistry Reviews, 12 (2011) 237-268.
[39] O. Khaselev, J.A. Turner, A monolithic photovoltaic-photoelectrochemical device for hydrogen production via water splitting, Science, 280 (1998) 425-427.
[40] G.K. Mor, K. Shankar, M. Paulose, O.K. Varghese, C.A. Grimes, Enhanced photocleavage of water using titania nanotube arrays, Nano Letters, 5 (2005) 191-195.

[41] S.U.M. Khan, J. Akikusa, Photoelectrochemical splitting of water at nanocrystalline n-Fe_2O_3 thin-film electrodes, Journal of Physical Chemistry B, 103 (1999) 7184-7189.

[42] W.J. Youngblood, S.H.A. Lee, Y. Kobayashi, E.A. Hernandez-Pagan, P.G. Hoertz, T.A. Moore, A.L. Moore, D. Gust, T.E. Mallouk, Photoassisted overall water splitting in a visible light-absorbing dye-sensitized photoelectrochemical cell, Journal of the American Chemical Society, 131 (2009) 926.

[43] K. Maeda, T. Takata, M. Hara, N. Saito, Y. Inoue, H. Kobayashi, K. Domen, GaN : ZnO solid solution as a photocatalyst for visible-light-driven overall water splitting, Journal of the American Chemical Society, 127 (2005) 8286-8287.

[44] T. Takata, K. Shinohara, A. Tanaka, M. Hara, J.N. Kondo, K. Domen, A highly active photocatalyst for overall water splitting with a hydrated layered perovskite structure, Journal of Photochemistry and Photobiology A-Chemistry, 106 (1997) 45-49.

[45] A. Kudo, Development of photocatalyst materials for water splitting, International Journal of Hydrogen Energy, 31 (2006) 197-202.

[46] D. Yamasita, T. Takata, M. Hara, J.N. Kondo, K. Domen, Recent progress of visible-light-driven heterogeneous photocatalysts for overall water splitting, Solid State Ionics, 172 (2004) 591-595.

[47] A. Galinska, J. Walendziewski, Photocatalytic water splitting over Pt-TiO_2 in the presence of sacrificial reagents, Energy & Fuels, 19 (2005) 1143-1147.

[48] T. Watanabe, A. Nakajima, R. Wang, M. Minabe, S. Koizumi, A. Fujishima, K. Hashimoto, Photocatalytic activity and photoinduced hydrophilicity of titanium dioxide coated glass, Thin Solid Films, 351 (1999) 260-263.

[49] A. Fujishima, X.T. Zhang, Titanium dioxide photocatalysis: present situation and future approaches, Comptes Rendus Chimie, 9 (2006) 750-760.

[50] Y. Paz, Z. Luo, L. Rabenberg, A. Heller, Photooxidative self-cleaning transparent titanium-dioxide films on glass, Journal of Materials Research, 10 (1995) 2842-2848.

[51] G.K. Mor, M.A. Carvalho, O.K. Varghese, M.V. Pishko, C.A. Grimes, A room-temperature TiO_2-nanotube hydrogen sensor able to self-clean photoactively from environmental contamination, Journal of Materials Research, 19 (2004) 628-634.

[52] A. Fernandez, G. Lassaletta, V.M. Jimenez, A. Justo, A.R. GonzalezElipe, J.M. Herrmann, H. Tahiri, Y. AitIchou, Preparation and characterization of TiO_2 photocatalysts supported on

various rigid supports (glass, quartz and stainless steel). Comparative studies of photocatalytic activity in water purification, Applied Catalysis B-Environmental, 7 (1995) 49-63.

[53] J. Zhao, X.D. Yang, Photocatalytic oxidation for indoor air purification: a literature review, Building and Environment, 38 (2003) 645-654.

[54] Y. Horie, D.A. David, M. Taya, S. Tone, Effects of light intensity and titanium dioxide concentration on photocatalytic sterilization rates of microbial cells, Industrial & Engineering Chemistry Research, 35 (1996) 3920-3926.

[55] N. Armaroli, V. Balzani, The future of energy supply: Challenges and opportunities, Angewandte Chemie-International Edition, 46 (2007) 52-66.

[56] K. Maeda, K. Teramura, D.L. Lu, T. Takata, N. Saito, Y. Inoue, K. Domen, Photocatalyst releasing hydrogen from water - Enhancing catalytic performance holds promise for hydrogen production by water splitting in sunlight, Nature, 440 (2006) 295-295.

[57] H.G. Yu, H. Irie, K. Hashimoto, Conduction band energy level control of titanium dioxide: Toward an efficient visible-light-sensitive photocatalyst, Journal of the American Chemical Society, 132 (2010) 6898.

[58] K. Maeda, K. Domen, New non-oxide photocatalysts designed for overall water splitting under visible light, Journal of Physical Chemistry C, 111 (2007) 7851-7861.

[59] M. Anpo, M. Takeuchi, K. Ikeue, S. Dohshi, Design and development of titanium oxide photocatalysts operating under visible and UV light irradiation. The applications of metal ion-implantation techniques to semiconducting TiO_2 and Ti/Zeolite catalysts, Current Opinion in Solid State & Materials Science, 6 (2002) 381-388.

[60] A. Kudo, Recent progress in the development of visible light-driven powdered photocatalysts for water splitting, International Journal of Hydrogen Energy, 32 (2007) 2673-2678.

[61] A. Kudo, I. Mikami, New $In_2O_3(ZnO)_m$ photocatalysts with laminal structure for visible light-induced H_2 or O_2 evolution from aqueous solutions containing sacrificial reagents, Chemistry Letters, (1998) 1027-1028.

[62] A. Kudo, I. Mikami, Photocatalytic activities and photophysical properties of $Ga_{2-x}In_xO_3$ solid solution, Journal of the Chemical Society-Faraday Transactions, 94 (1998) 2929-2932.

[63] A. Harriman, I.J. Pickering, J.M. Thomas, P.A. Christensen, Metal-Oxides as heterogeneous catalysts for oxygen evolution under photochemical conditions, Journal of the Chemical Society-Faraday Transactions I, 84 (1988) 2795-2806.

[64] H. Kato, A. Kudo, Energy structure and photocatalytic activity for water splitting of $Sr_2(Ta_{1-x}Nb_x)_2O_7$ solid solution, Journal of Photochemistry and Photobiology A-Chemistry, 145 (2001) 129-133.

[65] Y. Lee, H. Terashima, Y. Shimodaira, K. Teramura, M. Hara, H. Kobayashi, K. Domen, M. Yashima, Zinc germanium oxynitride as a photocatalyst for overall water splitting under visible light, Journal of Physical Chemistry C, 111 (2007) 1042-1048.

[66] Q. Li, B.D. Guo, J.G. Yu, J.R. Ran, B.H. Zhang, H.J. Yan, J.R. Gong, Highly efficient visible-light-driven photocatalytic hydrogen production of CdS-cluster-decorated graphene nanosheets, Journal of the American Chemical Society, 133 (2011) 10878-10884.

[67] J.G. Yu, L.F. Qi, M. Jaroniec, Hydrogen production by photocatalytic water splitting over Pt/TiO_2 nanosheets with exposed (001) facets, Journal of Physical Chemistry C, 114 (2010) 13118-13125.

[68] C.G. Silva, R. Juarez, T. Marino, R. Molinari, H. Garcia, Influence of excitation wavelength (UV or visible light) on the photocatalytic activity of titania containing gold nanoparticles for the generation of hydrogen or oxygen from water, Journal of the American Chemical Society, 133 (2011) 595-602.

[69] G.L. Chiarello, E. Selli, L. Forni, Photocatalytic hydrogen production over flame spray pyrolysis-synthesised TiO_2 and Au/TiO_2, Applied Catalysis B-Environmental, 84 (2008) 332-339.

[70] O. Rosseler, M.V. Shankar, M.K.L. Du, L. Schmidlin, N. Keller, V. Keller, Solar light photocatalytic hydrogen production from water over Pt and Au/TiO_2(anatase/rutile) photocatalysts: Influence of noble metal and porogen promotion, Journal of Catalysis, 269 (2010) 179-190.

[71] B.J. Ma, F.Y. Wen, H.F. Jiang, J.H. Yang, P.L. Ying, C. Li, The synergistic effects of two co-catalysts on Zn_2GeO_4 on photocatalytic water splitting, Catalysis Letters, 134 (2010) 78-86.

[72] H. Bahruji, M. Bowker, P.R. Davies, F. Pedrono, New insights into the mechanism of photocatalytic reforming on Pd/TiO_2, Applied Catalysis B-Environmental, 107 (2011) 205-209.

[73] S.M. Arachchige, R. Shaw, T.A. White, V. Shenoy, H.M. Tsui, K.J. Brewer, High turnover in a photocatalytic system for water reduction to produce hydrogen using a Ru, Rh, Ru photoinitiated electron collector, Chemsuschem, 4 (2011) 514-518.
[74] Z.G. Yang, J.L. Zhang, M.C.W. Kintner-Meyer, X.C. Lu, D.W. Choi, J.P. Lemmon, J. Liu, Electrochemical energy storage for green grid, Chemical Reviews, 111 (2011) 3577-3613.
[75] H.L. Zhou, Y.Q. Qu, T. Zeid, X.F. Duan, Towards highly efficient photocatalysts using semiconductor nanoarchitectures, Energy & Environmental Science, 5 (2012) 6732-6743.
[76] G.R. Bamwenda, S. Tsubota, T. Nakamura, M. Haruta, Photoassisted hydrogen-production from a water-ethanol solution - a comparison of activities of Au-TiO_2 and Pt-TiO_2, Journal of Photochemistry and Photobiology A-Chemistry, 89 (1995) 177-189.
[77] B. Ohtani, K. Iwai, S. Nishimoto, S. Sato, Role of platinum deposits on titanium(IV) oxide particles: Structural and kinetic analyses of photocatalytic reaction in aqueous alcohol and amino acid solutions, Journal of Physical Chemistry B, 101 (1997) 3349-3359.
[78] H. Tada, T. Mitsui, T. Kiyonaga, T. Akita, K. Tanaka, All-solid-state Z-scheme in CdS-Au-TiO_2 three-component nanojunction system, Nature Materials, 5 (2006) 782-786.
[79] Y. Sasaki, A. Iwase, H. Kato, A. Kudo, The effect of co-catalyst for Z-scheme photocatalysis systems with an Fe^{3+}/Fe^{2+} electron mediator on overall water splitting under visible light irradiation, Journal of Catalysis, 259 (2008) 133-137.
[80] Y.Q. Qu, X.F. Duan, Progress, challenge and perspective of heterogeneous photocatalysts, Chemical Society Reviews, 42 (2013) 2568-2580.
[81] X. Zong, H.J. Yan, G.P. Wu, G.J. Ma, F.Y. Wen, L. Wang, C. Li, Enhancement of photocatalytic H_2 evolution on CdS by loading MOS_2 as cocatalyst under visible light irradiation, Journal of the American Chemical Society, 130 (2008) 7176.
[82] Q.J. Xiang, J.G. Yu, M. Jaroniec, Synergetic effect of MoS_2 and graphene as cocatalysts for enhanced photocatalytic H_2 production activity of TiO_2 nanoparticles, Journal of the American Chemical Society, 134 (2012) 6575-6578.
[83] H.M. Luo, T. Takata, Y.G. Lee, J.F. Zhao, K. Domen, Y.S. Yan, Photocatalytic activity enhancing for titanium dioxide by co-doping with bromine and chlorine, Chemistry of Materials, 16 (2004) 846-849.

[84] I. Cesar, A. Kay, J.A.G. Martinez, M. Gratzel, Translucent thin film Fe_2O_3 photoanodes for efficient water splitting by sunlight: Nanostructure-directing effect of Si-doping, Journal of the American Chemical Society, 128 (2006) 4582-4583.
[85] A. Kudo, R. Niishiro, A. Iwase, H. Kato, Effects of doping of metal cations on morphology, activity, and visible light response of photocatalysts, Chemical Physics, 339 (2007) 104-110.
[86] T. Takata, K. Domen, Defect engineering of photocatalysts by doping of aliovalent metal cations for efficient water splitting, Journal of Physical Chemistry C, 113 (2009) 19386-19388.
[87] K.E. Karakitsou, X.E. Verykios, Effects of altervalent cation doping of TiO_2 on its performance as a photocatalyst for water cleavage, Journal of Physical Chemistry, 97 (1993) 1184-1189.
[88] Y. Sasaki, H. Nemoto, K. Saito, A. Kudo, Solar water splitting using powdered photocatalysts driven by Z-schematic interparticle electron transfer without an electron mediator, Journal of Physical Chemistry C, 113 (2009) 17536-17542.
[89] K. Gurunathan, Photocatalytic hydrogen production using transition metal ions-doped gamma-Bi_2O_3 semiconductor particles, International Journal of Hydrogen Energy, 29 (2004) 933-940.
[90] J. Choi, H. Park, M.R. Hoffmann, Effects of single metal-Ion doping on the visible-light photoreactivity of TiO_2, Journal of Physical Chemistry C, 114 (2010) 783-792.
[91] S.W. Bae, P.H. Borse, J.S. Lee, Dopant dependent band gap tailoring of hydrothermally prepared cubic $SrTi_xM_{1-x}O_3$ (M=Ru,Rh,Ir,Pt,Pd) nanoparticles as visible light photocatalysts, Applied Physics Letters, 92 (2008).
[92] Y. Okazaki, T. Mishima, S. Nishimoto, M. Matsuda, M. Miyake, Photocatalytic activity of $Ca_3Ti_2O_7$ layered-perovskite doped with Rh under visible light irradiation, Materials Letters, 62 (2008) 3337-3340.
[93] R. Konta, T. Ishii, H. Kato, A. Kudo, Photocatalytic activities of noble metal ion doped $SrTiO_3$ under visible light irradiation, Journal of Physical Chemistry B, 108 (2004) 8992-8995.
[94] K. Iwashina, A. Kudo, Rh-doped $SrTiO_3$ photocatalyst electrode showing cathodic photocurrent for water splitting under visible-light irradiation, Journal of the American Chemical Society, 133 (2011) 13272-13275.
[95] A. Kudo, Z-scheme photocatalyst systems for water splitting under visible light irradiation, MRS Bulletin, 36 (2011) 32-38.

[96] R. Asahi, T. Morikawa, T. Ohwaki, K. Aoki, Y. Taga, Visible-light photocatalysis in nitrogen-doped titanium oxides, Science, 293 (2001) 269-271.

[97] J.C. Yu, J.G. Yu, W.K. Ho, Z.T. Jiang, L.Z. Zhang, Effects of F- doping on the photocatalytic activity and microstructures of nanocrystalline TiO_2 powders, Chemistry of Materials, 14 (2002) 3808-3816.

[98] H. Irie, Y. Watanabe, K. Hashimoto, Nitrogen-concentration dependence on photocatalytic activity of $TiO_{2-x}N_x$ powders, Journal of Physical Chemistry B, 107 (2003) 5483-5486.

[99] K. Maeda, M. Higashi, D.L. Lu, R. Abe, K. Domen, Efficient nonsacrificial water splitting through two-step photoexcitation by visible light using a modified oxynitride as a hydrogen evolution photocatalyst, Journal of the American Chemical Society, 132 (2010) 5858-5868.

[100] D. Li, N. Ohashi, S. Hishita, T. Kolodiazhnyi, H. Haneda, Origin of visible-light-driven photocatalysis: A comparative study on N/F-doped and N-F-codoped TiO_2 powders by means of experimental characterizations and theoretical calculations, Journal of Solid State Chemistry, 178 (2005) 3293-3302.

[101] H. Wang, J.P. Lewis, Second-generation photocatalytic materials: anion-doped TiO_2, Journal of Physics-Condensed Matter, 18 (2006) 421-434.

[102] X. Yang, C. Cao, K. Hohn, L. Erickson, R. Maghirang, D. Hamal, K. Klabunde, Highly visible-light active C- and V-doped TiO_2 for degradation of acetaldehyde, Journal of Catalysis, 252 (2007) 296-302.

[103] G. Liu, P. Niu, C. Sun, S.C. Smith, Z. Chen, G.Q. Lu, H.-M. Cheng, Unique electronic structure induced high photoreactivity of sulfur-doped graphitic C_3N_4, Journal of the American Chemical Society, 132 (2010) 11642-11648.

[104] K. Yang, Y. Dai, B. Huang, Understanding photocatalytic activity of S- and P-doped TiO_2 under visible light from first-principles, Journal of Physical Chemistry C, 111 (2007) 18985-18994.

[105] W.F. Shangguan, A. Yoshida, Photocatalytic hydrogen evolution from water on nanocomposites incorporating cadmium sulfide into the interlayer, Journal of Physical Chemistry B, 106 (2002) 12227-12230.

[106] J. Hensel, G. Wang, Y. Li, J.Z. Zhang, Synergistic effect of CdSe quantum dot sensitization and nitrogen doping of TiO_2 nanostructures for photoelectrochemical solar hydrogen generation, Nano Letters, 10 (2010) 478-483.

[107] Q. Xiang, J. Yu, M. Jaroniec, Preparation and enhanced visible-light photocatalytic H_2 production activity of graphene/C_3N_4 composites, Journal of Physical Chemistry C, 115 (2011) 7355-7363.

[108] M. Ashokkumar, An overview on semiconductor particulate systems for photoproduction of hydrogen, International Journal of Hydrogen Energy, 23 (1998) 427-438.

[109] Z. Jin, X. Zhang, Y. Li, S. Li, G. Lu, 5.1% Apparent quantum efficiency for stable hydrogen generation over eosin-sensitized CuO/TiO_2 photocatalyst under visible light irradiation, Catalysis Communications, 8 (2007) 1267-1273.

[110] R. Niishiro, H. Kato, A. Kudo, Nickel and either tantalum or niobium-codoped TiO_2 and $SrTiO_3$ photocatalysts with visible-light response for H_2 or O_2 evolution from aqueous solutions, Physical Chemistry Chemical Physics, 7 (2005) 2241-2245.

[111] S.G. Lee, S. Lee, H.I. Lee, Photocatalytic production of hydrogen from aqueous solution containing CN^- as a hole scavenger, Applied Catalysis a-General, 207 (2001) 173-181.

[112] H. Byrd, A. Clearfield, D. Poojary, K.P. Reis, M.E. Thompson, Crystal structure of a porous zirconium phosphate/phosphonate compound and photocatalytic hydrogen production from related materials, Chemistry of Materials, 8 (1996) 2239-2246.

[113] A. Kudo, I. Tsuji, H. Kato, $AgInZn_7S_9$ solid solution photocatalyst for H_2 evolution from aqueous solutions under visible light irradiation, Chemical Communications, (2002) 1958-1959.

[114] J.S. Jang, S.M. Ji, S.W. Bae, H.C. Son, J.S. Lee, Optimization of CdS/TiO_2 nano-bulk composite photocatalysts for hydrogen production from Na_2S/Na_2SO_3 aqueous electrolyte solution under visible light (lambda >= 420 nm), Journal of Photochemistry and Photobiology A-Chemistry, 188 (2007) 112-119.

[115] N. Bao, L. Shen, T. Takata, K. Domen, Self-templated synthesis of nanoporous CdS nanostructures for highly efficient photocatalytic hydrogen production under visible, Chemistry of Materials, 20 (2008) 110-117.

[116] D. Jing, L. Guo, A novel method for the preparation of a highly stable and active CdS photocatalyst with a special surface nanostructure, Journal of Physical Chemistry B, 110 (2006) 11139-11145.

[117] R. Abe, M. Higashi, K. Domen, Overall water splitting under visible light through a two-step photoexcitation between TaON and WO_3 in the presence of an iodate-iodide shuttle redox mediator, Chemsuschem, 4 (2011) 228-237.

[118] K. Sayama, H. Arakawa, Effect of carbonate salt addition on the photocatalytic decomposition of liquid water over Pt-TiO_2 catalyst, Journal of the Chemical Society-Faraday Transactions, 93 (1997) 1647-1654.
[119] K. Sayama, K. Yase, H. Arakawa, K. Asakura, A. Tanaka, K. Domen, T. Onishi, Photocatalytic activity and reaction mechanism of Pt-intercalated $K_4Nb_6O_{17}$ catalyst on the water splitting in carbonate salt aqueous solution, Journal of Photochemistry and Photobiology A-Chemistry, 114 (1998) 125-135.
[120] R. Abe, K. Sayama, H. Arakawa, Significant effect of iodide addition on water splitting into H_2 and O_2 over Pt-loaded TiO_2 photocatalyst: suppression of backward reaction, Chemical Physics Letters, 371 (2003) 360-364.

Chapter 3

Development of Perovskite Based Photocatalysts for Photocatalytic Water Splitting and Hydrogen Evolution

3.1 Crystal structure of perovskite structure materials

Perovskite structure materials are generally recognized a series of binary oxides with various crystalline structures and different physical chemical properties [1, 2]. Perovskite materials belongs ABO_3 structure family and are well known for their high efficiency for photocatalytic water splitting and hydrogen evolution in solar irradiation [3, 4]. One good example of perovskite materials is $SrTiO_3$, which has a simple cubic structure (space group, $Pm\bar{3}m$) [5] (Figure 3-1). Perovskite materials have two sites for metal cations, which are A sites and B sites. Both A sites and B sites are occupied by metal cations, which are bonded with 12 and 6 O anions, respectively. Cations with larger atomic radius are generally occupied A sites while smaller cations take B sites. A site cation is in the center of a cubic cell, surrounded by eight BO_6 octahedra with shared corners [6]. Using cation substitution in A sites and/or B sites, different composition and symmetry of the oxides can be achieved. Due to lattice distortion, the real perovskite structure normally exhibited different crystal phases such as orthogonal, tetragonal, monoclinic and triclinic phase [6]. The lattice distortion plays an important role in crystalline quality, dipole characteristics and band structures, therefore it can greatly influence the photocatalytic activity of water splitting or hydrogen evolution [7-9].

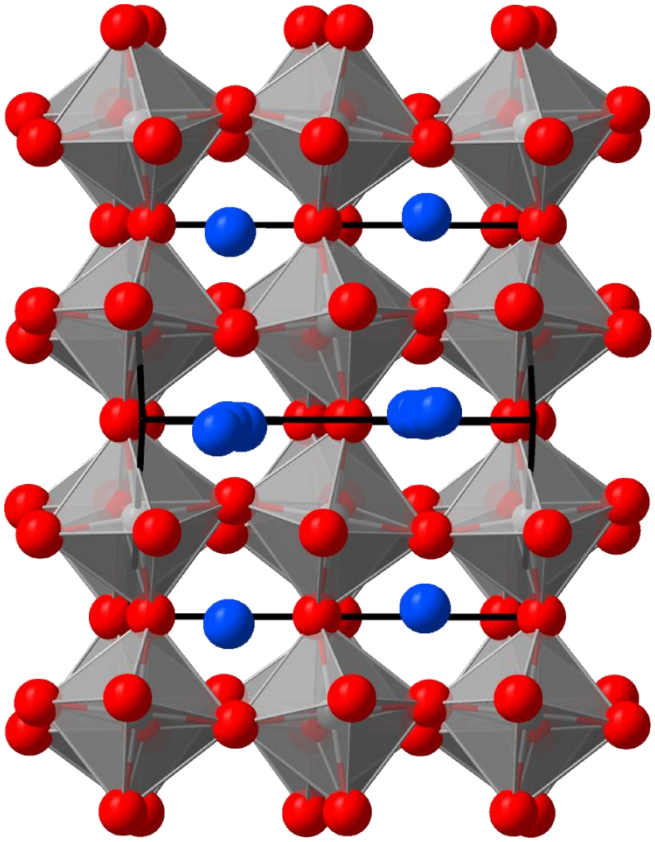

Figure 3-1 Schematic diagram of simple cubic perovskite structure material.

3.2 Chemical composition characteristics of perovskite structure materials

Perovskite structure can be adopted by many metal elements in periodic table [10, 11]. Perovskite structure materials can be easily synthesized using different chemical stoichiometry. This can be used to fabricate novel photocatalyst for water splitting and hydrogen evolution. For example, literature provides examples of $SrTiO_3$, $ATaO_3$ (A=Li, Na, K), $MCo_{1/3}Nb_{2/3}O_3$ (M = Ca, Sr, Ba) structures, which were successfully synthesized and exhibited high photocatalytic activity [12-15]. Overall, it has been shown that ABO_3 electronic band structures can be further tuned by doping, therefore the visible light response properties can be optimized [16, 17]. In addition, the variable oxidation states (valence bandgap states) introduced by the doped metal cations can be introduced into perovskite structure playing important roles in electron excitation as well as charge separation [18, 19]. Finally, the important advantage of these structures is related to their synthesis. The synthesis methods for ABO_3 materials are normally easy and straightforward, while dopant concentration can be easily controlled. All of the above mentioned

make perovskite type materials to be very promising candidates for photocatalysts development [15, 20].

3.3 Development of perovskite structure photocatalysts

Different modification strategies (such as ion doping, co-catalysts loading, and development of composite structures) were employed to develop perovskite structure photocatalysts with improved performance for photocatalytic water splitting and hydrogen production [19].

3.3.1 Ion doping

In general, ion doping includes two main methods, interstitial doping and lattice substitution. Substitutional doping of perovskite structure can happen when the dopant concentration and the doping coefficient are suitable [21].

A number of perovskite structure photocatalysts were synthesized and found to be efficient candidates for H_2 and/or O_2 evolution especially for overall water splitting under ultraviolet (UV) irradiation [4, 14, 15, 21-25]. However, the practical applications by using visible light for water splitting were limited due to their wide bandgaps. Consequently, an alternative strategy was focused on metal cations doping into perovskite structure to tailor the electronic structures and thus to extend the light response range [26]. In order to control the valence states of doped metal cations and to reduce the lattice defects in perovskite structure photocatalysts, another strategy, such as codoping, was generally adopted to maintain the charge balance.

It could be found that both the types and valence states of doped transition metals play important roles in enabling the visible-light response and improving the photocatalytic activities, and perovskite structure hosts provide excellent platforms for the modification of ion doping.

3.3.2 Co-catalyst loading

Co-catalysts could promote the separation of photoexcited electrons and holes. Moreover, co-catalysts offer the low activation potentials for H_2 or O_2 evolution and are often served as the active sites for H_2 or O_2 generation [27, 28]. Therefore, the loading of proper co-catalysts can greatly enhance the activities of photocatalysts, as discussed in the previous chapter. Various co-catalysts, such as NiO [29, 30], Ag [31], Au[32, 33], Pt [24, 34], Ni [35] were proved to be effective co-catalysts for perovskite structure photocatalysts for H_2 evolution, O_2 evolution and CO_2 reduction. However, the mechanisms for activity enhancement were different due to the different structural features, which were considerably affected by the interaction between co-

catalyst and photocatalyst interfaces. Further research on interaction between co-catalysts and perovskite structure photocatalysts is needed to clarify these mechanisms [26].

3.3.3 Multi-component composites

Synergistic effect on photocatalytic performance could be achieved when different materials are combined to form multi-component composites [36-39]. Heterojunctions could be formed by coupling other band structure-matched semiconductors with perovskite structure photocatalysts to facilitate separation of photogenerated charge carriers. For example, $TiO_2/SrTiO_3$ heterostructures were prepared by different groups [40-43]. Ng et al. reported that in comparison to the respective pristine semiconductor photocatalysts, the heterostructured $TiO_2/SrTiO_3$ film showed the highest efficiency in photocatalytic splitting of water to produce H_2, 4.9 times that of TiO_2 and 2.1 times that of $SrTiO_3$. The enhanced photocatalytic efficiency is largely attributed to the efficient separation of photogenerated charges at heterojunctions of the two dissimilar semiconductors, as well as a negative redox potential shift in the Fermi level. Furthermore, the coupled semiconductors with perovskite structure photocatalysts could act as photosensitizers to harness low-energy photons that could not be utilized by the perovskite structure host due to the wide bandgaps [44, 45].

3.4 Preparation strategies for perovskite structure photocatalysts

3.4.1 Solid state reaction

Solid state reaction (SSR) method is one of the most common methods to synthesize solid oxide photocatalysts [46]. SSR method is fairly straightforward as it involves simple mixing of precursors, followed by repeated cycles of grinding and high temperature calcination. The solid state reaction starts from nuclei formation at the interfaces between reactants. The reaction rate depends on the diffusion coefficient and dopant concentration. Temperature is a favorable factor for increasing the diffusion coefficient. Therefore, it requires high temperature to provide enough energy for ion transport [47] as well as proper dopant concentration for a successful doping. Additionally, the precursors have to be well mixed by grinding in order to increase contact between their surfaces. The final stage of the synthesis process is calcinations, which results in formation of oxidation products [48]. The advantages of this method are low cost, easily available precursors and simplicity. However, this approach results in poor uniformity and large particle size resulted from high temperature treatment, which was also linked to recombination

of photogenerated carriers [23]. In addition, larger particles have smaller specific surface areas, leading to low overall catalytic activity [49]. Figure 3-2 shows a typical synthesis process for solid state reaction method.

Figure 3-2 Schematic of synthesis process for solid state reaction method.

3.4.2 Hydrothermal/solvothermal reaction

Hydrothermal/solvothermal reaction method has also been widely employed to synthesize nanosized materials [50]. The method can potentially be used to produce bigger, purer and dislocation-free single crystals. The nanoparticles produced by this method have a significant degree of crystallinity and purity, few defects and novel morphologies, which are very beneficial for improving the photocatalytic activity of the synthesized materials [51-53].

Many perovskite structure photocatalysts synthesized by hydrothermal/solvothermal reaction method were reported as efficient photocatalysts [54-56]. For example, Chen and Ye successfully prepared dumbbell-like and rod-like $SrSnO_3$ nanostructures by a facile hydrothermal process and subsequent heat-treatment process. Compared to the sample produced by solid-state reaction, the as-prepared $SrSnO_3$ nanostructures showed higher activity for H_2 and O_2 evolution under UV light irradiation due to the higher surface area and fewer defects [56]. Ding et al. synthesized $KNbO_3$ single-crystal nanowires by a hydrothermal method. The prepared nanowires achieved the highest photocatalytic activity for H_2 production from aqueous CH_3OH solutions among all reported $KNbO_3$ materials conceivably due to high surface area and high crystallinity [57]. In another publication, Yu et al. from the same group synthesized Cr-doped $SrTiO_3$ with high specific surface areas (19.3–65.4 m^2/g), good crystallinity, and small crystalline size (20-30 nm) by using a sol–gel hydrothermal method. The as prepared Pt/Cr-doped $SrTiO_3$ photocatalyst exhibited visible light induced H_2 evolution rates 3 times higher than that of the sample prepared by solid-state reaction presumably due to the high specific surface area and good crystallinity [58].

However, the challenges associated with this method are in achieving a precise control of various reaction parameters, such as temperature, duration of synthesis, pressure, solvent type, pH and others [59, 60].

3.4.3 Polymerizable complex method

Among other options of synthesis is the sol-gel method, which involves hydrolysis-condensation of metal-alkoxides, concentration of aqueous solutions containing metal-chelates and organic polymeric gel [30]. However, due to the fast hydrolysis rate of the metal alkoxides, controlling the homogeneity of different components during experiments presents a formidable challenge [31].

The polymerizable complex method (PC method, also called Pechini route), which is a modified sol-gel approach, is another promising method for the preparation of solid oxide catalysts [61-64]. In contrast to synthesis by solid state reaction, the PC approach requires rather mild preparation conditions. Parameters such as crystallinity, particle size and surface morphology can be easily controlled by changing the calcination temperature. For example, it has been reported that $K_2La_2Ti_3O_{10}$ [23, 65] and $KTiNbO_5$ [66] prepared by the PC method have higher crystallinity, smaller crystallite size and better size uniformity than those prepared by SSR, which results in higher photocatalytic activity. In a typical polymerizable complex reaction, the metal salt precursors of both A site and B site cations of a perovskite material are dissolved in an ethylene glycol (EG) and methanol mixed solution. Citric acid (CA) is added as a chelating agent to form metal-citrate complex compounds for metal cations stabilization. The solution is followed by heating at 373 - 403 K to promote polymerization process between EG and CA. The polymerization process can form long chains which isolate the metal cations. This process prevents the grain growth during the following heat treatment such as high temperature calcination. After several hours polymerization, a resin-like gel without any visible precipitates is obtained. The brown gel is heated at 673-773 K for several hours to remove residual solvents and burn out all the organics. The obtained powder is subsequently calcined at designated temperatures for better crystallinity and photocatalytic performance. Figure 3-3 shows a typical synthesis process of polymerizable complex method.

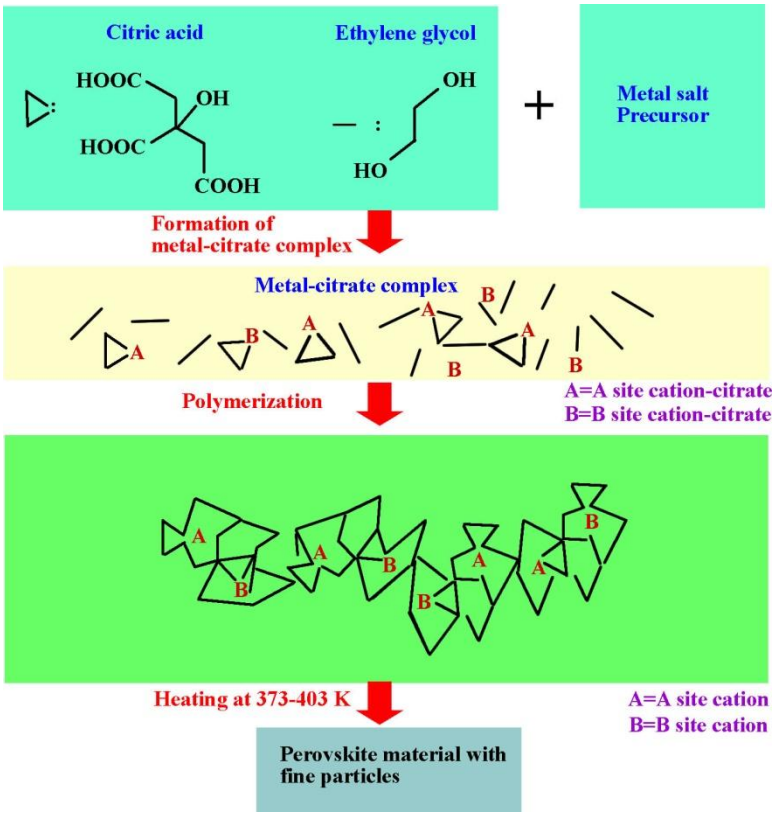

Figure 3-3 Polymerizable complex method for preparation of perovskite materials.

3.5 Treatment during the synthesis

3.5.1 Thermal treatment

Most perovskite structure materials need to be subjected to thermal treatment to promote relevant phase formation, better surface morphology and enhanced crystallinity.

Reaction of particles goes through three main steps during the thermal treatment. In the first step, particles agglomerate together and go through mass transfer from the convex to concave surfaces which result in decrease of the total pore volume and distance between particles. Second step includes atom diffusion into the lattice of the host materials. In this step, the density keeps increasing while the pore diameters and distances between particles decrease. During the final step, the materials undergo phase formation and grain growth. The final product with minimum vacancies is formed.

Thermal treatment can largely affect particle size, particle shape and packing behavior. The diffusion process (step 2) is the most important process since it relates nucleation as well as the

formation of the phases. The diffusion process happens faster in smaller particles because it can start at lower temperatures. Thus, thermal treatment is especially important to nanomaterials.

3.5.1.1 Calcination

Calcination is required for precursor decomposition and/or impurity degradation during synthesis. The decomposed products can be released in form of gas, such as H_2O, CO_2 and other gaseous products of degradation. Calcination is often performed under various atmospheres to facilitate precursor decomposition and/or impurity degradation include air, oxygen, ammonia, nitrous oxide and others. Other calcination conditions, for example, calcination temperature, calcination temperature ramping and calcination time, have significant influence on particle size, shape, surface area, crystallinity and phase purity of the synthesized materials.

Some preparation methods discussed above largely involve in organic components as solvents or chelate complex. The organic residuals on the surface also cause samples having different physical and chemical properties. The reactive and catalytic activity of the samples may decrease because of the organic residuals. These organic components need to be removed after synthesis. Therefore, calcination of the samples at 300-500 ℃ to remove these organic residues is necessary.

3.5.2 Drying

To yield fine multi-component single phase powders, two conditions need to be considered. Firstly, small particles need to be treated under low reaction and calcination temperatures because high temperatures can result in grain growth. Secondly, highly homogeneous, preferably on an atomic scale, precursor mixture solution is needed for better single phase formation. To preserve the homogeneity of the precursor solution and to avoid growth of large grains, solvents (such as water and ethanol) have to be removed under well controlled conditions.

Freezing and vacuum drying have been employed as an efficient method to remove solvents under low temperature as well as preserve the homogeneity of the precursor solution. Freezing is accomplished by using low temperature liquid (such as liquid nitrogen and liquid helium) to spray the solution to preserve the solution homogeneity. The process can be further controlled by selecting the suitable spraying method. Followed freezing process, vacuum drying is used to evaporate of the solvents which are more volatile. It must be carried out without back melting to prevent segregation of components and growth of large grains. The temperature needs to be

maintained at least as low as 208 K and the pressure is kept at less than 1 Pa to achieve ideal vacuum drying.

3.6 Strontium titanate based photocatalysts

Strontium titanate is one of the most widely studied perovskite materials due to its surpassing dielectric properties. Non-stoichiometric and isotopic substitution doped SrTiO3 has high ferroelectricity and is proved to be a good candidate for device applications [67]. Another promising field for strontium titanate is photocatalysis. Early in 1976, $SrTiO_3$ was proved to be an excellent photocatalyst for overall water splitting under UV irradiation due to its high stability and suitable band-edge positions [68]. Since then, $SrTiO_3$ has been extensively investigated by optimizing, for example, the reactant ion conditions [69], presence of co-catalyst [70-73], conditions of preparation methods [74-77], and concentrations of defects [78]; to improve its performance for photocatalysis.

A traditional method to synthesize $SrTiO_3$ is solid state reaction method. Strontium carbonate and titanium dioxide are mixed and ground together, and subsequently calcined at high temperature for more than 10 hours. $SrTiO_3$ synthesized by solid state reaction method has low surface areas, approximately 2 m^2/g, and low homogeneity due to local differences of starting materials [79]. Therefore, other synthesis method for $SrTiO_3$ have been attracted more and more attention. Polymerizable complex method provided an alternative method to synthesize $SrTiO_3$ with high purity and small particle size at low temperature [80]. Using this method of synthesis, pure perovskite $SrTiO_3$ was formed without any other intermediate species, suggesting that the molecular-scale mixing of cations in the Sr-Ti powder precursor was achieved [81].

Pristine $SrTiO_3$ has a bandgap of 3.2 eV which corresponds to the light wavelength of 387 nm [82]. From the viewpoint of practical applications, it is desirable to utilize visible light hence the bandgap needs to be smaller than 3.0 eV. To develop visible light responsive $SrTiO_3$, ion doping, co-catalyst and multi-component composites, as discussed above, have been extensively investigated.

Ion doping can shift the light absorption edge to visible region. However, the absorption of visible light does not necessarily indicate a formation of a good photocatalyst, although it is a necessary starting requirement to select a potentially promising materials [83]. For example, Cr^{3+} doped TiO_2 or $SrTiO_3$ can have enhanced visible light absorption, however, the improvement of photoactivity was not observed. The imbalanced charge in the crystal due to substitution of Ti^{4+}

with Cr^{3+} leads to formation of oxygen defects and/or to formation of Cr^{6+} ions, which stabilizes the charge balance. However, oxygen defects and Cr^{6+} ions might act as recombination centers for electrons, and therefore result in a decrease of photoactivity. Kudo et al. developed a series of codoped $SrTiO_3$ photocatalysts, such as (Cr,Sb)- codoped $SrTiO_3$ [83], (Cr,Ta)-codoped $SrTiO_3$ [84], and (Ni,Ta)-codoped $SrTiO_3$ [85], and used these materials to study visible-light driven photocatalytic H_2 evolution in methanol solution. (Cr,Sb)-codoped $SrTiO_3$ showed intense absorption bands in the visible light region and possessed 2.4 eV of energy gaps, respectively. The charge balance was kept by codoping of Sb^{5+} and Cr^{3+} ions, resulting in the suppression of formation of Cr^{6+} ions and oxygen defects in the lattice thus preventing a formation of non-radiative recombination centers between photogenerated electrons and holes [83]. Compared to Cr-doped $SrTiO_3$, (Cr,Ta)-codoped $SrTiO_3$ had a shorter induction period for photocatalytic reaction and showed higher photocatalytic activity. Konta et al. investigated noble metal (Ru, Rh, Ir) doped $SrTiO_3$ and attributed absorption bands in the visible light region to the formation of the intermediate band introduced by the noble metal dopants [13]. In a different study Pt and Rh doped $SrTiO_3$ have high activities under visible light irradiation in the presence of aqueous methanol solution as sacrificial reagent [86]. Takata et al. studied the doping of aliovalent metal cations to $SrTiO_3$ for photocatalytic overall water splitting. It was reported that doping with aliovalent metal cations brought distinct different effects in water splitting [85]. For example, Na^+ doping can effectively enhance the photocatalytic activity while doping of Ta^{5+} can largely suppress the photocatalytic activity. The reason might be that doping of Ta^{5+} introduced oxygen vacancies thus leading to higher photogenerated carrier recombination and lower visible light absorption.

Co-catalyst loading is another effective method to enhance the photocatalytic activity of $SrTiO_3$. Domen et al. studied $SrTiO_3$ loaded with Ni/NiO co-catalyst for the overall water splitting [72, 87]. In this photocatalyst, H_2 evolved on the surface of Ni/NiO co-catalyst and O_2 production occurred over $SrTiO_3$ surface. The metallic Ni severed as an interlayer between NiO and $SrTiO_3$, which effectively facilitated the electron transfer and therefore enhanced the photocatalytic activity. Other co-catalysts, such as noble metals co-catalysts, were also extensively employed to enhance photocatalytic activity of $SrTiO_3$ [13].

3.7 Summary

In summary, some major progress on the development of perovskite structure based photocatalysts for water splitting has been reported in literature. The literature analysis has indicated encouraging prospects of perovskite structure based photocatalysts and offered guidance for future research work. Modification of perovskite structure photocatalysts by combining different modification strategies is the most promising way forward, where optimizing (a) the absorption of photons, (b) formation of photogenerated charge carriers, (c) charge carriers separation and transport, (d) conditions of redox reactions can all lead to improve the photocatalytic performance. However, a development of perovskite structure based photocatalysts for overall water splitting and/or hydrogen evolution under visible-light irradiation remains a significant challenge. Further systematic and detailed work on the improvement of dynamic conditions (such as separation and migration of photogenerated charge carriers, and redox reactions), by optimizing reaction conditions and co-catalyst composition , are needed to achieve either the overall water splitting under visible-light irradiation or to improve the efficiency of hydrogen production. Development of new methods of synthesis and optimization of the existing methods for perovskite catalyst preparation should lead to improved photocatalytic activities in water splitting and hydrogen evolution.

References

[1] R.S. Roth, Classification of perovskite and other ABO_3 type compounds, Journal of Research of the National Bureau of Standards, 58 (1957) 75-88.

[2] T. Nitadori, T. Ichiki, M. Misono, Catalytic properties of perovskite type mixed oxides (ABO_3) consisting of rare-earth and 3D transition-metals: The roles of the A-site and B-site ions, Bulletin of the Chemical Society of Japan, 61 (1988) 621-626.

[3] A. Kudo, H. Kato, S. Nakagawa, Water splitting into H_2 and O_2 on new $Sr_2M_2O_7$ (M = Nb and Ta) photocatalysts with layered perovskite structures: Factors affecting the photocatalytic activity, Journal of Physical Chemistry B, 104 (2000) 571-575.

[4] H. Kato, A. Kudo, Photocatalytic water splitting into H_2 and O_2 over various tantalate photocatalysts, Catalysis Today, 78 (2003) 561-569.

[5] Y.A. Abramov, V.G. Tsirelson, V.E. Zavodnik, S.A. Ivanov, I.D. Brown, The chemical bond and atomic displacements in $SrTiO_3$ from x-ray diffraction analysis, Acta Crystallographica Section B-Structural Science, 51 (1995) 942-951.

[6] M.A. Pena, J.L.G. Fierro, Chemical structures and performance of perovskite oxides, Chemical Reviews, 101 (2001) 1981-2017.

[7] W.H. Lin, C. Cheng, C.C. Hu, H.S. Teng, $NaTaO_3$ photocatalysts of different crystalline structures for water splitting into H_2 and O_2, Applied Physics Letters, 89 (2006).

[8] C.C. Hu, Y.L. Lee, H.S. Teng, Efficient water splitting over $Na_{1-x}K_xTaO_3$ photocatalysts with cubic perovskite structure, Journal of Materials Chemistry, 21 (2011) 3824-3830.

[9] P. Li, S.X. Ouyang, G.C. Xi, T. Kako, J.H. Ye, The effects of crystal structure and electronic structure on photocatalytic H_2 evolution and CO_2 reduction over two phases of perovskite-structured $NaNbO_3$, Journal of Physical Chemistry C, 116 (2012) 7621-7628.

[10] M.S. Islam, Ionic transport in ABO_3 perovskite oxides: a computer modelling tour, Journal of Materials Chemistry, 10 (2000) 1027-1038.

[11] P.S. Pizani, E.R. Leite, F.M. Pontes, E.C. Paris, J.H. Rangel, E.J.H. Lee, E. Longo, P. Delega, J.A. Varela, Photoluminescence of disordered ABO_3 perovskites, Applied Physics Letters, 77 (2000) 824-826.

[12] S. Ahuja, T.R.N. Kutty, Nanoparticles of $SrTiO_3$ prepared by gel to crystallite conversion and their photocatalytic activity in the mineralization of phenol, Journal of Photochemistry and Photobiology A-Chemistry, 97 (1996) 99-107.

[13] R. Konta, T. Ishii, H. Kato, A. Kudo, Photocatalytic activities of noble metal ion doped $SrTiO_3$ under visible light irradiation, Journal of Physical Chemistry B, 108 (2004) 8992-8995.

[14] H. Kato, A. Kudo, Water splitting into H_2 and O_2 on alkali tantalate photocatalysts $ATaO_3$ (A = Li, Na, and K), Journal of Physical Chemistry B, 105 (2001) 4285-4292.

[15] J. Yin, Z.G. Zou, J.H. Ye, A novel series of the new visible-light-driven photocatalysts $MCo_{1/3}Nb_{2/3}O_3$ (M = Ca, Sr, and Ba) with special electronic structures, Journal of Physical Chemistry B, 107 (2003) 4936-4941.

[16] C. Li, K.C.K. Soh, P. Wu, Formability of ABO_3 perovskites, Journal of Alloys and Compounds, 372 (2004) 40-48.

[17] L.M. Feng, L.Q. Jiang, M. Zhu, H.B. Liu, X. Zhou, C.H. Li, Formability of ABO_3 cubic perovskites, Journal of Physics and Chemistry of Solids, 69 (2008) 967-974.

[18] J.J. Ding, J. Bao, S.N. Sun, Z.L. Luo, C. Gao, Combinatorial discovery of visible-light driven photocatalysts based on the ABO_3-type (A = Y, La, Nd, Sm, Eu, Gd, Dy, Yb, B = Al and In) binary oxides, Journal of Combinatorial Chemistry, 11 (2009) 523-526.

[19] J.W. Shi, L.J. Guo, ABO_3-based photocatalysts for water splitting, Progress in Natural Science-Materials International, 22 (2012) 592-615.

[20] S.D. Li, L.Q. Jing, W. Fu, L.B. Yang, B.F. Xin, H.G. Fu, Photoinduced charge property of nanosized perovskite-type $LaFeO_3$ and its relationships with photocatalytic activity under visible irradiation, Materials Research Bulletin, 42 (2007) 203-212.

[21] D.W. Hwang, H.G. Kirn, J.S. Lee, J. Kim, W. Li, S.H. Oh, Photocatalytic hydrogen production from water over m-doped $La_2Ti_2O_7$ (M = Cr, Fe) under visible light irradiation (lambda > 420 nm), Journal of Physical Chemistry B, 109 (2005) 2093-2102.

[22] H. Kato, K. Asakura, A. Kudo, Highly efficient water splitting into H_2 and O_2 over lanthanum-doped $NaTaO_3$ photocatalysts with high crystallinity and surface nanostructure, Journal of the American Chemical Society, 125 (2003) 3082-3089.

[23] S. Ikeda, M. Hara, J.N. Kondo, K. Domen, H. Takahashi, T. Okubo, M. Kakihana, Preparation of $K_2La_2Ti_3O_{10}$ by polymerized complex method and photocatalytic decomposition of water, Chemistry of Materials, 10 (1998) 72-77.

[24] Y. Ebina, T. Sasaki, M. Harada, M. Watanabe, Restacked perovskite nanosheets and their Pt-loaded materials as photocatalysts, Chemistry of Materials, 14 (2002) 4390-4395.

[25] J.W. Liu, G. Chen, Z.H. Li, Z.G. Zhang, Hydrothermal synthesis and photocatalytic properties of $ATaO_3$ and $ANbO_3$ (A = Na and K), International Journal of Hydrogen Energy, 32 (2007) 2269-2272.

[26] A. Kudo, Y. Miseki, Heterogeneous photocatalyst materials for water splitting, Chemical Society Reviews, 38 (2009) 253-278.

[27] D. Yamasita, T. Takata, M. Hara, J.N. Kondo, K. Domen, Recent progress of visible-light-driven heterogeneous photocatalysts for overall water splitting, Solid State Ionics, 172 (2004) 591-595.

[28] A. Kudo, Recent progress in the development of visible light-driven powdered photocatalysts for water splitting, International Journal of Hydrogen Energy, 32 (2007) 2673-2678.

[29] H. Jeong, T. Kim, D. Kim, K. Kim, Hydrogen production by the photocatalytic overall water splitting on $NiO/Sr_3Ti_2O_7$: Effect of preparation method, International Journal of Hydrogen Energy, 31 (2006) 1142-1146.

[30] C.C. Hu, H.S. Teng, Structural features of p-type semiconducting NiO as a co-catalyst for photocatalytic water splitting, Journal of Catalysis, 272 (2010) 1-8.

[31] K. Iizuka, T. Wato, Y. Miseki, K. Saito, A. Kudo, Photocatalytic reduction of carbon dioxide over Ag cocatalyst-Loaded $ALa_4Ti_4O_{15}$ (A = Ca, Sr, and Ba) using water as a reducing reagent, Journal of the American Chemical Society, 133 (2011) 20863-20868.

[32] V. Subramanian, R.K. Roeder, E.E. Wolf, Synthesis and UV-visible-light photoactivity of noble-metal-$SrTiO_3$ composites, Industrial & Engineering Chemistry Research, 45 (2006) 2187-2193.

[33] Y.W. Tai, J.S. Chen, C.C. Yang, B.Z. Wan, Preparation of nano-gold on $K_2La_2Ti_3O_{10}$ for producing hydrogen from photo-catalytic water splitting, Catalysis Today, 97 (2004) 95-101.

[34] J. Yoshimura, Y. Ebina, J. Kondo, K. Domen, A. Tanaka, Visible-light induced photocatalytic behavior of a layered perovskite type niobate, $RbPb_2Nb_3O_{10}$, Journal of Physical Chemistry, 97 (1993) 1970-1973.

[35] K. Shimizu, S. Itoh, T. Hatamachi, T. Kodama, M. Sato, K. Toda, Photocatalytic water splitting on Ni-intercalated Ruddlesden-Popper tantalate $H_2La_{2/3}Ta_2O_7$, Chemistry of Materials, 17 (2005) 5161-5166.

[36] J. Hensel, G. Wang, Y. Li, J.Z. Zhang, Synergistic effect of CdSe quantum dot sensitization and nitrogen doping of TiO_2 nanostructures for photoelectrochemical solar hydrogen generation, Nano Letters, 10 (2010) 478-483.

[37] S. Fukahori, H. Ichiura, T. Kitaoka, H. Tanaka, Capturing of bisphenol A photodecomposition intermediates by composite TiO_2-zeolite sheets, Applied Catalysis B-Environmental, 46 (2003) 453-462.

[38] S. Fukahori, H. Ichiura, T. Kitaoka, H. Tanaka, Photocatalytic decomposition of bisphenol A in water using composite TiO_2-Zeolite sheets prepared by a papermaking technique, Environmental Science & Technology, 37 (2003) 1048-1051.

[39] B. Gao, C. Peng, G.Z. Chen, G.L. Puma, Photo-electro-catalysis enhancement on carbon nanotubes/titanium dioxide (CNTs/TiO_2) composite prepared by a novel surfactant wrapping sol-gel method, Applied Catalysis B-Environmental, 85 (2008) 17-23.

[40] J. Zhang, J.H. Bang, C.C. Tang, P.V. Kamat, Tailored TiO_2-$SrTiO_3$ heterostructure nanotube arrays for improved photoelectrochemical performance, ACS Nano, 4 (2010) 387-395.

[41] H.W. Bai, J. Juay, Z.Y. Liu, X.X. Song, S.S. Lee, D.D. Sun, Hierarchical $SrTiO_3$/TiO_2 nanofibers heterostructures with high efficiency in photocatalytic H_2 generation, Applied Catalysis B-Environmental, 125 (2012) 367-374.

[42] Y. Yang, K. Lee, Y. Kado, P. Schmuki, Nb-doping of TiO_2/$SrTiO_3$ nanotubular heterostructures for enhanced photocatalytic water splitting, Electrochemistry Communications, 17 (2012) 56-59.

[43] J. Ng, S.P. Xu, X.W. Zhang, H.Y. Yang, D.D. Sun, Hybridized nanowires and cubes: A novel architecture of a heterojunctioned TiO_2/$SrTiO_3$ thin film for efficient water splitting, Advanced Functional Materials, 20 (2010) 4287-4294.

[44] J.H. Luo, P.A. Maggard, Hydrothermal synthesis and photocatalytic activities of $SrTiO_3$-coated Fe_2O_3 and $BiFeO_3$, Advanced Materials, 18 (2006) 514.

[45] S. Boumaza, A. Boudjemaa, A. Bouguelia, R. Bouarab, M. Trari, Visible light induced hydrogen evolution on new hetero-system $ZnFe_2O_4$/$SrTiO_3$, Applied Energy, 87 (2010) 2230-2236.

[46] A. Stein, S.W. Keller, T.E. Mallouk, Turning down the heat- Design and mechanism in solid state synthesis, Science, 259 (1993) 1558-1564.

[47] C. Racault, F. Langlais, R. Naslain, Solid-state synthesis and characterization of the ternary phase Ti_3SiC_2, Journal of Materials Science, 29 (1994) 3384-3392.
[48] A. Kudo, Development of photocatalyst materials for water splitting with the aim at photon energy conversion, Journal of the Ceramic Society of Japan, 109 (2001) S81-S88.
[49] L. Zhou, W.Z. Wang, S.W. Liu, L.S. Zhang, H.L. Xu, W. Zhu, A sonochemical route to visible-light-driven high-activity $BiVO_4$ photocatalyst, Journal of Molecular Catalysis a-Chemical, 252 (2006) 120-124.
[50] M.Y. K. Byrappa, Handbook of Hydrothermal Technology-A Technology for Crystal Growth and Materials Processing, first ed., William Andrew Publishing, New York, 2001.
[51] H.B. Yin, Y. Wada, T. Kitamura, S. Kambe, S. Murasawa, H. Mori, T. Sakata, S. Yanagida, Hydrothermal synthesis of nanosized anatase and rutile TiO_2 using amorphous phase TiO_2, Journal of Materials Chemistry, 11 (2001) 1694-1703.
[52] J.G. Yu, L.J. Zhang, B. Cheng, Y.R. Su, Hydrothermal preparation and photocatalytic activity of hierarchically sponge-like macro-/mesoporous titania, Journal of Physical Chemistry C, 111 (2007) 10582-10589.
[53] J.G. Yu, X.X. Yu, Hydrothermal synthesis and photocatalytic activity of zinc oxide hollow spheres, Environmental Science & Technology, 42 (2008) 4902-4907.
[54] C. Zhang, Y.F. Zhu, Synthesis of square Bi_2WO_6 nanoplates as high-activity visible-light-driven photocatalysts, Chemistry of Materials, 17 (2005) 3537-3545.
[55] Y. Cong, J.L. Zhang, F. Chen, M. Anpo, Synthesis and characterization of nitrogen-doped TiO_2 nanophotocatalyst with high visible light activity, Journal of Physical Chemistry C, 111 (2007) 6976-6982.
[56] D. Chen, J.H. Ye, $SrSnO_3$ nanostructures: Synthesis, characterization, and photocatalytic properties, Chemistry of Materials, 19 (2007) 4585-4591.
[57] Q.P. Ding, Y.P. Yuan, X. Xiong, R.P. Li, H.B. Huang, Z.S. Li, T. Yu, Z.G. Zou, S.G. Yang, Enhanced photocatalytic water splitting properties of $KNbO_3$ nanowires synthesized through hydrothermal method, Journal of Physical Chemistry C, 112 (2008) 18846-18848.
[58] H. Yu, S.X. Ouyang, S.C. Yan, Z.S. Li, T. Yu, Z.G. Zou, Sol-gel hydrothermal synthesis of visible-light-driven Cr-doped $SrTiO_3$ for efficient hydrogen production, Journal of Materials Chemistry, 21 (2011) 11347-11351.

[59] X. Chen, S.S. Mao, Titanium dioxide nanomaterials: Synthesis, properties, modifications, and applications, Chemical Reviews, 107 (2007) 2891-2959.

[60] T. Kasuga, M. Hiramatsu, A. Hoson, T. Sekino, K. Niihara, Formation of titanium oxide nanotube, Langmuir, 14 (1998) 3160-3163.

[61] Y. Miseki, H. Kato, A. Kudo, Water splitting into H_2 and O_2 over niobate and titanate photocatalysts with (111) plane-type layered perovskite structure, Energy & Environmental Science, 2 (2009) 306-314.

[62] Z.H. Li, G. Chen, X.J. Tian, Y.X. Li, Photocatalytic property of $La_2Ti_2O_7$ synthesized by the mineralization polymerizable complex method, Materials Research Bulletin, 43 (2008) 1781-1788.

[63] Y. Yamashita, M. Tada, M. Kakihana, M. Osada, K. Yoshida, Synthesis of RuO_2-loaded $BaTinO_{2n+1}$ (n=1, 2 and 5) using a polymerizable complex method and its photocatalytic activity for the decomposition of water, Journal of Materials Chemistry, 12 (2002) 1782-1786.

[64] Y.P. Yuan, Z.Y. Zhao, J. Zheng, M. Yang, L.G. Qiu, Z.S. Li, Z.G. Zou, Polymerizable complex synthesis of $BaZr_{1-x}Sn_xO_3$ photocatalysts: Role of Sn^{4+} in the band structure and their photocatalytic water splitting activities, Journal of Materials Chemistry, 20 (2010) 6772-6779.

[65] S. Ikeda, M. Hara, J.N. Kondo, K. Domen, H. Takahashi, T. Okubo, M. Kakihana, Preparation of a high active photocatalyst, $K_2La_2Ti_3O_{10}$, by polymerized complex method and its photocatalytic activity of water splitting, Journal of Materials Research, 13 (1998) 852-855.

[66] H. Takahashi, M. Kakihana, Y. Yamashita, K. Yoshida, S. Ikeda, M. Hara, K. Domen, Synthesis of NiO-loaded $KTiNbO_5$ photocatalysts by a novel polymerizable complex method, Journal of Alloys and Compounds, 285 (1999) 77-81.

[67] J.H. Haeni, P. Irvin, W. Chang, R. Uecker, P. Reiche, Y.L. Li, S. Choudhury, W. Tian, M.E. Hawley, B. Craigo, A.K. Tagantsev, X.Q. Pan, S.K. Streiffer, L.Q. Chen, S.W. Kirchoefer, J. Levy, D.G. Schlom, Room-temperature ferroelectricity in strained $SrTiO_3$, Nature, 430 (2004) 758-761.

[68] M.S. Wrighton, A.B. Ellis, P.T. Wolczanski, D.L. Morse, H.B. Abrahamson, D.S. Ginley, Strontium titanate photoelectrodes- Efficient photoassisted electrolysis of water at zero applied potential, Journal of the American Chemical Society, 98 (1976) 2774-2779.

[69] F.T. Wagner, G.A. Somorjai, Photocatalytic hydrogen production from water on Pt free $SrTiO_3$ in alkali hydroxide solutions, Nature, 285 (1980) 559-560.

[70] Y. Sasaki, A. Iwase, H. Kato, A. Kudo, The effect of co-catalyst for Z-scheme photocatalysis systems with an Fe^{3+}/Fe^{2+} electron mediator on overall water splitting under visible light irradiation, Journal of Catalysis, 259 (2008) 133-137.

[71] G.Y. Wang, Y.J. Wang, B.J. Song, Y.Q. Xu, Performance of photocatalytic decomposition of water into hydrogen over Co-$SrTiO_3$, Chinese Journal of Inorganic Chemistry, 19 (2003) 988-992.

[72] K. Domen, A. Kudo, T. Onishi, Mechanism of photocatalytic decomposition of water into H_2 and O_2 over NiO-$SrTiO_3$, Journal of Catalysis, 102 (1986) 92-98.

[73] K. Domen, S. Naito, M. Soma, T. Onishi, K. Tamaru, Photocatalytic decomposition of water vapor on an NiO-$SrTiO_3$ catalyst, Journal of the Chemical Society-Chemical Communications, (1980) 543-544.

[74] H. Xu, S. Wei, H. Wang, M. Zhu, R. Yu, H. Yan, Preparation of shape controlled $SrTiO_3$ crystallites by sol-gel-hydrothermal method, Journal of Crystal Growth, 292 (2006) 159-164.

[75] J.S. Wang, S. Yin, M. Komatsu, Q.W. Zhang, F. Saito, T. Sato, Preparation and characterization of nitrogen doped $SrTiO_3$ photocatalyst, Journal of Photochemistry and Photobiology A-Chemistry, 165 (2004) 149-156.

[76] L. Chen, S. Zhang, L. Wang, D. Xue, S. Yin, Preparation and photocatalytic properties of strontium titanate powders via sol-gel process, Journal of Crystal Growth, 311 (2009) 746-748.

[77] T. Xian, H. Yang, J.F. Dai, Z.Q. Wei, J.Y. Ma, W.J. Feng, Photocatalytic properties of $SrTiO_3$ nanoparticles prepared by a polyacrylamide gel route, Materials Letters, 65 (2011) 3254-3257.

[78] T. Takata, K. Domen, Defect engineering of photocatalysts by doping of aliovalent metal cations for efficient water splitting, Journal of Physical Chemistry C, 113 (2009) 19386-19388.

[79] F.A. Rabuffetti, P.C. Stair, K.R. Poeppelmeier, Synthesis-dependent surface acidity and structure of $SrTiO_3$ nanoparticles, Journal of Physical Chemistry C, 114 (2010) 11056-11067.

[80] Y. Liu, L. Xie, Y. Li, R. Yang, J. Qu, Y. Li, X. Li, Synthesis and high photocatalytic hydrogen production of SrTiO3 nanoparticles from water splitting under UV irradiation, Journal of Power Sources, 183 (2008) 701-707.

[81] M. Kakihana, T. Okubo, M. Arima, Y. Nakamura, M. Yashima, M. Yoshimura, Polymerized complex route to the synthesis of pure $SrTiO_3$ at reduced temperatures: Implication

for formation of Sr-Ti heterometallic citric acid complex, Journal of Sol-Gel Science and Technology, 12 (1998) 95-109.

[82] C.H. Chang, Y.H. Shen, Synthesis and characterizations of chromium doped $SrTiO_3$ photocatalyst, Materials Letters, 60 (2006) 129-132.

[83] H. Kato, A. Kudo, Visible-light-response and photocatalytic activities of TiO_2 and $SrTiO_3$ photocatalysts codoped with antimony and chromium, Journal of Physical Chemistry B, 106 (2002) 5029-5034.

[84] T. Ishii, H. Kato, A. Kudo, H_2 evolution from an aqueous methanol solution on $SrTiO_3$ photocatalysts codoped with chromium and tantalum ions under visible light irradiation, Journal of Photochemistry and Photobiology A-Chemistry, 163 (2004) 181-186.

[85] R. Niishiro, H. Kato, A. Kudo, Nickel and either tantalum or niobium-codoped TiO_2 and $SrTiO_3$ photocatalysts with visible-light response for H_2 or O_2 evolution from aqueous solutions, Physical Chemistry Chemical Physics, 7 (2005) 2241-2245.

[86] S.W. Bae, P.H. Borse, J.S. Lee, Dopant dependent band gap tailoring of hydrothermally prepared cubic $SrTi_xM_{1-x}O_3$ (M=Ru,Rh,Ir,Pt,Pd) nanoparticles as visible light photocatalysts, Applied Physics Letters, 92 (2008) 104107.

[87] K. Domen, A. Kudo, T. Onishi, N. Kosugi, H. Kuroda, Photocatalytic decomposition of water into H_2 and O_2 over NiO-$SrTiO_3$ powder. 1. Structure of the catalyst, Journal of Physical Chemistry, 90 (1986) 292-295.

Chapter 4

Development of Noble Metal Nanoparticles for Photocatalytic Water Splitting and Hydrogen Evolution

4.1 Chapter introduction

Noble metal nanoparticles have received attention with the number of publications still growing exponentially (Figure 4-1).

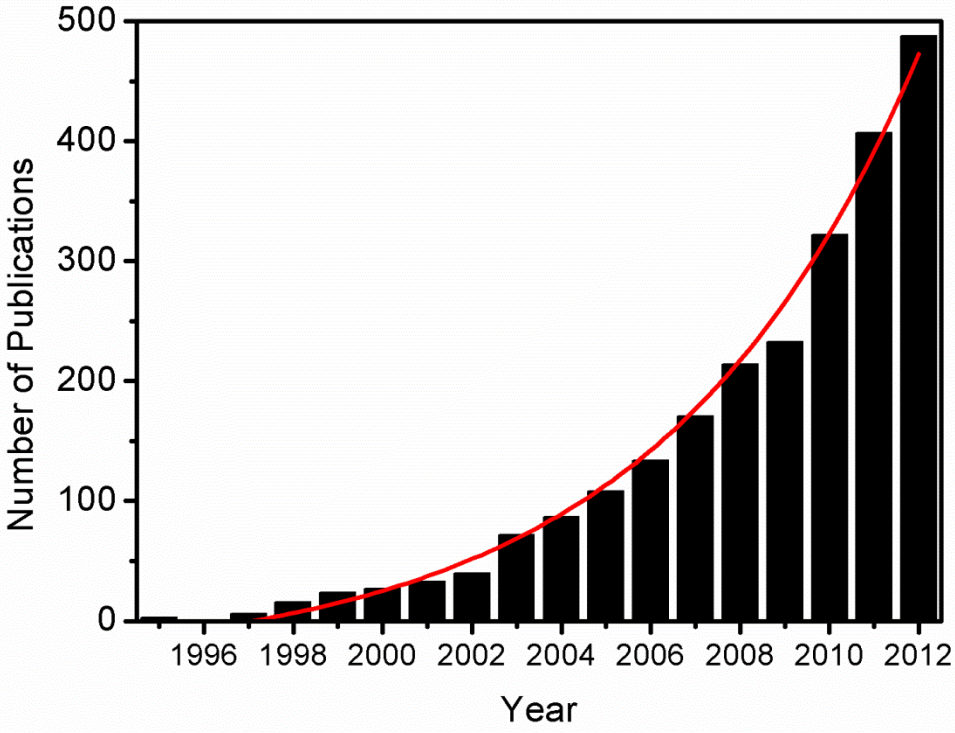

Figure 4-1 Number of publications on noble metal nanoparticles from 1994-2012. (Source: Web of knowledge; Search key word: noble metal nanoparticles).

These studies focused on different aspects of nanoparticles, including synthesis, characterization and applications of nanoparticles of various sizes for both noble and non-noble metal nanoparticles. More specifically, the cited references provided discussion of synthesis methods [1-5], shapes [6-8], optical and electronic properties [9-13] and core-shell properties [14-17] of noble metal nanoparticles. Despite the fact that this literature has focused primarily on synthesis aspects, still new and/or modified synthetic techniques are urgently needed to achieve a precise control of size, shape and monodispersity. There is also more and more attention being given to extremely small metal particles where electronic confinement effects start playing a significant role as opposed to only specific surface area effects. Depending on the size range of metal nanoparticles, they can exhibit strong quantum confinement effect and surface plasmon resonance [18-22].

Since interface plays an important role in electronic confinement and surface effect, various coupling structures of metal nanoparticles were investigated such as metal nanoparticles-semiconductor system, bimetallic system and metal nanoparticles-polymer system. Among these heterostructures, noble metal-semiconductor material is very promising for photocatalysis. Noble metal in contact with a semiconductor can greatly improve the interfacial charge-transfer process, resulting in enhancement of photocatalytic activity. Since the noble metal nanoparticles are anchored on the surfaces of the semiconductors, the sizes and shapes of the metal nanoparticles can significantly affect the amount of the active sites and carriers transfer routes. Different particle sizes, shapes and semiconductor supports have been extensively investigated. Among many different types of nanoparticles, sub-nanometer size metal clusters which consist of several metal atoms to tens metal atoms, have generated an enormous interest due to their unique electronic structures.

In this chapter, recent advances in noble metal nanoparticles, including the mechanism, synthetic methods and their potential applications are discussed.

4.1.1 Nanoparticles

What are nanoparticles? There is no particular definition for nanoparticles. Nano actually comes from the Greek word "nanos" which means dwarf or extremely small in size. The internationally accepted definition is that any particle which has at least one dimension less than 100 nm is called a nanoparticle [23].

4.1.2 Quantum confinement effect

One important question is what would happen to particles when the particle size decreases down to the size range where quantum confinement effects starts to play a significant role [24]. Particles with diameters in the order of several nanometers exhibit unique size-dependent properties due to the quantum size effect, which can drastically alter electronic properties. In the conventional infinite-depth well model [25], the excitation energy level E1n of an ultra-small particle with radius R is a function of the bandgap energy Eg of bulk semiconductor and kinetic energy. The kinetic energy can be calculated as the energy of a particle in a box having a spherically symmetric square well potential of infinite depth:

$$\mathrm{E1n} = \mathrm{Eg} + \left(\frac{\delta^2}{2\varphi \mathrm{R}^2}\right) \emptyset^2 \qquad (4\text{-}1)$$

In Equation 4-1, φ is the reduced, effective mass of the conduction band electron and valence band hole, ∅ is the nth root of the spherical Bessel function. The equation indicates that the bandgap of nanosized particles ($\leq$6nm) is larger than that of materials bulk, and the gap increases with decreasing particle size. Thus, nanoparticles show the unique properties, which are different from those of bulk materials. Decreasing the particles size also leads to an increase in surface area and to altering the mechanical, thermal and catalytic properties [26].

4.1.3 Surface plasmon resonance

Free electrons in the metal can travel through the material. The mean free path in gold and silver is ~50 nm [27]. In particles smaller than ~50nm, no scattering is expected from the bulk. This means interactions with the surface dominate [28]. When the wavelength of light is much larger than the nanoparticle size it sets up standing resonance conditions. Light in resonance with the surface plasmon oscillation causes the free electrons in the metal to oscillate. As the wave front of the light passes, the electron density in the particle is polarized to one surface and oscillates in resonance with the light's frequency causing a standing oscillation [29]. The resonance condition is determined from absorption and scattering spectroscopy and is found to depend on the shape, size, and dielectric constants of both the metal and the surrounding material. This is referred to as the surface plasmon resonance, since it is located at the surface. As the shape or size of the nanoparticle changes, the surface geometry changes, causing a shift in the electric field density on the surface. This causes a change in the oscillation frequency of the electrons, generating different cross-sections for the optical properties including absorption and scattering [30]. Moreover, light absorption is a local effect, limited to the noble metal particles so that the light only heats the noble metal NPs which generally account for a few percent of the overall catalyst mass to elevated temperature, while the reaction system remains at temperatures close to the ambient temperature. Therefore, such a process will require much lesser energy input to catalyze reactions.

4.2 Synthesis methods of noble metal nanoparticles

4.2.1 Seeding technique

The seeding technique is a popular method for generation of large spherical and non-spherical nanoparticles [31]. A chemical reducing agent is used, where small, generally spherical nanoparticles are first generated and then added to a growth solution with more metal ions and surfactant to induce anisotropic growth. The seeds are generated with a strong reducing agent, such as sodium borohydride. The growth solution employs a weaker reducing agent (often ascorbic acid) to reduce the metal salt to an intermediate state so that only catalyzed reduction on the nanoparticle surface is allowed. Proper seed, salt, and stabilizer concentrations are adjusted to generate nanoparticles with various sizes. Counter ions and additives have also been found to play a role in directing growth and the final shape of nanoparticles obtained.

4.2.2 Two-phase reaction

Two-phase reaction has been extensively used and studied for synthesis of nanoparticles with very small sizes (1-5nm) and narrow dispersity [32-35]. The particles are stabilized by a noble metal-thiol bonds [36]. Samples generated with the two-phase method are stable for long periods of time when dry and can easily be redispersed in many organic solvents. In synthesis, the noble metal salt is first transferred to the organic phase using a suitable surfactant. Nanoparticles formation can be monitored by color change from orange to deep brown. The ratio of noble metal salt to surfactant and the reaction temperature control particle size and dispersity. This synthetic procedure is often referred to as generating monolayer-protected clusters (MPCs) due to the monolayer coverage of the sulfur groups and the small size of nanoparticles generated. Many improvements to this synthesis procedure have been reported to generate small monodisperse gold nanoparticles.

4.2.3 Inverse micelle method

Inverse micelles have been used to generate many different sizes and shapes of nanoparticles [37-39]. By utilizing the different polarity of the surfactants and water, inverse micelles can create small cages, where the dedicated materials can diffuse in and form a certain shape. Single crystal, monodisperse nanoparticles can be generated in inverse micelles by using a metal salt conjugated to the surfactant prior to the addition of the reducing agent. The inverse micelles normally yields good monodispersity of nanoparticles, and can be used for many different materials.

4.3 Catalytic applications of noble metal nanoparticles

In the 1980s Haruta et al. reported that supported gold catalysts could exhibit the activity to oxidize CO at very low temperatures, significantly below 273K [40]. This discovery started the rapid growth in studies relating to heterogeneous catalysis with noble metal NPs. Since then, many research groups have prepared noble metal NPs and studied their catalytic activities for various catalytic applications under different conditions, these studies including Au [41-46], Pt [47-49] and Pd [50].

CO oxidation reaction is still a major application of noble metal NPs. Recent research has focused on the effect of the supports for noble metals. Various substrates, such as α-Fe_2O_3 [40], TiO2 [41], metal-organic framework [42], carbon [47] and zeolite [49] were proved to be good candidates for noble metal CO oxidation reaction. These reports indicated the interaction between noble metals and the substrate is essential for catalytic activity enhancement. It is also crucial to understand the size effect in CO oxidation. For example, Grunwaldt et al. investigated the gold catalysts on TiO_2 and ZrO_2 for CO oxidation [51]. By controlling the Au NPs average size and depositing these Au NPs onto different support, they found different catalytic activities, suggesting that both noble metal NPs size and the support play key roles in CO oxidation.

Photocatalytic oxidation of organic compounds is another promising application of noble metal NPs. Electron-hole pairs are produced when a semiconductor is illuminated by the light. The photogenerated electron-hole pairs can subsequently degrade some organic compounds [52, 53]. Noble metals were found to be good candidates to further enhance the photocatalytic activity for organic compound oxidization reaction. Since the first discovery in this field, extensive reports have been published on enhancement of photocatalytic organic compound oxidation efficiency, conversion rate and selectivity with the existence of noble metals [54-61]. Zheng et al. reported an enhancement factor of 6.3 times of photocatalytic degradation of methyl orange under UV light irradiation when TiO_2 was loaded with Ag [62]. The enhance photocatalytic activity might come from the efficient charge separation attributed to Ag NPs. Pt and Au were reported to play important roles when loaded with TiO_2 for methylene blue photodegradation [63, 64]. The reason for the enhancement in this study was attributed to the photogenerated electrons being trapped by Pt and Au, resulting more efficient charge separation.

Third, noble metals can work as excellent co-catalyst for photocatalytic water splitting and hydrogen production reactions. Since the first successful demonstration of photocatalytic water

splitting by using Pt/TiO_2 photocatalyst reported by Fujishima and Honda, noble metals have attracted a growing attention in photocatalyst development for photocatalytic water splitting and hydrogen evolution studies. Various noble metals, sizes, structures and noble metal-semiconductor coupling system have been extensively investigated. Liu et al. investigated the effect Ag loading on $SrTiO_3$ for photocatalytic activity enhancement [65]. Subramanian et al. reported Au and Ag NPs could capture and store the photogenerated electrons, therefore enhanced the photocurrent of TiO_2 under UV-light irradiation [66]. Miseki et al. observed the photocatalytic activity improvement when different photocatalysts loaded with Au NPs, including titanate, niobate and tantalite photocatalysts [67].

4.4 Enhancement mechanism of noble metal NPs

Noble metal NPs can enhance the photocatalytic activity. This phenomenon has been proved by various different photocatalytic applications as discussed above. The reason for photocatalytic activity enhancement of noble metal NPs can be various. One of the main reasons attributes to the easier electron transition within the energy levels of noble metals and charge carrier separation at the interface of noble metal and semiconductor. The energy levels of bulk noble metals are considered as continuous levels filled up to Fermi level. However, the energy levels of noble metal nanoparticles may become discrete depend on the particle size. The higher electron energy levels are often unoccupied. When noble metal is illuminated by the light, the electrons transition from the conduction band to empty orbital levels or vacuum level can take place, therefore creating electron-hole pairs in the noble metals. These electrons and holes can also participate in redox reactions, resulting in higher photocatalytic activities. In addition, noble metals can work as a charge separator for photogenerated charge carriers. When a noble metal-semiconductor heterostructure system is illuminated by the light, the electrons generated from the semiconductors can move from the conduction band of the semiconductor to the noble metal NPs, while the photogenerated holes leave in the semiconductor. This mechanism helps to separate the charge carriers to minimize the recombination.

4.5 Important factors to affect the catalytic activities

4.5.1 Particle size

Significant catalytic activity enhancement was observed with noble metal particles, which was discussed in the previous chapters. Among these catalytic activity enhancement reports,

small noble metal NPs were found to have extraordinary activities. For instance, CO oxidation rate for 2 to 4 nm Au nanoparticles was more than two orders of magnitude higher than for 20 to 30 nm particles [68]. The proposed mechanism was when the gold particle size decreased, the concentration of low-coordinated Au atoms increased which were considered more active. Further evidences for the particle size effect were obtained by other related studies, such as CO oxidation [69, 70]. In these studies Au clusters supported on TiO_2 thin films were prepared under ultra-high vacuum conditions with average metal cluster sizes that varied from 2.5 to 6.0 nm, while the catalytic activity measurements were performed in a reactor contiguous to the surface analysis chamber. The rates of reaction were dependent on the Au particle size and the Au with 3.2 nm achieved the highest activity[70].

4.5.2 Support

The support of noble metal NPs has been found to be important in determining the catalytic activity. TiO_2 is a widely used support because of its good stability, simple preparation method and relatively low cost. There is a number of reports on using TiO_2 as an effective support, focused on different applications discussed above, including CO oxidation, photocatalytic organic compound degradation and photocatalytic water splitting and hydrogen evolution. However, TiO_2 has a large bandgap (> 3.0 eV) thus make it a challenge to utilize visible light for photocatalytic applications. Other oxides, for example, CeO2 and Mn_2O_3 were studied for their compatibilities with noble metal NPs [71, 72]. Both of them exhibited high activities for low temperature CO oxidation. $SrTiO_3$ was employed as a support for noble metals for photocatalytic water splitting and hydrogen evolution. The enhanced activity can be contributed to the interfacial behavior of noble-metal NPs and $SrTiO_3$, as discussed detailedly in Chapter 3.3.2.

Interestingly, some conclusions for support performance in catalytic enhancement were not exactly consistent. For instance, Ribeiro et al. reported Au/ZrO_2 showed more than 30 % CO conversion rate at 273 K [73], however, in Grunwaldt et al. research, Au/ZrO_2 only reached about 10 % CO conversion rate [51]. The discrepancy could come from different $Au\text{-}ZrO_2$ interfacial behaviors, which resulted from different preparation methods of samples. Thus, understanding and optimization of the support is very important for noble metal catalytic activity enhancement.

4.5.3 Shape

Noble metal nanoparticles with different shapes have been synthesized [6, 8, 74-78]. Nanorods have attracted the most attention, due to the ease of preparation, the large number of synthetic methods available, the high monodispersity possible, and the rational control over the aspect ratio, which is primarily responsible for the change in their optical properties [79-82]. The two plasmon resonances of nanorods are due to the transverse oscillation of the electrons [83]. The transverse surface plasmon resonance does not depend on the aspect ratio and is at the same wavelength as the plasmon resonance of spheres. The longitudinal surface plasmon resonance increases with larger aspect ratios. The anisotropy has been shown to generate large control over the optical absorbance for all shapes generated [74]. Triangular nanoparticles have been generated by photochemical means and chemical growth [84-86]. Arrays of triangular nanoparticles can also be synthesized with nanosphere lithography. The edges and corners are very important with triangular nanoparticles. Snipping of the edges produces a visible blue shift in the plasmon resonance, which can be modeled theoretically [87]. Disks also display a similar plasmon resonance absorption dependence on their aspect ratio and low coordinated atoms [88].

4.6 Summary

The noble metal NPs, with proper control of the particle size and the suitable selection of oxide support materials, have been found to be very active catalysts for oxidation, selective oxidation and photocatalytic water splitting and hydrogen evolution reactions. Fundamental research aiming at interpreting good catalytic activity and selectivity of noble metal materials at an atomic scale is also invaluable for understanding the photocatalytic properties of noble metal NPs, as the combination of the catalytic activity and the light absorption property of noble metal NPs creates great opportunity for a new class of photocatalysts. These properties make the photocatalysts attractive for applications over a wide range from final chemical synthesis, environmental remediation and renewable energy production.

References

[1] C.L. Haynes, R.P. Van Duyne, Nanosphere lithography: A versatile nanofabrication tool for studies of size-dependent nanoparticle optics, Journal of Physical Chemistry B, 105 (2001) 5599-5611.

[2] X.H. Huang, S. Neretina, M.A. El-Sayed, Gold nanorods: from synthesis and properties to biological and biomedical applications, Advanced Materials, 21 (2009) 4880-4910.

[3] E. Hao, G.C. Schatz, J.T. Hupp, Synthesis and optical properties of anisotropic metal nanoparticles, Journal of Fluorescence, 14 (2004) 331-341.

[4] X.M. Lu, M. Rycenga, S.E. Skrabalak, B. Wiley, Y.N. Xia, Chemical synthesis of novel plasmonic nanoparticles, in: Annual Review of Physical Chemistry, 2009, pp. 167-192.

[5] K.B. Narayanan, N. Sakthivel, Biological synthesis of metal nanoparticles by microbes, Advances in Colloid and Interface Science, 156 (2010) 1-13.

[6] A.R. Tao, S. Habas, P.D. Yang, Shape control of colloidal metal nanocrystals, Small, 4 (2008) 310-325.

[7] K.S. Lee, M.A. El-Sayed, Gold and silver nanoparticles in sensing and imaging: Sensitivity of plasmon response to size, shape, and metal composition, Journal of Physical Chemistry B, 110 (2006) 19220-19225.

[8] T. Jensen, L. Kelly, A. Lazarides, G.C. Schatz, Electrodynamics of noble metal nanoparticles and nanoparticle clusters, Journal of Cluster Science, 10 (1999) 295-317.

[9] J. Zheng, P.R. Nicovich, R.M. Dickson, Highly fluorescent noble-metal quantum dots, Annual Review of Physical Chemistry, 58 (2007) 409-431.

[10] L.L. Zhao, K.L. Kelly, G.C. Schatz, The extinction spectra of silver nanoparticle arrays: Influence of array structure on plasmon resonance wavelength and width, Journal of Physical Chemistry B, 107 (2003) 7343-7350.

[11] S.A. Maier, P.G. Kik, H.A. Atwater, Optical pulse propagation in metal nanoparticle chain waveguides, Physical Review B, 67 (2003).

[12] J. Zheng, C.W. Zhang, R.M. Dickson, Highly fluorescent, water-soluble, size-tunable gold quantum dots, Physical Review Letters, 93 (2004).

[13] W.P. Zhou, A. Lewera, R. Larsen, R.I. Masel, P.S. Bagus, A. Wieckowski, Size effects in electronic and catalytic properties of unsupported palladium nanoparticles in electrooxidation of formic acid, Journal of Physical Chemistry B, 110 (2006) 13393-13398.

[14] P. Mani, R. Srivastava, P. Strasser, Dealloyed Pt-Cu core-shell nanoparticle electrocatalysts for use in PEM fuel cell cathodes, Journal of Physical Chemistry C, 112 (2008) 2770-2778.

[15] S. Koh, P. Strasser, Electrocatalysis on bimetallic surfaces: Modifying catalytic reactivity for oxygen reduction by voltammetric surface dealloying, Journal of the American Chemical Society, 129 (2007) 12624-12625.

[16] J. Zhang, F.H.B. Lima, M.H. Shao, K. Sasaki, J.X. Wang, J. Hanson, R.R. Adzic, Platinum monolayer on nonnoble metal-noble metal core-shell nanoparticle electrocatalysts for O_2 reduction, Journal of Physical Chemistry B, 109 (2005) 22701-22704.

[17] T. Endo, K. Kerman, N. Nagatani, H.M. Hiepa, D.K. Kim, Y. Yonezawa, K. Nakano, E. Tamiya, Multiple label-free detection of antigen-antibody reaction using localized surface plasmon resonance-based core-shell structured nanoparticle layer nanochip, Analytical Chemistry, 78 (2006) 6465-6475.

[18] H. Tada, T. Kiyonaga, S. Naya, Rational design and applications of highly efficient reaction systems photocatalyzed by noble metal nanoparticle-loaded titanium(IV) dioxide, Chemical Society Reviews, 38 (2009) 1849-1858.

[19] H.B. Zeng, P.S. Liu, W.P. Cai, S.K. Yang, X.X. Xu, Controllable Pt/ZnO porous nanocages with Improved photocatalytic activity, Journal of Physical Chemistry C, 112 (2008) 19620-19624.

[20] W.B. Hou, W.H. Hung, P. Pavaskar, A. Goeppert, M. Aykol, S.B. Cronin, Photocatalytic conversion of CO_2 to hydrocarbon fuels via plasmon-enhanced absorption and metallic interband transitions, Acs Catalysis, 1 (2011) 929-936.

[21] X.J. Lv, W.F. Fu, H.X. Chang, H. Zhang, J.S. Cheng, G.J. Zhang, Y. Song, C.Y. Hu, J.H. Li, Hydrogen evolution from water using semiconductor nanoparticle/graphene composite photocatalysts without noble metals, Journal of Materials Chemistry, 22 (2012) 1539-1546.

[22] X.D. Wang, R.A. Caruso, Enhancing photocatalytic activity of titania materials by using porous structures and the addition of gold nanoparticles, Journal of Materials Chemistry, 21 (2011) 20-28.

[23] N.L. Rosi, C.A. Mirkin, Nanostructures in biodiagnostics, Chemical Reviews, 105 (2005) 1547-1562.

[24] Y. Wang, N. Herron, Nanometer-sized semiconductor clusters - materials synthesis, quantum size effects, and photophysical properties, Journal of Physical Chemistry, 95 (1991) 525-532.
[25] A.L. Efros, Interband absorption of light in a semiconductor sphere, Soviet Physics Semiconductors-Ussr, 16 (1982) 772-775.
[26] A.H. Castro Neto, F. Guinea, N.M.R. Peres, K.S. Novoselov, A.K. Geim, The electronic properties of graphene, Reviews of Modern Physics, 81 (2009) 109-162.
[27] J.H. Adair, T. Li, T. Kido, K. Havey, J. Moon, J. Mecholsky, A. Morrone, D.R. Talham, M.H. Ludwig, L. Wang, Recent developments in the preparation and properties of nanometer-size spherical and platelet-shaped particles and composite particles, Materials Science & Engineering R-Reports, 23 (1998) 139-242.
[28] A.J. Haes, R.P. Van Duyne, A nanoscale optical blosensor: Sensitivity and selectivity of an approach based on the localized surface plasmon resonance spectroscopy of triangular silver nanoparticles, Journal of the American Chemical Society, 124 (2002) 10596-10604.
[29] S. Link, M.A. El-Sayed, Size and temperature dependence of the plasmon absorption of colloidal gold nanoparticles, Journal of Physical Chemistry B, 103 (1999) 4212-4217.
[30] P.K. Jain, X.H. Huang, I.H. El-Sayed, M.A. El-Sayed, Noble metals on the nanoscale: optical and photothermal properties and some applications in imaging, sensing, biology, and medicine, Accounts of Chemical Research, 41 (2008) 1578-1586.
[31] C.J. Murphy, T.K. San, A.M. Gole, C.J. Orendorff, J.X. Gao, L. Gou, S.E. Hunyadi, T. Li, Anisotropic metal nanoparticles: Synthesis, assembly, and optical applications, Journal of Physical Chemistry B, 109 (2005) 13857-13870.
[32] Y.J. Xiong, I. Washio, J.Y. Chen, H.G. Cai, Z.Y. Li, Y.N. Xia, Poly(vinyl pyrrolidone): A dual functional reductant and stabilizer for the facile synthesis of noble metal nanoplates in aqueous solutions, Langmuir, 22 (2006) 8563-8570.
[33] G.B. Khomutov, Interfacially formed organized planar inorganic, polymeric and composite nanostructures, Advances in Colloid and Interface Science, 111 (2004) 79-116.
[34] D.C. Pan, Q. Wang, L.J. An, Controlled synthesis of monodisperse nanocrystals by a two-phase approach without the separation of nucleation and growth processes, Journal of Materials Chemistry, 19 (2009) 1063-1073.

[35] E. Hammarberg, C. Feldmann, In^0 nanoparticle synthesis assisted by phase-transfer reaction, Chemistry of Materials, 21 (2009) 771.

[36] A. Badia, S. Singh, L. Demers, L. Cuccia, G.R. Brown, R.B. Lennox, Self-assembled monolayers on gold nanoparticles, Chemistry-a European Journal, 2 (1996) 359-363.

[37] Y.H. Jang, S.T. Kochuveedu, M.A. Cha, Y.J. Jang, J.Y. Lee, J. Lee, J. Kim, D.Y. Ryu, D.H. Kim, Synthesis and photocatalytic properties of hierarchical metal nanoparticles/ZnO thin films hetero nanostructures assisted by diblock copolymer inverse micellar nanotemplates, Journal of Colloid and Interface Science, 345 (2010) 125-130.

[38] T. Krasia, H. Schlaad, Poly 2-(acetoacetoxy)ethyl methacrylate -based hybrid micelles, in: U.S. Schubert, G.R. Newkome, I. Manners (Eds.) Metal-Containing and Metallosupramolecular Polymers and Materials, 2006, pp. 157-167.

[39] Y.H. Jang, S.T. Kochuveedu, Y.J. Jang, H.Y. Shin, S. Yoon, M. Steinhart, D.H. Kim, The fabrication of graphitic thin films with highly dispersed noble metal nanoparticles by direct carbonization of block copolymer inverse micelle templates, Carbon, 49 (2011) 2120-2126.

[40] M. Haruta, T. Kobayashi, H. Sano, N. Yamada, Nobel gold catalysis for the oxidation of carbon-monoxide at a temperature far below 0-degrees C, Chemistry Letters, (1987) 405-408.

[41] R. Zanella, S. Giorgio, C.H. Shin, C.R. Henry, C. Louis, Characterization and reactivity in CO oxidation of gold nanoparticles supported on TiO_2 prepared by deposition-precipitation with NaOH and urea, Journal of Catalysis, 222 (2004) 357-367.

[42] H.L. Jiang, B. Liu, T. Akita, M. Haruta, H. Sakurai, Q. Xu, $Au^{@}$ZIF-8: CO oxidation over gold nanoparticles deposited to metal-organic framework, Journal of the American Chemical Society, 131 (2009) 11302-11303.

[43] M. Haruta, M. Date, Advances in the catalysis of Au nanoparticles, Applied Catalysis a-General, 222 (2001) 427-437.

[44] M. Haruta, Catalysis of gold nanoparticles deposited on metal oxides, Cattech, 6 (2002) 102-115.

[45] M. Okumura, S. Nakamura, S. Tsubota, T. Nakamura, M. Azuma, M. Haruta, Chemical vapor deposition of gold on Al_2O_3, SiO_2, and TiO_2 for the oxidation of CO and of H_2, Catalysis Letters, 51 (1998) 53-58.

[46] M. Date, M. Okumura, S. Tsubota, M. Haruta, Vital role of moisture in the catalytic activity of supported gold nanoparticles, Angewandte Chemie-International Edition, 43 (2004) 2129-2132.

[47] F. Maillard, S. Schreier, M. Hanzlik, E.R. Savinova, S. Weinkauf, U. Stimming, Influence of particle agglomeration on the catalytic activity of carbon-supported Pt nanoparticles in CO monolayer oxidation, Physical Chemistry Chemical Physics, 7 (2005) 385-393.

[48] A. Fukuoka, J.I. Kimura, T. Oshio, Y. Sakamoto, M. Ichikawa, Preferential oxidation of carbon monoxide catalyzed by platinum nanoparticles in mesoporous silica, Journal of the American Chemical Society, 129 (2007) 10120-10125.

[49] T. Visser, T.A. Nijhuis, A.M.J. van der Eerden, K. Jenken, Y.Y. Ji, W. Bras, S. Nikitenko, Y. Ikeda, M. Lepage, B.M. Weckhuysen, Promotion effects in the oxidation of CO over zeolite-supported Pt nanoparticles, Journal of Physical Chemistry B, 109 (2005) 3822-3831.

[50] M.S. Jin, H.Y. Liu, H. Zhang, Z.X. Xie, J.Y. Liu, Y.N. Xia, Synthesis of Pd nanocrystals enclosed by {100} facets and with sizes < 10 nm for application in CO oxidation, Nano Research, 4 (2011) 83-91.

[51] J.D. Grunwaldt, C. Kiener, C. Wogerbauer, A. Baiker, Preparation of supported gold catalysts for low-temperature CO oxidation via "size-controlled" gold colloids, Journal of Catalysis, 181 (1999) 223-232.

[52] O. Carp, C.L. Huisman, A. Reller, Photoinduced reactivity of titanium dioxide, Progress in Solid State Chemistry, 32 (2004) 33-177.

[53] M. Pera-Titus, V. Garcia-Molina, M.A. Banos, J. Gimenez, S. Esplugas, Degradation of chlorophenols by means of advanced oxidation processes: a general review, Applied Catalysis B-Environmental, 47 (2004) 219-256.

[54] P.R. Gogate, A.B. Pandit, A review of imperative technologies for wastewater treatment I: oxidation technologies at ambient conditions, Advances in Environmental Research, 8 (2004) 501-551.

[55] S. Sakthivel, B. Neppolian, M.V. Shankar, B. Arabindoo, M. Palanichamy, V. Murugesan, Solar photocatalytic degradation of azo dye: comparison of photocatalytic efficiency of ZnO and TiO_2, Solar Energy Materials and Solar Cells, 77 (2003) 65-82.

[56] C.A. Martinez-Huitle, E. Brillas, Decontamination of wastewaters containing synthetic organic dyes by electrochemical methods: A general review, Applied Catalysis B-Environmental, 87 (2009) 105-145.

[57] G. Palmisano, M. Addamo, V. Augugliaro, T. Caronna, A. Di Paola, E.G. Lopez, V. Loddo, G. Marci, L. Palmisano, M. Schiavello, Selectivity of hydroxyl radical in the partial oxidation of aromatic compounds in heterogeneous photocatalysis, Catalysis Today, 122 (2007) 118-127.

[58] V. Iliev, D. Tomova, L. Bilyarska, A. Eliyas, L. Petrov, Photocatalytic properties of TiO_2 modified with platinum and silver nanoparticles in the degradation of oxalic acid in aqueous solution, Applied Catalysis B-Environmental, 63 (2006) 266-271.

[59] V. Iliev, D. Tomova, L. Bilyarska, G. Tyuliev, Influence of the size of gold nanoparticles deposited on TiO_2 upon the photocatalytic destruction of oxalic acid, Journal of Molecular Catalysis a-Chemical, 263 (2007) 32-38.

[60] G.M. Zuo, Z.X. Cheng, H. Chen, G.W. Li, T. Miao, Study on photocatalytic degradation of several volatile organic compounds, Journal of Hazardous Materials, 128 (2006) 158-163.

[61] C. Hu, Y.H. Tang, Z. Jiang, Z.P. Hao, H.X. Tang, P.K. Wong, Characterization and photocatalytic activity of noble-metal-supported surface TiO_2/SiO_2, Applied Catalysis a-General, 253 (2003) 389-396.

[62] J.Y. Zheng, H. Yu, X.J. Li, S.Q. Zhang, Enhanced photocatalytic activity of TiO_2 nano-structured thin film with a silver hierarchical configuration, Applied Surface Science, 254 (2008) 1630-1635.

[63] F.B. Li, X.Z. Li, The enhancement of photodegradation efficiency using Pt-TiO_2 catalyst, Chemosphere, 48 (2002) 1103-1111.

[64] X.Z. Li, F.B. Li, Study of Au/Au^{3+}-TiO2 photocatalysts toward visible photooxidation for water and wastewater treatment, Environmental Science & Technology, 35 (2001) 2381-2387.

[65] J.W. Liu, Y. Sun, Z.H. Li, S.Y. Li, J.X. Zhao, Photocatalytic hydrogen production from water/methanol solutions over highly ordered Ag-$SrTiO_3$ nanotube arrays, International Journal of Hydrogen Energy, 36 (2011) 5811-5816.

[66] V. Subramanian, E. Wolf, P.V. Kamat, Semiconductor-metal composite nanostructures. To what extent do metal nanoparticles improve the photocatalytic activity of TiO_2 films?, Journal of Physical Chemistry B, 105 (2001) 11439-11446.

[67] Y. Miseki, H. Kato, A. Kudo, Water splitting into H_2 and O_2 over niobate and titanate photocatalysts with (111) plane-type layered perovskite structure, Energy & Environmental Science, 2 (2009) 306-314.
[68] N. Lopez, T.V.W. Janssens, B.S. Clausen, Y. Xu, M. Mavrikakis, T. Bligaard, J.K. Norskov, On the origin of the catalytic activity of gold nanoparticles for low-temperature CO oxidation, Journal of Catalysis, 223 (2004) 232-235.
[69] M. Valden, X. Lai, D.W. Goodman, Onset of catalytic activity of gold clusters on titania with the appearance of nonmetallic properties, Science, 281 (1998) 1647-1650.
[70] M. Valden, S. Pak, X. Lai, D.W. Goodman, Structure sensitivity of CO oxidation over model Au/TiO_2 catalysts, Catalysis Letters, 56 (1998) 7-10.
[71] V. Aguilar-Guerrero, B.C. Gates, Genesis of a highly active cerium oxide-supported gold catalyst for CO oxidation, Chemical Communications, (2007) 3210-3212.
[72] L.C. Wang, X.S. Huang, Q. Liu, Y.M. Liu, Y. Cao, H.Y. He, K.N. Fan, J.H. Zhuang, Gold nanoparticles deposited on manganese(III) oxide as novel efficient catalyst for low temperature CO oxidation, Journal of Catalysis, 259 (2008) 66-74.
[73] N.F.P. Ribeiro, F.M.T. Mendes, C.A.C. Perez, M. Souza, M. Schmal, Selective CO oxidation with nano gold particles-based catalysts over Al_2O_3 and ZrO_2, Applied Catalysis a-General, 347 (2008) 62-71.
[74] K.L. Kelly, E. Coronado, L.L. Zhao, G.C. Schatz, The optical properties of metal nanoparticles: The influence of size, shape, and dielectric environment, Journal of Physical Chemistry B, 107 (2003) 668-677.
[75] N. Tian, Z.Y. Zhou, S.G. Sun, Y. Ding, Z.L. Wang, Synthesis of tetrahexahedral platinum nanocrystals with high-index facets and high electro-oxidation activity, Science, 316 (2007) 732-735.
[76] J. Park, J. Joo, S.G. Kwon, Y. Jang, T. Hyeon, Synthesis of monodisperse spherical nanocrystals, Angewandte Chemie-International Edition, 46 (2007) 4630-4660.
[77] S. Eustis, M.A. El-Sayed, Why gold nanoparticles are more precious than pretty gold: Noble metal surface plasmon resonance and its enhancement of the radiative and nonradiative properties of nanocrystals of different shapes, Chemical Society Reviews, 35 (2006) 209-217.
[78] T.K. Sau, A.L. Rogach, Nonspherical noble metal nanoparticles: colloid-chemical synthesis and morphology control, Advanced Materials, 22 (2010) 1781-1804.

[79] G.J. Nusz, A.C. Curry, S.M. Marinakos, A. Wax, A. Chilkoti, Rational selection of gold nanorod geometry for label-free plasmonic biosensors, Acs Nano, 3 (2009) 795-806.

[80] P.D. Cozzoli, M.L. Curri, A. Agostiano, Efficient charge storage in photoexcited TiO_2 nanorod-noble metal nanoparticle composite systems, Chemical Communications, (2005) 3186-3188.

[81] P.R. Evans, G.A. Wurtz, R. Atkinson, W. Hendren, D. O'Connor, W. Dickson, R.J. Pollard, A.V. Zayats, Plasmonic Core/Shell nanorod arrays: Subattoliter controlled geometry and tunable optical properties, Journal of Physical Chemistry C, 111 (2007) 12522-12527.

[82] H. Baida, D. Mongin, D. Christofilos, G. Bachelier, A. Crut, P. Maioli, N. Del Fatti, F. Vallee, Ultrafast nonlinear optical response of a single gold nanorod near its surface plasmon resonance, Physical Review Letters, 107 (2011) 057402.

[83] M.A. El-Sayed, Some interesting properties of metals confined in time and nanometer space of different shapes, Accounts of Chemical Research, 34 (2001) 257-264.

[84] R.C. Jin, Y.C. Cao, E.C. Hao, G.S. Metraux, G.C. Schatz, C.A. Mirkin, Controlling anisotropic nanoparticle growth through plasmon excitation, Nature, 425 (2003) 487-490.

[85] F. Kim, S. Connor, H. Song, T. Kuykendall, P.D. Yang, Platonic gold nanocrystals, Angewandte Chemie-International Edition, 43 (2004) 3673-3677.

[86] D. Takagi, Y. Homma, H. Hibino, S. Suzuki, Y. Kobayashi, Single-walled carbon nanotube growth from highly activated metal nanoparticles, Nano Letters, 6 (2006) 2642-2645.

[87] R.C. Jin, Y.W. Cao, C.A. Mirkin, K.L. Kelly, G.C. Schatz, J.G. Zheng, Photoinduced conversion of silver nanospheres to nanoprisms, Science, 294 (2001) 1901-1903.

[88] M.P. Pileni, The role of soft colloidal templates in controlling the size and shape of inorganic nanocrystals, Nature Materials, 2 (2003) 145-150.

Chapter 5

Characterization, Experimental and Computational Methods

5.1 Characterization methods

The following sections describe several important characterization techniques used throughout the following chapters. These techniques help to determine several materials' properties, such as how a material interacts with light, as well as their chemical and physical properties. These techniques are important for predicting, analyzing and interpretation of the observed photocatalytic activity.

5.1.1 UV-Vis spectroscopy

The performance of a photocatalyst in large part dependents on the material's optical properties, such as light absorbance. These properties indicate how a material interacts with photon flux; for example, the absorbance of a semiconductor is a direct measurement of the fraction of incident photons that produce charge carriers (electron/hole pairs). Spectroscopy in general refers to a technique for measuring the interaction of a material with energy. Since the studies presented in this dissertation use UV and visible light sources, the most useful characterization technique is UV-visible spectroscopy.

To explain the quantities that are measured, several terms need to be defined. For example, absorbance is a measurement of the fraction of photons that interact with the material to produce excited charge carriers (electron-hole pairs). The charge carriers eventually release the stored energy through some non-radiative process such as heating through excitation of phonon modes or through transferring charge to the surroundings [1, 2]. This process is referred to as absorption and the measured quantity is the absorbance. Absorbance is usually defined in the field of analytical chemistry as the logarithm (base 10) of I_0/I, where I_0 is intensity of the incident light and I is the intensity of light transmitted through the sample to the detector. The quantity I_0/I is the reciprocal of transmittance, T (the amount of light not absorbed) [3].

The scattering process is simply the interaction of a photon with a material, in which the net result is that the photon changes direction. This can be due to a few effects, such as the interaction of light with a structure similar in size to the light wavelength. It can also be due to temporary excitation of electronic states or virtual states within a material, which then relax by re-emitting a photon. This process is referred to as Rayleigh scattering if the emitted photon has the same energy as the incident photon, Stokes scattering if the emitted photon has less energy than the incident photon or anti-Stoke scattering if the emitted photon has gained energy [4-6]. The emitted photons (the vast majority of which are Rayleigh scattered) are emitted in essentially

random directions, sometimes called diffuse scattering or diffuse reflection [7]. Because of this, if a sample scatters a high portion of the incident light, then very little signal will reach the detector of the spectrometer. To get around this problem we must use a special version of UV-visible spectroscopy, referred to as diffuse reflectance UV-Visible spectroscopy (DRUVS), which is discussed below.

Extinction: The total amount of the incident light in a spectrometer that does not reach the detector (i.e., the extinguished light) is called the extinction. Essentially, this amounts to the sum of the absorbance and scattering discussed above. As mentioned above, transmittance through a sample is defined as I_0/I, or the fraction of light that reaches detector. In fact, when we measure an "absorbance spectrum" in a spectrometer, we are actually measuring the extinction from the sample, and as mentioned above we must be careful if trying to specifically assign this extinction to absorbance or scattering, since both effects could be present [8, 9].

All of the spectra measured throughout this document were carried out using a Thermo Scientific Evolution 3000 UV-visible Spectrometer. As mentioned above, the machine nominally measures absorbance and transmittance. For solid samples, we have used diffuse reflectance spectroscopy. Measurements were obtained using a Thermo Mantis diffuse reflectance cell within the UV-visible spectrometer listed above. The measurement is essentially the same, except that the beam is not passed through the sample, rather the sample is illuminated at an angle. Light is scattered in all directions and a parabolic mirror captures a relatively large portion of the light and focuses it back to the detector. The absorbance characteristics of the materials thus can be measured.

5.1.2 X-ray powder diffraction (XRD)

XRD is a rapid analytical technique primarily used for phase identification of a crystalline material and can provide information on unit cell dimensions. The analyzed material is finely ground, homogenized, and average bulk composition is determined. X-ray diffraction is based on constructive interference of monochromatic X-rays and a crystalline sample. X-rays are generated by a cathode ray tube, filtered to produce monochromatic radiation, collimated to concentrate, and directed toward the sample. The interaction of the incident rays with the sample produces constructive interference (and a diffracted ray) when conditions satisfy Bragg's Law [10]:

$$n\lambda = 2d \sin \theta \qquad (5\text{-}1)$$

In this equation, λ is the wavelength of the incident X- ray, θ is the Bragg angle which defines the angle between the incident X-ray beam and the scattering planes.

This law relates the wavelength of electromagnetic radiation to the diffraction angle and the lattice spacing in a crystalline sample. These diffracted X-rays are then detected, processed and counted. By scanning the sample through a range of 2θ angles, all possible diffraction directions of the lattice should be attained due to the random orientation of the powdered material. Conversion of the diffraction peaks to d-spacings allows identification of the mineral because each mineral has a set of unique d-spacings. Typically, this is achieved by comparison of d-spacings with standard reference patterns. The crystallite size of the materials were calculated using the Scherrer equation which is given by [11]:

$$\tau = \frac{K\lambda}{B\cos\theta} \tag{5-2}$$

In this equation, τ is the mean size of the crystalline domains. τ can be smaller or equal to the grain size. K is the shape factor. A typical value of K is about 0.9, however, it can vary with the actual shape of the crystallite, B is the line broadening at half the maximum intensity. The disadvantages of XRD is that it only provides analysis of bulk crystalline phases and is unable to provide surface information, detect amorphous phases or detect crystalline particles smaller than 3 nm due to peak broadening. Thus, XRD is only a good tool to provide bulk structural information about large particles (> 3 nm).

In this study, two XRD instruments (Rigaku Ultima IV diffractometer with CuKα radiation and a position sensitive detector, Bruker X-ray diffraction D8-discover) were used. Rigaku Ultima IV diffractometer provided full and precise scanning of the developed materials. Bruker X-ray diffraction D8-discover provided a quick scan option for early stage investigations and sample filtering.

5.1.3 Electron Microscopy

Electron microscopy offers an effective way to understand the surface, interface and chemical characteristics of a photocatalyst system. Electron microscopy encompasses many different techniques such as Transmission Electron Microscopy (TEM), Scanning Electron Microscopy (SEM), Scanning Transmission Electron Microscopy (STEM), Energy-Dispersive

X-ray Spectroscopy (EDX), and Electron Energy-Loss Spectroscopy (EELS). These techniques provide different angles to characterize materials. Among them, TEM is the most commonly used technique for studying photocatalytic materials which is primarily used to give information on topography, morphology and crystal structure at with atomic resolution (0.1 nm) [12] and bulk composition when coupled with EELS. SEM is carried out by rastering a narrow electron beam over the sample's surface and collect the information from secondary electron and back scattered electrons. The main difference between SEM and TEM is that SEM observes contrast due to topology and composition of a surface, and the TEM aims at the projection information from the materials [13].

All the TEM images present in this dissertation were obtained through JOEL JEM 2100F microscope using 10-20 kV accelerating voltage. STEM images were obtained through Hitachi HD2700C with a probe aberration corrector.

5.1.4 X-ray photoelectron spectroscopy (XPS)

XPS is a surface technique that utilizes photons from an X-ray source to excite the electronic states of atoms near the surface (~1-3 nm) of a solid [14]. The electrons ejected from the sample are collected by a hemispherical electron energy analyzer which measures the kinetic energy of the ejected electrons. The kinetic energy measured can then be used to determine the binding energy of the electron from the following equation [15]:

$$E_{bingding} = E_{phonton} - (E_{kinetic} + \phi) \quad (5\text{-}3)$$

where $E_{binding}$ is the binding energy (BE) of the electron, $E_{phonton}$ is the energy of the X-ray photons, $E_{kinetic}$ is the kinetic energy of the electron which is measured by the instrument and ϕ is the work function of the spectrometer (not the material). Each ejected electron from an element has a characteristic binding energy and the position of this binding energy is used to identify the element and core level of the electron that can be found by consulting binding energy tables. The peak intensities can be used to quantitatively determine the elemental composition (detection limit ~ 1000 ppm for most elements) and the peak positions can be used to determine oxidation states for the elements. In general, binding energies increases with increasing oxidation state typically shifting by about 0-3 eV [14]. Some of the disadvantages of XPS are that it requires ultra-high vacuum conditions, sample damage from the X-ray sources, not sensitive

enough to get information on only the outermost layer (~0.3 nm) and overlapping elemental peaks that can make spectra analysis challenging.

5.1.5 Gas Chromatography

Gas chromatography (GC) is a common type of chromatography used in analytic chemistry for separating and analyzing compounds that can be vaporized without decomposition [16, 17]. In gas chromatography, the moving phase (or "mobile phase") is a carrier gas, usually an inert gas such as helium or an unreactive gas such as nitrogen [18]. The stationary phase is a microscopic layer of a polymer deposited on an inert solid support, which is placed inside a piece of glass or metal tubing called a column (an homage to the fractionating column used in distillation) [19]. The instrument used to perform gas chromatography is called a gas chromatograph. The gaseous compounds being analyzed interact with the walls of the column, which is coated with different stationary phases. This causes each compound to elute at a different time, known as the retention time of the compound. The comparison of retention times is what gives GC its analytical usefulness.

All the gas chromatographs in this dissertation were obtained through Agilent 7890A Gas Chromatography equipped with HP-PLOT Molesieve 5A as the column and a Thermal Conductivity Detector (TCD) as the detector. All the chromatographs were subjected to software (MSD Chemstation) for quantitative calculation and data analysis.

5.2 Photocatalytic experimental setup

5.2.1 Light source

Photocatalytic activity evaluation of the developed photocatalysts was mostly performed under visible light. However, in order to investigate the photocatalytic activity of unmodified photocatalysts, Ultra-visible light was also employed. The light used in the experiments was generated using a solar simulator (Model: 66983, Newport, with a 300 W Xe arc lamp and an AM 1.5 filter). The lamp delivers a smooth continuum through the UV-Vis and some high intensity lines in the NIR. Figure 5-1 shows the irradiance intensity of the lamp in this dissertation, it produces a total irradiance about 100 mW cm^{-2} at full power.

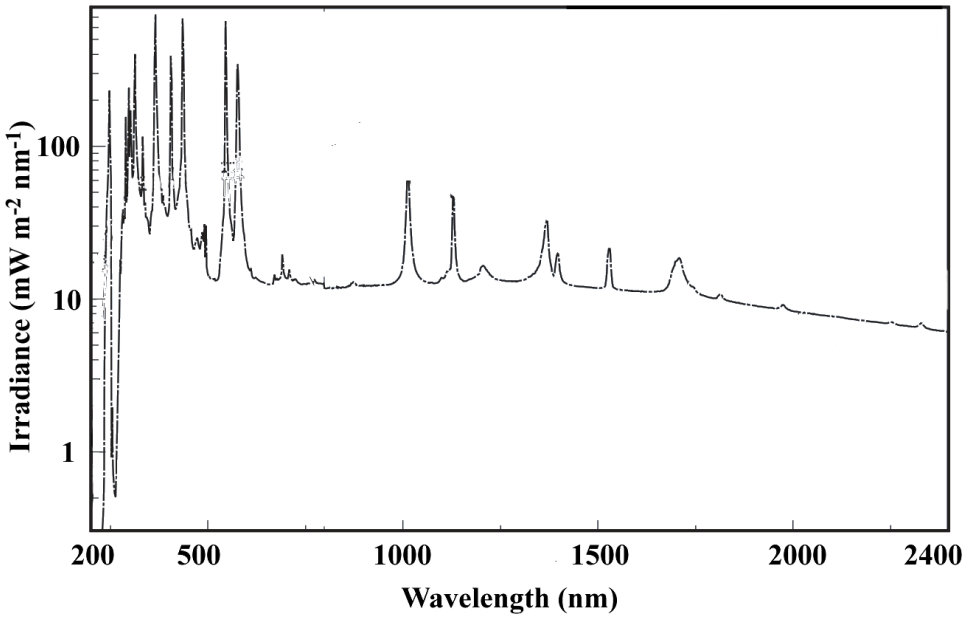

Figure 5-1 Irradiance intensity of the lamp used in this dissertation

5.2.2 Light filters

The light produced by the light source is filtered by different optical filters to obtain light in a particular range of wavelengths. The optical filters used in this study were all long pass filters (320 nm, Edmund optics; 400 nm, Hoya; 420 nm, Hoya). A long pass filter is an optical interference or colored glass filter that attenuates shorter wavelengths and transmits longer wavelengths over the active range of the target spectrum. Figure 5-2 and 5-3 show the Absorbance spectrum of 320 nm and 420 nm optical filters in wavelength between 200-800 nm.

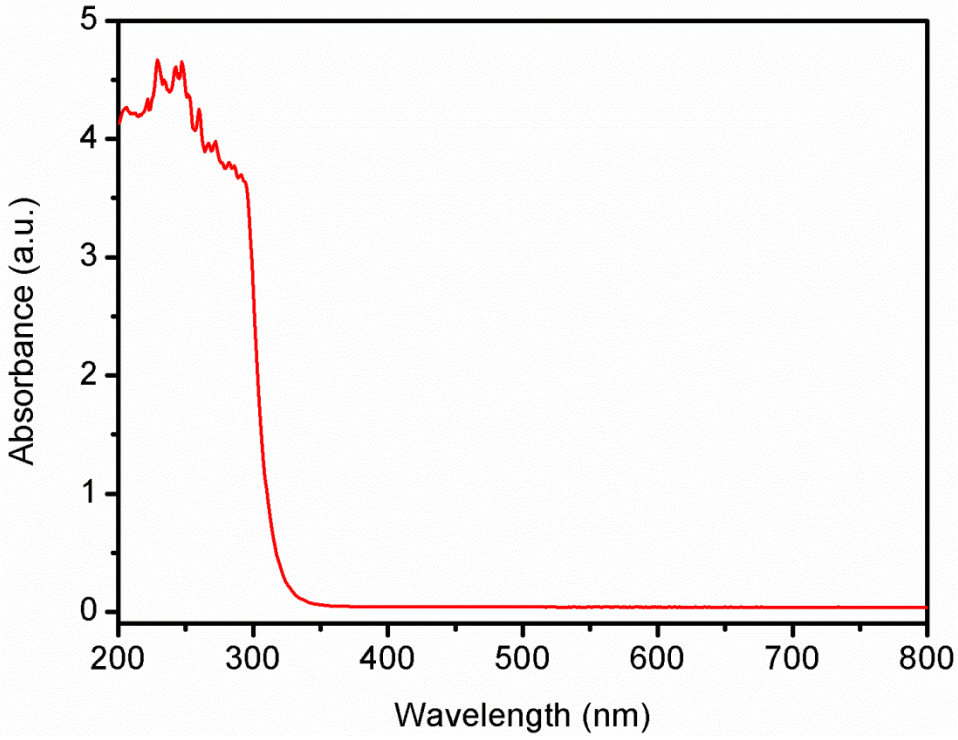

Figure 5-2 Absorbance spectrum of 320 nm optical filter. The absorbance of this optical filter ≤ 10 % of the total intensity with light wavelength ≥ 320 nm.

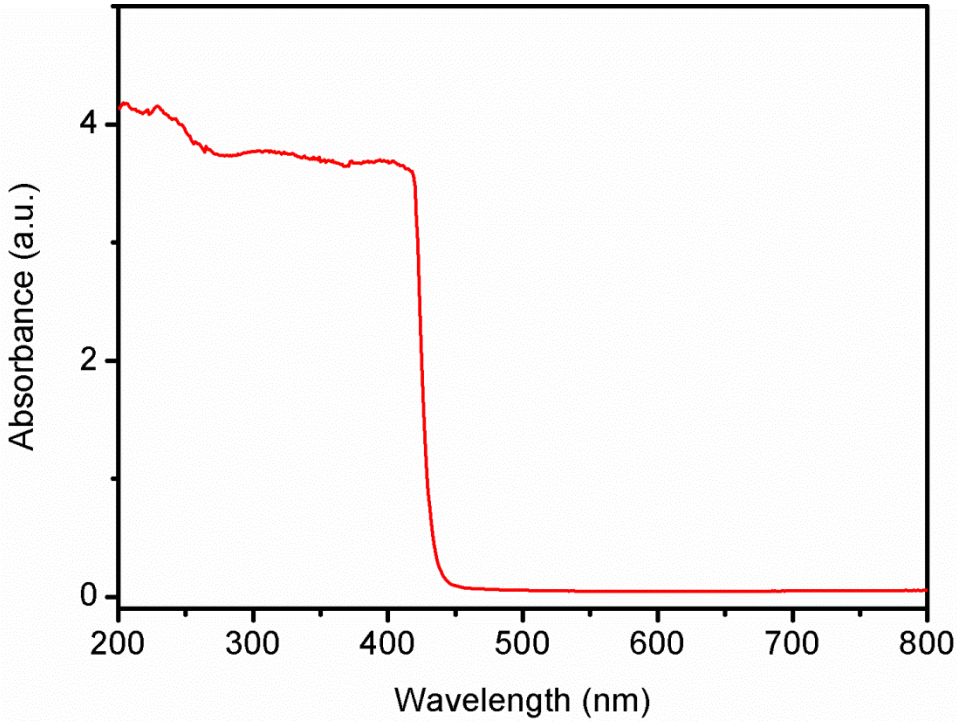

Figure 5-3 Absorbance spectrum of 420 nm optical filter. The absorbance of this optical filter ≤ 10 % of the total intensity with light wavelength ≥ 420 nm.

5.2.3 Reactor

An ideal reactor for photocatalytic water splitting and hydrogen evolution should meet several criteria:

(1) The reactor should be gas tight. It should hold vacuum as well as positive pressure up to 1 bar. Ideally, the leakage rate should be lower than $1x10^{-7}$ mbar L/sec to minimize the influence from the leakage.

(2) Light from the light source can pass through the container and interact with the reactants. However, unnecessary light from the interference should be eliminated.

(3) Easy operation and cleaning. The reactor should be able to be cleaned to remove any chemical residues after each photocatalytic reaction.

(4) Availability of passive cooling capability to maintain a constant temperature during the photocatalytic reactions.

(5) Chemically inert when in contact with various photocatalysts and reactants, and mechanically stable and durable.

Unfortunately, there is no commercial available reactor which meets all the requirements. To better evaluate the photocatalytic activity, a reactor with all the features mentioned above, was designed and developed. Figure 5-4 shows a schematic diagram of the designed reactor.

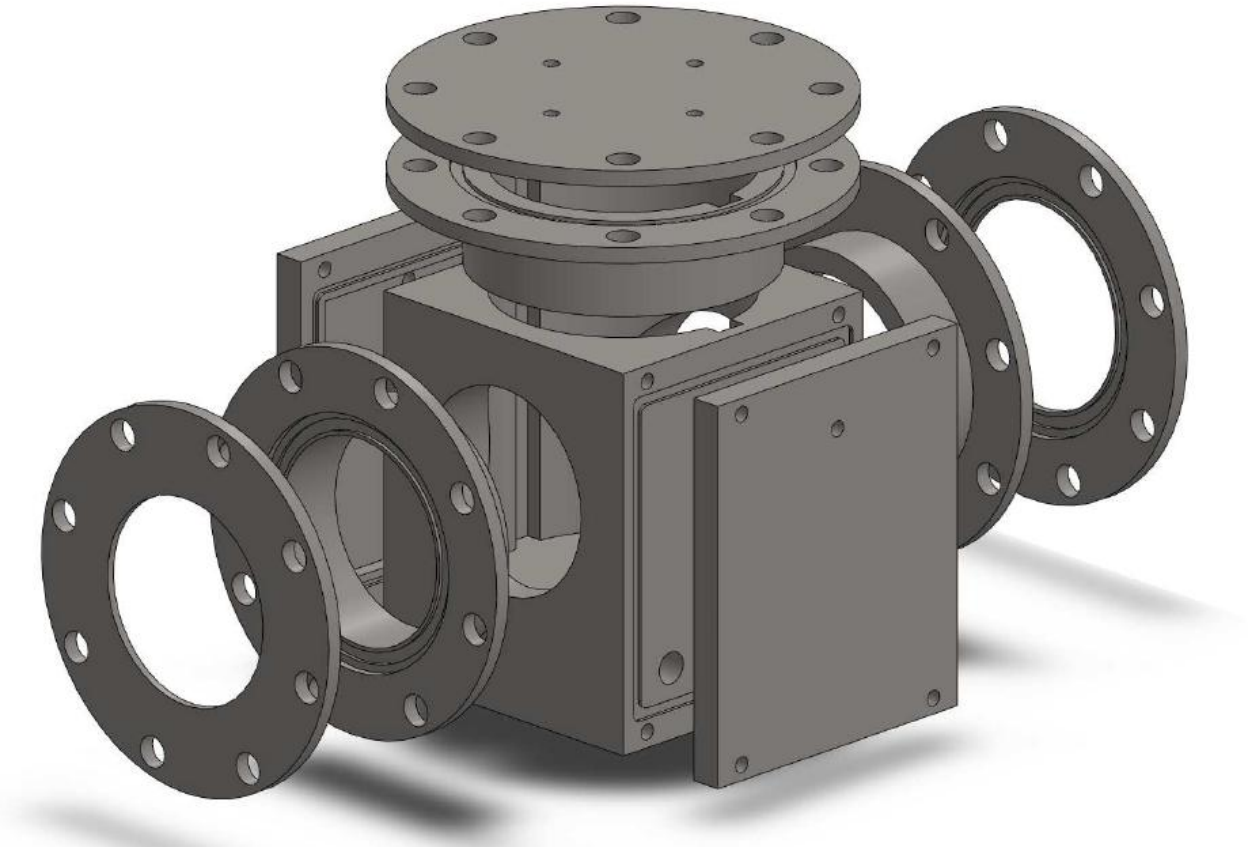

Figure 5-4 Schematic diagram of the designed reactor for photocatalytic reactions.

The reactor was made of stainless steels and has a dead volume of 190 ml. It uses flange designs for superior gas tightness as these designs can be seen on a lot of ultra high vacuum chambers. Two pieces of quartz glass were equipped in the reactor to serve as windows to maximize the luminous intensity from the light source. To be noted, the diameter of the quartz window matches the diameter of the light from the light source for full light flux utilization. It also provides the flexibility in terms of light irradiation directions.

The designed reactor is equipped with two side pockets which serve as water cooling jackets. As the light source emits a lot of heat, without water cooling, the temperature of the reactant in the reactor tends to go up and the chemical kinetics of the reaction can be largely affected. However, our reactor was tested and proved to maintain constant temperatures during the reaction. Figure 5-5 presents the photograph of the developed reactor.

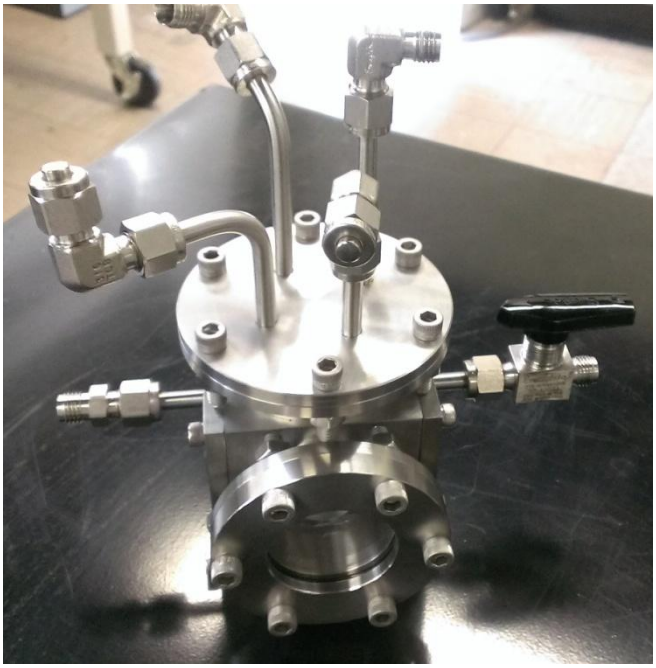

Figure 5-5 Photograph of the designed reactor.

Furthermore, two slots was designed and developed to expend its applications (Figure 5-6). As various accessories can be inserted into the reactor along the two slots, the reactor will be able to serve as an ideal reactor for other related projects in the future.

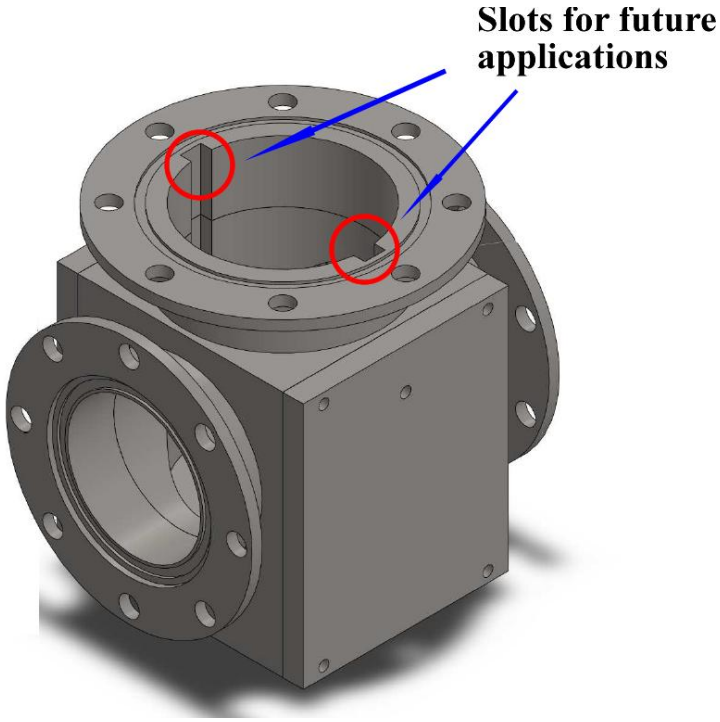

Figure 5-6 Schematic diagram shows the designed reactor has two slots for expandability.

5.2.4 Apparatus for photocatalytic activity evaluation

Figure 5-7 shows the schematic diagram and actual photograph of the photocatalytic activity reaction apparatus, respectively.

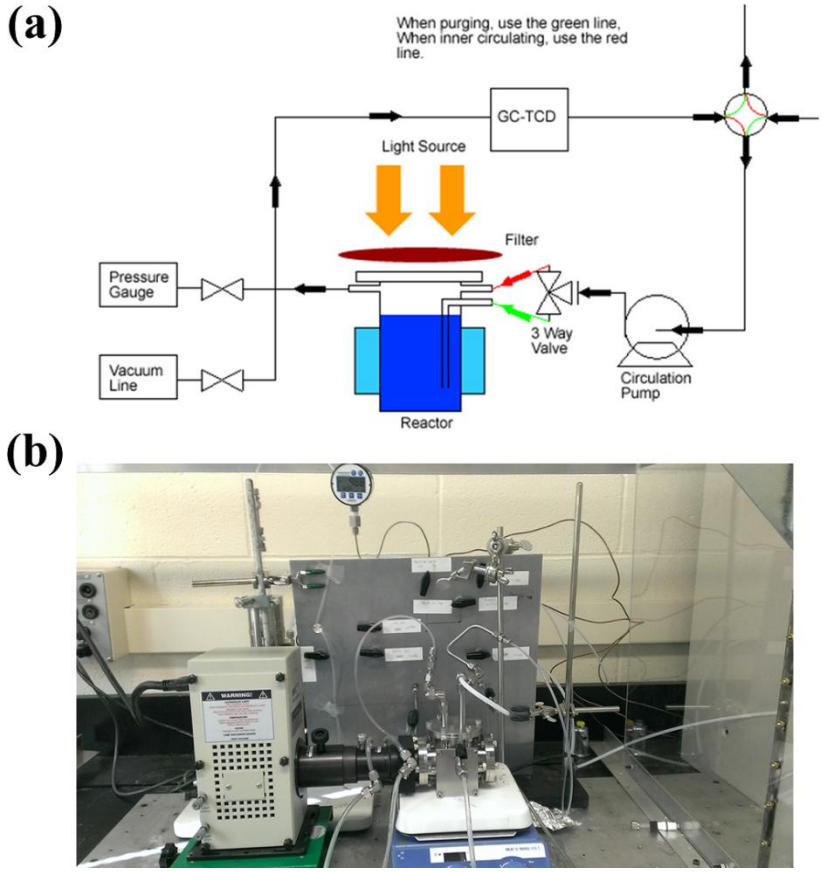

Figure 5-7 Schematic diagram (a) and photograph (b) of the photocatalytic activity reaction apparatus.

Various components, including reactor, pressure gauge, gas circulation pump, vacuum pump and on-line analysis instrument (GC-TCD) were connected through 1/8" 316 stainless steel tubings. The pressure gauge was used to monitor the pressure inside the apparatus. The gas circulation pump was used to ensure good gas circulation and delivery. The apparatus was optimized in design of piping and gas circulation. The apparatus underwent strict tightness examination to minimize the leakage. Given leakage can be detrimental for photocatalytic activity testing for water splitting and hydrogen evolution and therefore we have made every effort to minimize O_2 diffusion from the atmosphere. The measured leakage rate was less than $1x10^{-7}$ mbar L/sec for the apparatus using in this research.

5.3 Method of photocatalytic reaction

Photocatalytic reactions were carried out in the reactors demonstrated above. The photocatalyst powder was suspended in 50 or 100 ml di-ionized water or di-ionized water with sacrificial reagent. The system was degassed by a vacuum pump, and ultra pure argon (Ar, 99.99%) was subsequently introduced into the apparatus for purging. This procedure was repeated 3 times to ensure O_2 free environment in the apparatus. The suspension was stirred by a magnetic stirrer and irradiated by the light source equipped with an optical filter. The evolved gas was circulated and delivered to an on-line GC-TCD (Agilent 7890A) by a gas circulator for gas components analysis.

5.4 Parameters for photocatalytic activity evaluation

To properly evaluate photocatalytic water splitting and/or photocatalytic hydrogen evolution, several points should be highlighted:

5.4.1 Time dependence

Time course provides the detailed photocatalytic activity information of the photocatalyst. Amounts of H_2 and O_2 evolved for water splitting, or, for photocatalytic hydrogen evolution case, amount of H_2 evolved should increase with irradiation time. To check not only the value of activity or a gas evolution rate but also the time course is important. Time course reveals the stability of the photocatalyst, for example, a linear line of hydrogen evolution versus time normally demonstrates better stability. Time course also enables research of back reaction during the photocatalytic processes. Long term reactions (more than 48 hours) and repeated cycles reactions are always performed to show the time course of the photocatalytic reactions.

5.4.2 Induction period

For some photocatalytic reactions, the photocatalysts showed low activities (or sometimes no activity) at beginning of the reactions. This is known as induction period. Induction period provides a way in fundamental interpretation of the photocatalysts, more specifically, the chemical kinetics of the photocatalysts. Chemical and electronic structure changes can greatly affect the chemical kinetics, which, eventually, result in induction periods [20]. Previous research of induction periods in photocatalytic processes include [21-23]. These studies provided a lot of insights of induction periods understanding and proved induction period cannot be neglected.

5.4.3 Turnover number (TON)

In catalysis, TON is defined as the maximum amount of the products which are catalyzed before a catalyst becoming inactivated. An ideal catalyst would have an infinite TON, however, to be realistic, infinite TON is not achievable. In photocatalytic water splitting and hydrogen evolution, TON is an important parameter as it evaluates the stability of a photocatalyst. The total molar amount of the evolved hydrogen and oxygen should overwhelm the molar amount of the photocatalyst used to prove the reaction proceeds photocatalytically. The following equation is used to define TON:

$$\mathrm{TON} = \frac{\text{Number of reacted molecules}}{\text{Number of active sites}} \tag{5-4}$$

However, to determine the number of active sites for photocatalysts is challenging. Therefore, the number of reacted electrons to the number of atoms in a photocatalyst or on the surface of a photocatalyst is employed as the TON, as shown in Equation 5-5.

$$\mathrm{TON} = \frac{\text{Number of reacted electrons}}{\text{Number of atoms in a photocatalyst}} \tag{5-5}$$

In this equation, the number of reacted electrons is calculated from the amount of evolved H_2. The number of atoms in a photocatalyst can be calculated according to the total mass and molar weight of the photocatalyst. Since only atoms on the surface of a photocatalyst can be active sites, the TON calculated from equation 5.5 is usually smaller than that of the real case.

For this reason, normalization of photocatalytic activity by weight of used photocatalyst (for example, mmol $h^{-1}g^{-1}$) is not a proper way because the photocatalytic activity is not usually proportional to the weight of photocatalyst, as the inactive atoms cannot make contribution to the photocatalytic activity. The rate of gas evolution should indicate without the mass of the photocatalyst, for example, mmol h^{-1} should be used to evaluate the photocatalytic activity.

5.4.4 Quantum efficiency (QE)

Photocatalytic activity largely depends on the experimental conditions such as a light source and a type of a reaction cell. The activity of a photocatalyst is not comparable if two different experimental systems are employed. To evaluate the activity of a photocatalyst, even with

different experimental systems, testing the QE of a photocatalyst is important. QE can be measure through the follow equation:

$$\text{QE}\ (\%) = \frac{\text{Number of reacted ectrons}}{\text{Number of incident photons}} \times 100 \qquad (5\text{-}6)$$

In this equation, the number of incident photons can be measured using a thermopile or Si photodiode. The number of reacted electrons can be calculated from the evolved hydrogen and oxygen.

It should be noteworthy that the quantum efficiency measured here is different from solar energy conversion, which presents in the following equation:

$$\text{Solar energy conversion}\ (\%) = \frac{\text{Output energy as } H_2}{\text{Energy of incident solar light}} \times 100 \qquad (5\text{-}7)$$

The number of photocatalysts that can give good solar energy conversion efficiency is limited at the present stage because of insufficient activities for the measurement. However, the solar energy conversion efficiency should finally be used to evaluate the photocatalytic water splitting if solar hydrogen production is considered.

5.5 Computational method

Some results in the following chapters depend on optical simulations. Two computational methods are used for simulation of metal nanoparticles structures and charges: Density functional theory and Time Dependent Density Functional Theory. These two computational methods are briefly introduced here.

5.5.1 Density functional theory (DFT)

DFT is a widely used quantum mechanical modeling method for electronic structure investigation (principally the ground state) of many-body systems including atoms, molecules and the condensed phases. In DFT calculation, the electron density is used to determine the properties of a many-electron system. DFT is among the most popular methods in various disciplines, such as computational physics and computational chemistry. It provides an effective tool for calculations in solid state physics. However, while DFT has a lot of advantages, it also suffers from several drawbacks. For example, first, DFT calculation has limited predictive

capabilities to guide experimental testing. Second, it requires intensive computation thus the model is limited to limited dimensions/ number of atoms. A lot of research has being conducted to overcome or minimize the shortcomings of DFT.

5.5.2 Time-dependent density functional theory (TDDFT)

TDDFT is an extension of DFT which shares the same conceptual and computational foundations. TDDFT aims at showing the relationship between the time dependent wave function and the electronic density. The effective potential of a hypothetical non-interacting system then can be revealed. TDDFT is mostly employed to calculate the energies of excited states of isolated systems as well as solids. Based on the calculation of changes of the electron density, the excitation energies of a system can be determined. To perform the calculation properly, exchange-correlation potential and the exchange-correlation kernel (the functional derivative of the exchange correlation potential with respect to the electronic density) are often introduced.

References

[1] A.J. Nozik, R. Memming, Physical chemistry of semiconductor-liquid interfaces, Journal of Physical Chemistry, 100 (1996) 13061-13078.

[2] A. Fujishima, X.T. Zhang, D.A. Tryk, TiO_2 photocatalysis and related surface phenomena, Surface Science Reports, 63 (2008) 515-582.

[3] T.A. Day, B.W. Howells, W.J. Rice, Ultraviolet-absorption and epidermal-transmittance spectra in foliage, Physiologia Plantarum, 92 (1994) 207-218.

[4] M.C. Flipse, R. Dejonge, R.H. Woudenberg, A.W. Marsman, C.A. Vanwalree, L.W. Jenneskens, The determination of first hyperpolarizabilities-beta using hyper-rayleigh scattering: A caveat, Chemical Physics Letters, 245 (1995) 297-303.

[5] M. Kahl, E. Voges, Analysis of plasmon resonance and surface-enhanced Raman scattering on periodic silver structures, Physical Review B, 61 (2000) 14078-14088.

[6] A. Mori, H. Masuda, K. Shikano, M. Shimizu, Ultra-wide-band tellurite-based fiber Raman amplifier, Journal of Lightwave Technology, 21 (2003) 1300-1306.

[7] N. Everall, T. Hahn, P. Matousek, A.W. Parker, M. Towrie, Picosecond time-resolved Raman spectroscopy of solids: Capabilities and limitations for fluorescence rejection and the influence of diffuse reflectance, Applied Spectroscopy, 55 (2001) 1701-1708.

[8] R. Bonneau, J. Wirz, A.D. Zuberbuhler, Methods for the analysis of transient absorbance data, Pure and Applied Chemistry, 69 (1997) 979-992.

[9] B. Dusemund, A. Hoffmann, T. Salzmann, U. Kreibig, G. Schmid, Cluster matter - the transition of optical elastic-scattering to regular reflection, Zeitschrift Fur Physik D-Atoms Molecules and Clusters, 20 (1991) 305-308.

[10] Z. Otwinowski, W. Minor, Processing of X-ray diffraction data collected in oscillation mode, Macromolecular Crystallography, Pt A, 276 (1997) 307-326.

[11] B.D. Cullity, Elements of X-ray diffraction, Third edition ed., Upper Saddle River, Prentice Hall, 2001.

[12] A.K. Datye, P.L. Hansen, S. Helveg, Electron microscopy and diffraction, 2008.

[13] J.W. Niemantsverfriet, Spectroscopy in Catalysis, Wiley, Weinheim, 2000.

[14] B.L. Henke, E.M. Gullikson, J.C. Davis, X-ray interactions - photoabsorption, scattering, transmission, and reflection at e=50-30,000 eV, Z=1-92, Atomic Data and Nuclear Data Tables, 54 (1993) 181-342.

[15] J.F. Moulder, Handbook of x-ray photoelectron spectroscopy : a reference book of standard spectra for identification and interpretation of XPS data, Perkin Elmer Corporation, Eden Prairie, 1992.
[16] C.C. Sweeley, R. Bentley, M. Makita, W.W. Wells, Gas-liquid chromatography of trimethylsilyl derivatives of sugars and related substances, Journal of the American Chemical Society, 85 (1963) 2497.
[17] H. Vandendool, P.D. Kratz, A generalization of retention index system including linear temperature programmed gas-liquid partition chromatography, Journal of Chromatography, 11 (1963) 463.
[18] H.H. Lauer, D. McManigill, R.D. Board, Mobile-phase transport-properties of liquefied gases in near-critical and supercritical fluid chromatography, Analytical Chemistry, 55 (1983) 1370-1375.
[19] L.A. Cole, J.G. Dorsey, Temperature-dependence of retention in reversed-phase liquid-chromatography .1. stationary-phase considerations, Analytical Chemistry, 64 (1992) 1317-1323.
[20] Y. Lin, R.G. Finke, A more general-approach to distinguishing "homogeneous" from "heterogeneous" catalysis: Discovery of polyoxoanion and Bu_4N^+-stabilized, isolable and redissolvable, high-reactivity $Ir_{\sim 190-450}$ nanocluster catalysts, Inorganic Chemistry, 33 (1994) 4891-4910.
[21] T. Ishii, H. Kato, A. Kudo, H-2 evolution from an aqueous methanol solution on $SrTiO_3$ photocatalysts codoped with chromium and tantalum ions under visible light irradiation, Journal of Photochemistry and Photobiology A-Chemistry, 163 (2004) 181-186.
[22] A. Mylonas, E. Papaconstantinou, V. Roussis, Photocatalytic degradation of phenol and p-cresol by polyoxotungstates. Mechanistic implications, Polyhedron, 15 (1996) 3211-3217.
[23] N. Lakshminarasimhan, W. Kim, W. Choi, Effect of the agglomerated state on the photocatalytic hydrogen production with in situ agglomeration of colloidal TiO_2 nanoparticles, Journal of Physical Chemistry C, 112 (2008) 20451-20457.

Chapter 6

$SrTiO_3$: Rh Photocatalyst Preparation and Characterization

6.1 Chapter introduction

$SrTiO_3$ is considered one of the best photocatalysts under UV-light [1]. The merits of this photocatalyst include good light response characteristics, highly stable properties and low cost [2, 3]. However, the wide bandgap of $SrTiO_3$ limits its practical applications such as photocatalytic hydrogen evolution driven by visible light [4]. There are a number of efforts to tailor the absorbance edge to visible region, as discussed in details in the previous chapters.

The most effective way to modify the bandgap of $SrTiO_3$ includes metal ions doping and co-catalyst loading. A lot of metal ions, such as Mn^-, Ru^-, Rh^-, Ir^-, Cr^{3+}, Cr^{3+} and Ta^{5+} (codoping), La^{3+} and N^{3-} (codoping), S and C cation codoping and etc., were proved to be effective dopant [3, 5-10]. In the previous research, solid state reaction (SSR) method and hydrothermal method were extensively employed to yield metal ions doped $SrTiO_3$ [11-14]. However, photocatalysts synthesized by SSR and hydrothermal reaction suffer from big particle size (thus increase the travelling path for an excited electron to travel to active sites on surface) and smaller surface area (less active sites).

Polymerizable complex (PC) method is a valuable synthesis method for solid state materials [15-18]. PC method yields higher crystallinity, smaller crystallite size and better size uniformity, which results in higher photocatalytic activity [19, 20]. In this work, Rh-doped $SrTiO_3$ photocatalysts was synthesized by using the PC method and compared it to SSR and hydrothermal method of preparation. To the best of our knowledge, this is the first synthesis of a Rh-doped photocatalyst by the PC method. This is also the first time this $SrTiO_3$ preparation method was utilized for photocatalytic applications.

For better comparison, hydrothermal method was also used for the preparation of Rh-doped $SrTiO_3$. The samples have been thoroughly characterized by XPS, XRD, TEM and UV-Vis spectroscopy analysis. The sample prepared by the PC method had significantly higher photocatalytic efficiency for hydrogen evolution as compared to that synthesized by other methods. The results of this work suggest that the PC method can be also applied to synthesis of other doped oxide materials for water splitting and environmental applications.

6.2 Experimental conditions

6.2.1 Catalyst preparation

In general, solid oxide materials can be synthesized by SSR method, hydrothermal method and PC method.

6.2.1.1 Rh doped $SrTiO_3$ prepared by SSR method

Strontium carbonate ($SrCO_3$, ≥99.9 %), Titanium (IV) oxide (TiO_2, anatase, ≥99.5 %) and Rhodium (III) oxide (Rh_2O_3, ≥99.8 %) were obtained from Aldrich. Prior weighting, all the precursors were heated at 60 ℃ in the air for dehumidification. $SrCO_3$, TiO_2 and Rh_2O_3 were then mixed according to their stoichiometric ratios followed by grinding for 30 mins to achieve homogeneous mixing. The mixture was then heated in a furnace with a heating rate of 10 ˚C/min from room temperature to the designated calcination temperature (500 ˚C, 600 ˚C, 700 ˚C, 800 ˚C, 1000 ˚C), and was then kept constant for 10 hours. The furnace was naturally cooled down to room temperature. The resulting samples were collected and bottled.

6.2.1.2 Rh doped $SrTiO_3$ prepared by hydrothermal method

Strontium hydroxide hydrates ($Sr(OH)_2 \bullet 8H_2O$, 99.995%), Rhodium (III) nitrate hydrates ($Rh(NO_3)_3 \bullet xH_2O$, ~36% Rhodium basis) were obtained from Aldrich and used without further treatment.

Amorphous TiO_2 was prepared according to the literature [21]. Briefly, 4 mL of 1.0 M nitric acid (HNO_3) was added to 396 mL of de-ionized water. A Teflon-coated magnetic stir bar was added and liquid was stirred vigorously. 10 mL of Titanium (IV) isopropoxide (Aldrich, 99.999%) was diluted with 90 mL 2-propanol and subsequently added slowly to the nitric acid solution. After stirring for 4 hours, the resulting white precipitate was collected and washed by de-ionized water until the pH of the resulting product reached pH=7. The amorphous TiO_2 was then desiccated at 60 ℃ in an oven for 10 hours and collected for next step synthesis.

$SrTiO_3$: Rh (1 mol %) was synthesized by the hydrothermal method adapted from the previously published literature [22]. Briefly, amorphous TiO_2 particles, strontium hydroxide hydrates and rhodium nitrate hydrates were added at appropriate molar ratios to 15 mL of distilled water. The suspension was subsequently transferred into a 23 mL Teflon-lined digestion acid bomb and then placed into an oven at 180 ℃ for 12 h. The resulting products were collected, washed with 1.0 M aqueous acetic acid solution and deionized water 3 times until the pH of

supernatant reached pH = 7. The resulting products were finally dried in an oven at 60 ℃ overnight.

6.2.1.3 Rh doped $SrTiO_3$ prepared by PC method

Starting materials were Titanium(IV) isopropoxide ($Ti[OCH(CH_3)_2]_4$ ($Ti(OiPr)_4$), 99.999%), Strontium carbonate ($SrCO_3$, ≥99.9 %) and Rhodium (III) nitrate hydrates ($Rh(NO_3)_3 \bullet xH_2O$, ~36% Rhodium basis) were obtained from Aldrich and used without further treatment. Ethylene glycol (EG) and methanol (CH_3OH) were used as solvents, and anhydrous citric acid (CA) was used as a complexing agent to stabilize the Ti^{4+}, Sr^{2+} and Rh^{3+} ions in solution. More specifically, $SrTiO_3$:Rh (Rh=0 - 5 mol %) was prepared using a 3:1 molar ratio of citric acid to metal to achieve the optimal metal chelation. The synthetic steps are described in Figure 6-1.

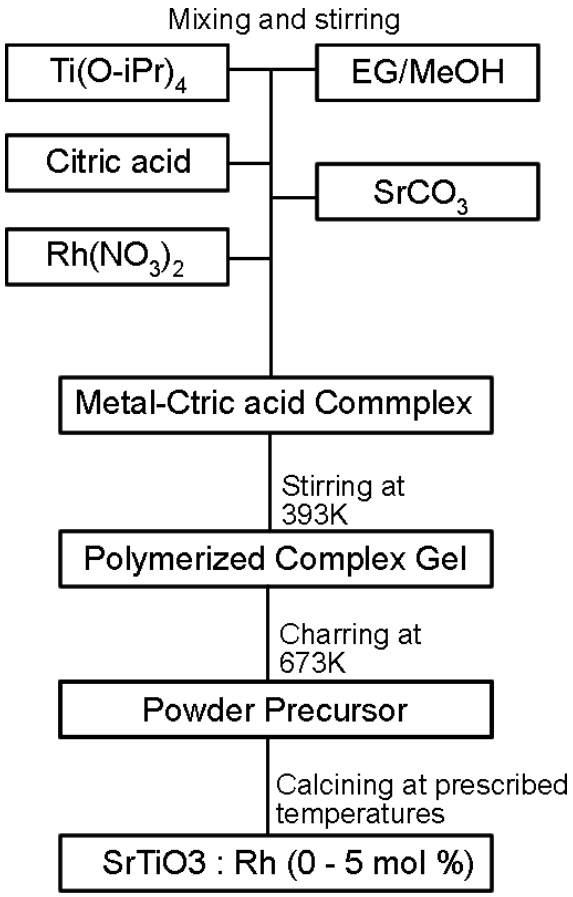

Figure 6-1 Schematic diagram for $SrTiO_3$: Rh synthesis by PC method.

Briefly, to yield 0.01 mol of $SrTiO_3$: Rh (1 mol %), $Ti(OiPr)_4$ (2.814 g, 0.0099 mol) was first dissolved in the mixture of CH_3OH (25.5 g, 0.8 mol) and EG (25.0 g, 0.4 mol). While the

solution was continuously stirred, CA (19.2 g, 0.1 mol) was added. Following a complete dissolution of the reagents, $SrCO_3$ was added. The resulting mixture was stirred at 50 ℃ until it became transparent at which point $Rh(NO_3)_2$ was added. The solution was subsequently stirred for another 30 minutes to achieve a complete dissolution of reactants, and then heated at 130 ℃ for several hours under continuous stirring to promote polymerization. After several hours of heating and evaporation of water and CH_3OH, the mixture gelled into a transparent brown resin. The resin was then heated at 400 ℃ for 2 hours. The resulting powders were calcined at 500 ℃. Additional samples were synthesized by varying the calcination temperatures to 600 ℃, 700 ℃, 850 ℃ and 1000 ℃.

6.2.1.4 Pt co-catalyst

To further enhance photocatalytic activity of the prepared materials, a Pt co-catalyst was loaded on the catalyst surface by an in situ photodeposition method. The procedure used 100 mg of Rh-doped $SrTiO_3$ suspended in 100 ml of an aqueous CH_3OH (20 vol. %) solution while a stoichiometric amount of $H_2PtCl_6 \cdot 6H_2O$ was added. The solution was then irradiated by a 300W Xe arc lamp for 10 hours. The sample was collected and washed with deionized water 3 times and then dried in an oven at 60 ℃ for 24 hours. In addition to Pt-modified samples, a set of Pt-free $SrTiO_3$ samples was also used for control experiment.

6.2.2 Catalyst characterization

Powder X-ray diffraction (XRD) patterns were obtained using a Rigaku Ultima IV diffractometer with CuKα radiation (40 kV and 40 mA) and a position sensitive detector (D/teX Ultra). The XRD patterns were collected at a rate of 1 °/min from 20 ° to 160 ° (2θ). Rietveld refinements were conducted using the fundamental parameters approach in the program TOPAS to model the instrument function, which allows for the refinement of crystallite size and strain [39].

Specimens for electron microscopy were prepared by suspending them in ethanol and followed by sonication for 5 minutes. Then a droplet of as prepared suspension solution was transferred to a copper grid coated with an amorphous carbon support. TEM images were recorded using a JEOL JEM 2100F (200 kV) Transmission Electron Microscope.

UV-Visible diffuse reflectance spectra were measured using a Thermo Evolution 3000 UV-Vis spectroscopy. About 100 mg of specimens were loaded in a holder. The specimens were packed to achieve better reflection and scanned by the UV-Vis spectrometer from 300 - 800 nm

with a step size of 2 nm/s. All the specimen underwent 3 scanning cycles for better resolution and accuracy.

X-ray photoelectron spectroscopy (XPS) was performed in a standard ultra-high vacuum (UHV) chamber, equipped with a hemispherical electron energy analyzer (100 mm mean radius; Oxford Applied Research, VSW 100) and an Al/Mg twin anode x-ray tube (PSP Vacuum Technology, TX400/2). The sample was prepared by pressing the catalyst powder between two plates (10 x 10 x 1 mm) at a pressure of ~2000 psi. One of the loaded plates was then clamped into a molybdenum holder that could be resistively heated to above 900 K. The XPS spectra were obtained using unmonochromatized Al Kα (1486.6 eV) radiation. Atom-specific core level spectra were taken at an analyzer pass energy of 35 eV, with a step size of 0.2 eV, and dwell time of 0.5 sec. Each region was signal averaged for 5 scans except for Rh which was averaged over 20 scans to improve the signal to noise ratio that was a result of the low rhodium concentration in the sample. Analysis of the XPS spectra was performed using Presents software (Oxford Applied Research). The O 1s peak at 529.5 eV of $SrTiO_3$ was used to calibrate the energy scale to which all the measured binding energies were adjusted [23, 24]. A Shirley background was applied to the spectra which were then fit with an appropriate number of peaks. The fits were allowed to optimize without constraints as long as a reasonable FWHM (below 3 eV) and goodness of fit were obtained. In cases where a FWHM greater than 3 eV occurred, widths and/or known peak separations were fixed to one another, until an acceptable fit was achieved. The atomic sensitivity factors [25] of 0.63 (O), 1.1 (Ti), 1.05 (Sr), and 1.75 (Rh) were used to correct for differences in photoemission cross sections to obtain relative surface atomic compositions.

6.3 Results and discussion

6.3.1 X-ray powder diffraction of $SrTiO_3$: Rh synthesized by the PC method

To answer the question whether Rh dopant can alter the crystalline structure of $SrTiO_3$, Rh doping effect was first investigated. Different Rh doping concentrations were achieved by varying the stoichiometric ratio of Sr^{2+}, Ti^{4+} and Rh^{4+} precursors.

Figure 6-2 shows XRD patterns of $SrTiO_3$: Rh samples with different Rh doping concentration prepared by the PC method. All the work of XRD characterization was a result of the cooperation with Prof. John Praise from Department of Geosciences, Stony Brook University.

Here, 3 samples were selected and presented, including 0%, 1% and 5% Rh doping concentrations.

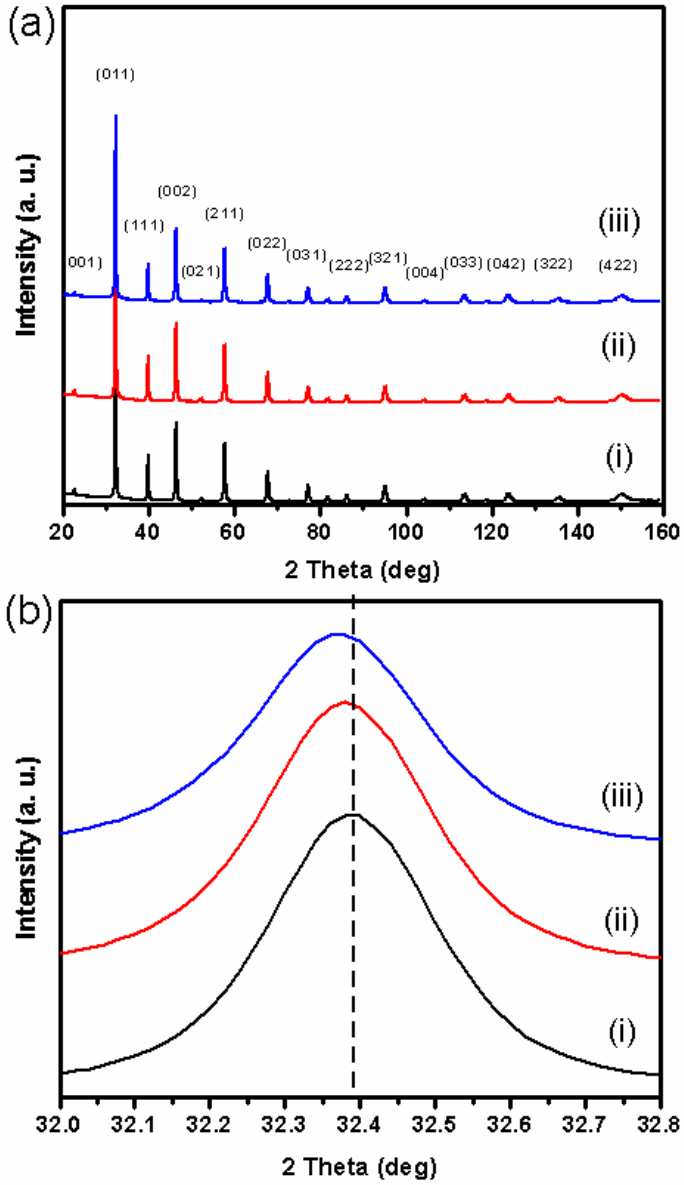

Figure 6-2 XRD patterns of $SrTiO_3$: Rh (0, 1, and 5 mol %). (a) XRD patterns of the three samples with the indexed reflections, (i) 0 mol % (ii) 1 mol % (iii) 5 mol %. (b) Magnified area from 32.0 to 32.8 2 theta degree showing (110) of $SrTiO_3$: Rh shifting to smaller angle, (i) 0 mol % (ii) 1 mol % (iii) 5 mol %.

Diffraction measurements showed that all the samples were single phase with nearly identical perovskite $SrTiO_3$ crystal structures. These results indicate that substitutional doping of up to 5

mol % of Rh cations did not introduce impurities and had a minimal effect on crystal structure. In another word, $SrTiO_3$: Rh prepared by PC method maintained the defect concentration at a relatively low level, leading to the recombination of electrons and holes minimum.

The integral breadth volume-weighted crystallite size (LVol-IB) was determined to be 45.80(70) nm, 45.02(78) nm, and 44.44(95) nm for pure $SrTiO_3$, $SrTiO_3$: Rh (1 mol %), and $SrTiO_3$: Rh (5 mol %), respectively, which shows that the volume weighted mean particle size (~46 nm) and distribution in the three samples were very similar. Rietveld refinements revealed that the lattice expansion is very small as more Rh was introduced into the structure. This can be visualized by the shift of the (011) reflection towards smaller angle with increasing dopant concentration (Figure 6-2(b)). The small structural changes are consistent with the similar ionic radii of Rh^{4+} (60.5 pm) and Ti^{4+} (60 pm) and substitutional doping of Rh^{4+} for Ti^{4+}. The results of the Rietveld refinements are summarized in Table 6-1.

Table 6-1: Rietveld refinement results of $SrTiO_3$: Rh with Rh doping concentration at 0, 1 and 5 mol %, respectively.

Sample	$SrTiO_3$	$SrTiO_3$: Rh (1 mol %)	$SrTiO_3$: Rh (5 mol %)
a lattice parameter (Å)	3.907041(26)	3.907261(23)	3.908254(32)
IVol-IB (nm)	45.80(70)	45.02(78)	44.44(95)
GOF	2.00	2.09	1.67
Rwp	3.72	3.88	3.08

$SrTiO_3$: Rh samples synthesized by PC method were also subjected to calcination temperature investigation. Since calcination temperature plays a key role in photocatalytic activity understanding, precursor powders (with a certain Rh doping concentration) were underwent different calcination temperatures to avoid other variances which can be introduced during the sample preparation procedure. Figure 6-3 shows XRD patterns of $SrTiO_3$: Rh (1 mol %) samples prepared by the PC method at different calcination temperatures ranging from 500 ℃ to 1000 ℃. All the samples exhibit cubic structure and the strongest diffraction peak corresponds to the (110) plane reflection. Sample calcined at 450 ℃ showed amorphous nature, while sample calcined at 500 ℃ clearly showed some certain degrees of crystallinity. These results indicated the turning point of amorphous and crystallization of $SrTiO_3$: Rh prepared by PC method was between 450 -500 ℃. As the calcination temperature is increased, the intensity

of the all peaks went up accordingly, indicating that the samples calcined at higher temperatures are more crystalline.

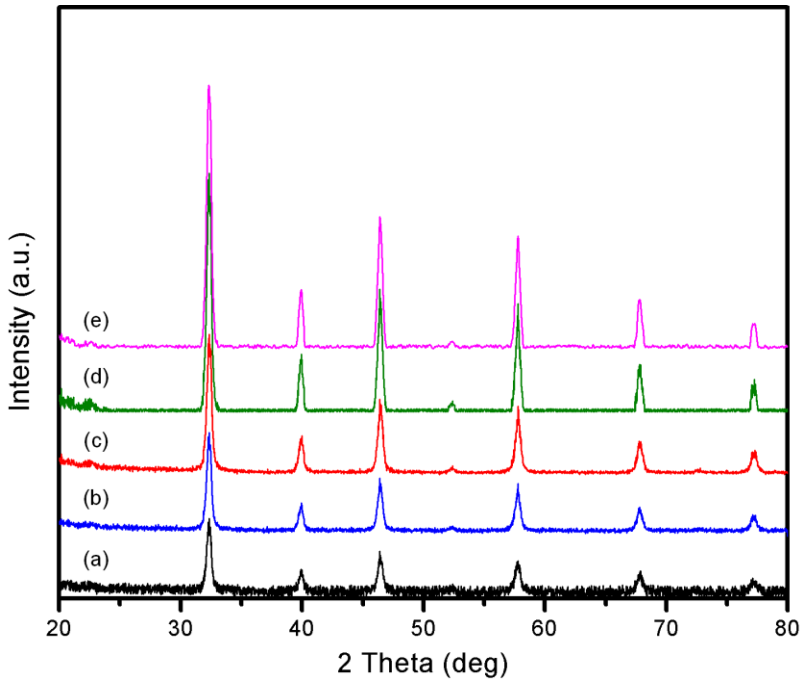

Figure 6-3 XRD patterns of $SrTiO_3$: Rh (1 mol %) prepared by PC method and calcined at different temperatures. (a) 500 °C (b) 600 °C (c) 700 °C (d) 850 °C and (e) 1000 °C.

Other $SrTiO_3$ samples with different Rh doping concentration (0, 0.5, 2, 5%) prepared by PC method were investigated calcination effects as well. These samples showed the similar characteristics and trends as $SrTiO_3$: Rh (1 %) under different calcination temperatures.

6.3.2 X-ray photoelectron spectroscopy of $SrTiO_3$: Rh synthesized by the PC method

We employed X-ray photoelectron spectroscopy for $SrTiO_3$: Rh electron state understanding. The most active samples, $SrTiO_3$: Rh (1 mol %) synthesized by PC method and calcined at 700 ˚C, $SrTiO_3$: Rh (1 mol %) synthesized by SSR method and calcined at 1000 ˚C and $SrTiO_3$: Rh (1 mol %) synthesized by hydrothermal method at 180˚C were selected for XPS characterization. All the work of XPS characterization was a result of the cooperation with Prof. Michael White from Department of Chemistry, Stony Brook University. Prior this work, $SrTiO_3$: Rh has never been subjected to XPS investigation. The electronic states of Rh doping are essential for photocatalytic activity enhancement. XPS can provide valuable information of chemical state,

electronic state of the elements in the sample, thus a comprehensive evaluation of the synthesized samples in bandgap structure can be determined.

Figure 6-4(a) shows Rh 3d XPS spectrum of the as prepared $SrTiO_3$: Rh (1 mol %) sample produced by the PC method. The spectrum was fitted with a doublet indicating only a single oxidation state (black squares are experimental data while the colored lines are the fits). Here rhodium is present in the 4^+ oxidation state as evidenced by a 3d5/2 binding energy of 309.3 eV [26]. The as prepared $SrTiO_3$: Rh (1 mol %) synthesized by the SSR method, shown in Figure 6-4(b), exhibited a similar Rh 3d spectrum to that of PC and hydrothermal samples, with the Rh^{4+} being the dominant species. These samples also exhibited very similar O 1s spectra with binding energies consistent with lattice oxygen from $SrTiO_3$ (see Figure 6-5) [23, 24, 26].

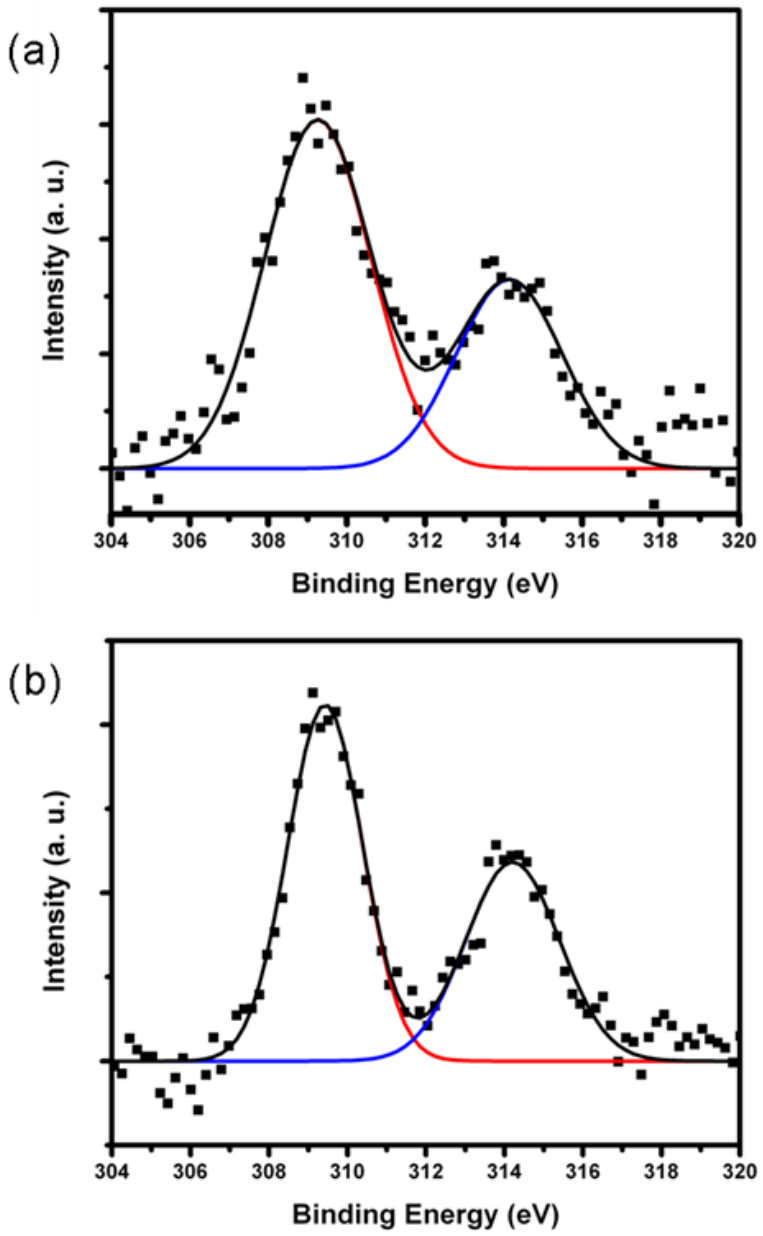

Figure 6-4: Fitted Rh 3d x-ray spectrum of as prepared $SrTiO_3$: Rh (1 mol %) produced by different methods. (a) PC method (b) SSR method. Black line is the original data, red line is the 5/2 fit, and blue line is the 3/2 fit.

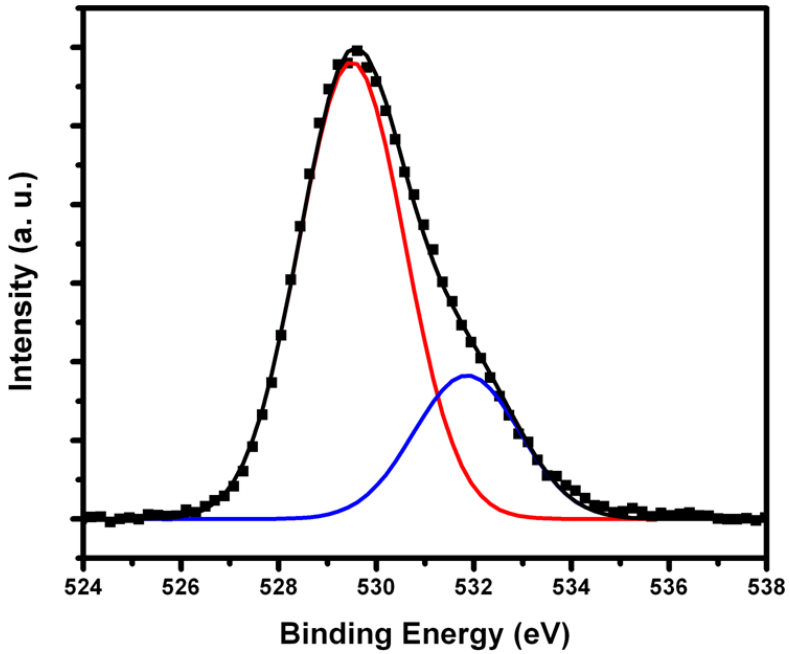

Figure 6-5: Fitted O 1s X-ray spectrum of $SrTiO_3$: Rh (1 mol %) produced by PC method after annealing. Black line is the original data, red line is the O fit and blue line is the OH fit.

When the samples were annealed at 850 K in vacuum for 30 min, the XPS spectra of the SSR, hydrothermal and the PC samples became distinctly different. As shown in Figure 6-6, the Rh 3d spectrum for the SSR and hydrothermal samples after annealing show the presence of two doublets whose 3d5/2 binding energies are consistent with Rh^0 and Rh^{4+}. The appearance of Rh^0 suggests that some of the Rh^{4+} in the as synthesized SSR and hydrothermal samples exist as a surface oxide, which is then converted to metallic nanoparticles during high temperature annealing. By contrast, the Rh 3d spectrum of the PC sample (see Figure 6-6) was essentially unchanged after annealing with a single 3d doublet assignable to Rh^{4+}.

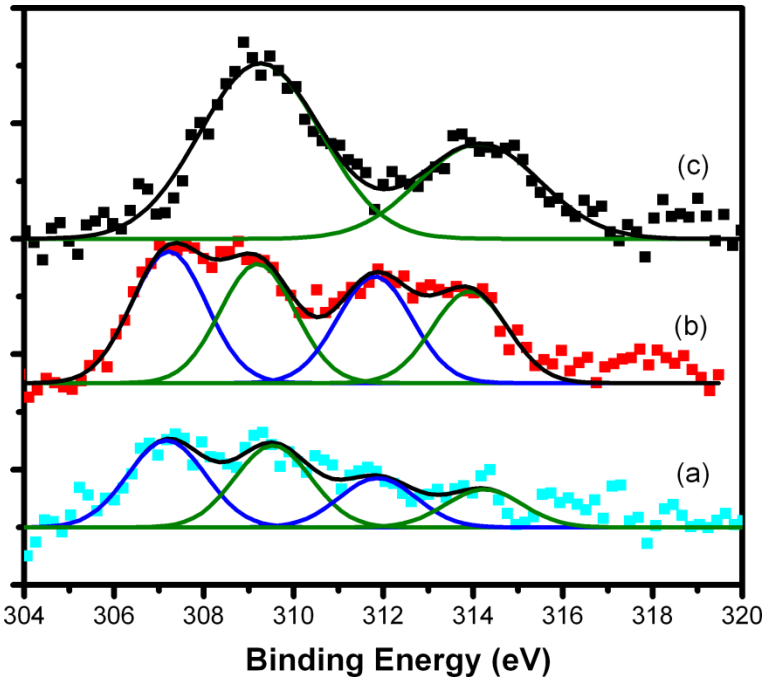

Figure 6-6 Fitted Rh 3d x-ray spectra of Rh-doped $SrTiO_3$ samples prepared by different methods after a 30 minute anneal at 850 K. (a) hydrothermal method (cyan line, synthesized at 180 ˚C), (b) SSR method (red line, calcined at 1000 ˚C) and (c) PC method (black line, calcined at 700 ˚C). The green fits are for Rh^{4+} and the blue fits are for Rh^0.

These results indicate that the Rh^{4+} species in the PC samples are located mostly in the lattice, whereas the SSR sample has Rh^{4+} in the lattice and on the surface as Rh oxide deposits. Moreover, annealing of the PC sample did not cause any significant changes in the binding energies of the Sr, Ti, or O from the literature reported values for $SrTiO_3$, further confirming the sample's stability [23, 24]. The only other species present on the PC sample (1 mol % Rh) were hydroxyl species (OH) with an O 1s binding energy of 531.8 eV as shown in Fig 6-5 [27].

In addition to the 1 mol % sample, Rh 3d XPS spectra of the 0.7 mol % and 5 mol % Rh-doped samples were also taken (not shown). In general, the Rh 3d peak widths (FWHM) for the PC samples were generally wider (~1 eV) than those for the SSR and hydrothermal samples, however, the spectra of the PC samples could only be fit by a single 3d doublet. This result is consistent with our earlier conclusion that the Rh4+ species in the PC samples are located in lattice sites with similar chemical environments. Table 6-2 summarizes the binding energy, assignment, and adjusted area for each species on the surface for Rh doping of $SrTiO_3$ at 0.7, 1, 5 mol % doping levels. All binding energies for each sample were consistent with each other and

are also in good agreement with the literature values for $SrTiO_3$ and Rh oxide (RhO_2) [23, 24, 26].

Table 6-2 Summary of binding energies, assignments, and calculated area of each atomic species for $SrTiO_3$: Rh (0.7, 1, 5 mol %).

Sample	Exp. BE (eV)	Assignment	Adjusted Area
$SrTiO_3$: Rh (0.7 mol %)			
Rh	309.0	$Rh(^{4+})O_2$	197.41 ($3d_{5/2}$)
Sr	132.5	$Sr(^{2+})TiO_3$	10493.70 (3d)
Ti	458.2	$SrTi(^{4+})O_3$	6664.72 ($2p_{3/2}$)
O1	529.5	$SrTiO_3(^{2+})$	22297.20 (1s)
O2	531.9	OH	5619.40(1s)
$SrTiO_3$: Rh (1 mol %)			
Rh	309.3	$Rh(^{4+})O2$	248.33 ($3d_{5/2}$)
Sr	132.3	$Sr(^{2+})TiO3$	12185.20 (3d)
Ti	458.1	$SrTi(^{4+})O3$	7769.77 ($2p_{3/2}$)
O1	529.5	$SrTiO_3$ ($^{2+}$)	25074.10 (1s)
O2	531.8	OH	7875.03 (1s)
$SrTiO_3$: Rh (5 mol %)			
Rh	309.3	$Rh(^{4+})O_2$	546.99 ($3d_{5/2}$)
Sr	132.4	$Sr(^{2+})TiO_3$	5733.57 (3d)
Ti	458.0	$SrTi(^{4+})O_3$	7092.11 ($2p_{3/2}$)
O1	529.5	$SrTiO_3$ ($^{2+}$)	22042.70 (1s)
O2	531.2	OH	2977.10 (1s)

The observation of Rh^{4+} in all the samples is consistent with the expectation that Rh^{4+} would most readily substitute for Ti^{4+} based on both charge balance and the similarity in cation size. The relative elemental concentrations obtained from XPS for the PC samples, however, actually show that the Sr^{2+} abundance changes with Rh substitution, whereas the Ti^{4+} abundance is roughly constant (see Table 6-3).

Table 6.3: Summary of compositional ratios determined using the fitted XPS peak areas corrected for elemental sensitivity factors. Calculated stoichiometry was determined using the corrected peak areas and by fixing the value of oxygen to 3.

%Rh (mole percent)	Rh/O	Ti/O	Sr/O	Sr/Ti	Rh/Ti	Rh/Sr	Calculated Stoichiometry Rh : Sr : Ti : O
0.7	0.01	0.30	0.47	1.6	0.03	0.02	0.03 : 1.4 : 0.9 : 3.0
1.0	0.01	0.31	0.49	1.6	0.03	0.02	0.03 : 1.5 : 0.9 : 3.0
2.0	0.01	0.31	0.41	1.3	0.04	0.03	0.04 : 1.2 : 0.9 : 3.0
5.0	0.03	0.32	0.26	0.8	0.08	0.09	0.07 : 0.8 : 1.0 : 3.0

Due to the limited escape depth of the electrons sampled by XPS (~1 nm), we believe these concentration ratios are more representative of the surface and less so of the bulk material. Indeed, it is well known that $SrTiO_3$ surfaces can be SrO or TiO_2 terminated (or both) such that the actual surface composition will depend on the details of the preparation method and post synthesis treatments [28, 29]. This is more clearly seen in the overall stoichiometry of the Rh-doped PC samples obtained from the XPS data (see Table 6-2), which suggest that the 0.7%, 1.0% and 2% samples are Sr rich, whereas the 5% is Sr deficient. Again, these compositions are more likely to be indicative of the surface composition, since such large changes in stoichiometry from the $SrTiO_3$ starting material should have resulted in more significant changes in the XRD patterns which are mostly bulk sensitive (see Figure 6-2).

6.3.3 Diffuse reflectance UV-Vis spectroscopy of $SrTiO_3$: Rh synthesized by the PC method

Diffuse reflectance spectra of undoped $SrTiO_3$, $SrTiO_3$: Rh (1 mol %) and $SrTiO_3$: Rh (5 mol %) prepared by the PC method are shown in Figure 6-7. The undoped $SrTiO_3$ prepared by PC method showed an absorbance edge at 385 nm (bandgap = 3.2 eV), consistent with the published literature [7]. In contrast, the absorption edges for the Rh-doped samples are shifted to significantly longer wavelengths (lower energy) with two features near 520 nm and 580 nm. Kudo assigned the adsorption peak at 580 nm to an electronic transition from the valence band to Rh^{4+} acceptor levels in the bandgap [30]. The latter results in occupied Rh^{3+} levels and photon absorption from these states to the conduction band give rise to the 580 nm peak. This description suggests that the Rh4+ donor levels act as intermediate states for multiple photon transitions that allow electron-hole pair excitation in $SrTiO_3$ with visible light.

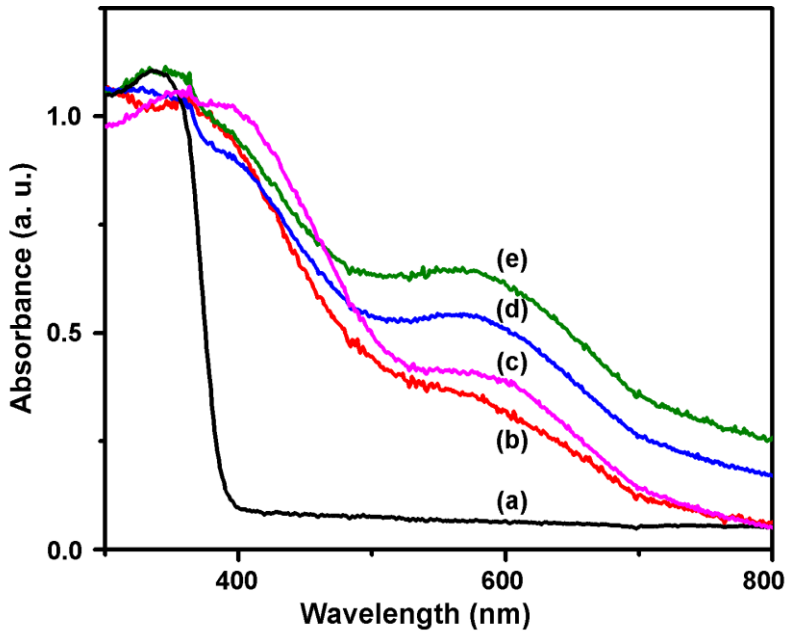

Figure 6-7 Diffuse reflectance spectra of $SrTiO_3$ synthesized by PC method with different level of Rh doping. (a) undoped $SrTiO_3$, (b) $SrTiO_3$: Rh (0.5 mol %) (c) $SrTiO_3$: Rh (1 mol %) (d) $SrTiO_3$: Rh (2 mol %) (e) $SrTiO_3$: Rh (5 mol %).

6.3.4 TEM characterization of $SrTiO_3$: Rh synthesized by the PC method

Figure 6-8 shows an HRTEM image of Pt (0.5 wt. %) - $SrTiO_3$: Rh (1 mol %) prepared by the PC method with Pt nanoparticle co-catalyst added by photo-deposition. The addition of Pt co-catalyst is a well-known strategy to improve photocatalytic activity for hydrogen production [31, 32]. The sizes of the $SrTiO_3$: Rh particles ranged from 20 nm to 30 nm, which were comparable to the average size obtained from the XRD analysis. A higher magnification HRTEM image (Figure 6-8(b)) shows fringe spacings of about 0.277 nm along two mutually orthogonal directions, which can be identified with the (110) crystal plane of $SrTiO_3$. The average size of the Pt particles was about 3-4 nm, which was comparable to that obtained in previous studies using photodeposition [33, 34]. HRTEM of the Pt nanoparticles also showed fringe spacings of about 0.196 nm corresponding to the (100) crystal plane of Pt.

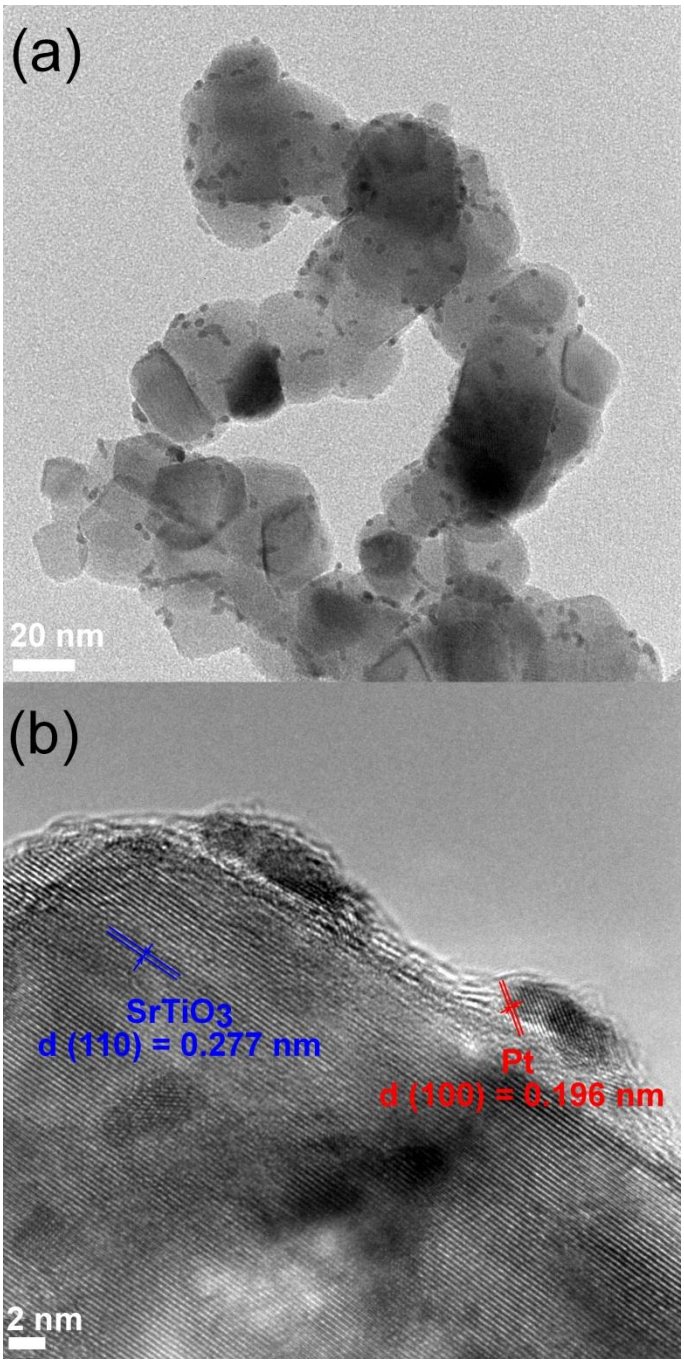

Figure 6-8 TEM images of Pt (0.5 wt. %)-$SrTiO_3$: Rh (1 mol %) synthesized by PC method. (a) Low magnification TEM image of Pt (0.5 wt. %)-$SrTiO_3$: Rh (1 mol %). The particle size of $SrTiO_3$: Rh (1 mol %) ranged between 20 nm - 30 nm. (b) HRTEM of Pt (0.5 wt. %)-$SrTiO_3$: Rh (1 mol %). Lattice spacing of the $SrTiO_3$: Rh (1 mol %) was 0.277 nm for corresponding (110) orientation, while lattice spacing of Pt was 0.196 nm for corresponding (100) crystal plane.

References

[1] K. Domen, A. Kudo, T. Onishi, Mechanism of photocatalytic decomposition of water into H_2 and O_2 over NiO-$SrTiO_3$, Journal of Catalysis, 102 (1986) 92-98.

[2] H. Kato, A. Kudo, Visible-light-response and photocatalytic activities of TiO_2 and $SrTiO_3$ photocatalysts codoped with antimony and chromium, Journal of Physical Chemistry B, 106 (2002) 5029-5034.

[3] R. Konta, T. Ishii, H. Kato, A. Kudo, Photocatalytic activities of noble metal ion doped $SrTiO_3$ under visible light irradiation, Journal of Physical Chemistry B, 108 (2004) 8992-8995.

[4] F.T. Wagner, G.A. Somorjai, Photocatalytic hydrogen-production from water on Pt-free $SrTiO_3$ in alkali hydroxide solutions, Nature, 285 (1980) 559-560.

[5] T. Ishii, H. Kato, A. Kudo, H_2 evolution from an aqueous methanol solution on $SrTiO_3$ photocatalysts codoped with chromium and tantalum ions under visible light irradiation, Journal of Photochemistry and Photobiology A-Chemistry, 163 (2004) 181-186.

[6] M. Miyauchi, M. Takashio, H. Tobimatsu, Photocatalytic activity of $SrTiO_3$ codoped with nitrogen and lanthanum under visible light illumination, Langmuir, 20 (2004) 232-236.

[7] J.W. Liu, G. Chen, Z.H. Li, Z.G. Zhang, Electronic structure and visible light photocatalysis water splitting property of chromium-doped $SrTiO_3$, Journal of Solid State Chemistry, 179 (2006) 3704-3708.

[8] T. Ohno, T. Tsubota, Y. Nakamura, K. Sayama, Preparation of S, C cation-codoped $SrTiO_3$ and its photocatalytic activity under visible light, Applied Catalysis A-General, 288 (2005) 74-79.

[9] J.S. Wang, S. Yin, M. Komatsu, T. Sato, Lanthanum and nitrogen co-doped $SrTiO_3$ powders as visible light sensitive photocatalyst, Journal of the European Ceramic Society, 25 (2005) 3207-3212.

[10] H. Irie, Y. Maruyama, K. Hashimoto, Ag^+ and Pb^{2+} doped $SrTiO_3$ photocatalysts. A correlation between band structure and photocatalytic activity, Journal of Physical Chemistry C, 111 (2007) 1847-1852.

[11] D.F. Wang, J.H. Ye, T. Kako, T. Kimura, Photophysical and photocatalytic properties of $SrTiO_3$ doped with Cr cations on different sites, Journal of Physical Chemistry B, 110 (2006) 15824-15830.

[12] Y. Liu, L. Xie, Y. Li, R. Yang, J.L. Qu, Y.Q. Li, X.G. Li, Synthesis and high photocatalytic hydrogen production of $SrTiO_3$ nanoparticles from water splitting under UV irradiation, Journal of Power Sources, 183 (2008) 701-707.

[13] J.S. Wang, S. Yin, T. Sato, Characterization and evaluation of fibrous $SrTiO_3$ prepared by hydrothermal process for the destruction of NO, Journal of Photochemistry and Photobiology A-Chemistry, 187 (2007) 72-77.

[14] H.W. Kang, S.B. Park, H_2 evolution under visible light irradiation from aqueous methanol solution on $SrTiO_3$:Cr/Ta prepared by spray pyrolysis from polymeric precursor, International Journal of Hydrogen Energy, 36 (2011) 9496-9504.

[15] A. Kudo, Y. Miseki, Heterogeneous photocatalyst materials for water splitting, Chemical Society Reviews, 38 (2009) 253-278.

[16] X.B. Chen, S.H. Shen, L.J. Guo, S.S. Mao, Semiconductor-based photocatalytic hydrogen generation, Chemical Reviews, 110 (2010) 6503-6570.

[17] M. Kakihana, M. Yoshimura, Synthesis and characteristics of complex multicomponent oxides prepared by polymer complex method, Bulletin of the Chemical Society of Japan, 72 (1999) 1427-1443.

[18] M. Yoshino, M. Kakihana, Polymerizable complex synthesis of pure $Sr_2Nb_xTa_{2-x}O_7$ solid solutions with high photocatalytic activities for water decomposition into H_2 and O_2, Chemistry of Materials, 14 (2002) 3369-3376.

[19] R. Abe, Recent progress on photocatalytic and photoelectrochemical water splitting under visible light irradiation, Journal of Photochemistry and Photobiology C-Photochemistry Reviews, 11 (2010) 179-209.

[20] H.G. Kim, D.W. Hwang, S.W. Bae, J.H. Jung, J.S. Lee, Photocatalytic water splitting over $La_2Ti_2O_7$ synthesized by the polymerizable complex method, Catalysis Letters, 91 (2003) 193-198.

[21] X. Chen, S.S. Mao, Titanium dioxide nanomaterials: Synthesis, properties, modifications, and applications, Chemical Reviews, 107 (2007) 2891-2959.

[22] Y. Wang, H. Xu, X. Wang, X. Zhang, H. Jia, L. Zhang, J. Qiu, A general approach to porous crystalline TiO2, SrTiO3, and BaTiO3 spheres, Journal of Physical Chemistry B, 110 (2006) 13835-13840.

[23] A. Kosola, M. Putkonen, L.S. Johansson, L. Niinisto, Effect of annealing in processing of strontium titanate thin films by ALD, Applied Surface Science, 211 (2003) 102-112.
[24] T.X. Wang, W.W. Chen, Solid phase preparation of submicron-sized SrTiO3 crystallites from SrO2 nanoparticles and TiO2 powders, Mater. Lett., 62 (2008) 2865-2867.
[25] C.D. Wagner, W.M. Riggs, Handbook of X-ray photoelectron spectroscopy, Eden Prairie, MN, 1979.
[26] Z. WengSieh, R. Gronsky, A.T. Bell, Microstructural evolution of gamma-alumina-supported Rh upon aging in air, Journal of Catalysis, 170 (1997) 62-74.
[27] G.S. Herman, Y.J. Kim, S.A. Chambers, C.H.F. Peden, Interaction of D_2O with CeO_2(001) investigated by temperature-programmed desorption and X-ray photoelectron spectroscopy, Langmuir, 15 (1999) 3993-3997.
[28] D.S. Deak, Strontium titanate surfaces, Mater Sci Tech-Lond, 23 (2007) 127-136.
[29] D.A. Bonnell, J. Garra, Scanning probe microscopy of oxide surfaces: atomic structure and properties, Rep Prog Phys, 71 (2008).
[30] Y. Sasaki, H. Nemoto, K. Saito, A. Kudo, Solar water splitting using powdered photocatalysts driven by Z-schematic interparticle electron transfer without an electron mediator, Journal of Physical Chemistry C, 113 (2009) 17536-17542.
[31] H. Haick, Y. Paz, Long-range effects of noble metals on the photocatalytic properties of titanium dioxide, Journal of Physical Chemistry B, 107 (2003) 2319-2326.
[32] A. Patsoura, D.I. Kondarides, X.E. Verykios, Enhancement of photoinduced hydrogen production from irradiated Pt/TiO_2 suspensions with simultaneous degradation of azo-dyes, Appl Catal B-Environ, 64 (2006) 171-179.
[33] M.C. Hidalgo, M. Maicu, J.A. Navio, G. Colon, Photocatalytic properties of surface modified platinised TiO_2: Effects of particle size and structural composition, Catalysis Today, 129 (2007) 43-49.
[34] Y.X. Li, J. Du, S.Q. Peng, D. Xi, G.X. Lu, S.B. Li, Enhancement of photocatalytic activity of cadmium sulfide for hydrogen evolution by photoetching, International Journal of Hydrogen Energy, 33 (2008) 2007-2013.

Chapter 7

Photocatalytic Hydrogen Evolution of $SrTiO_3$: Rh Photocatalyst

7.1 Chapter introduction

$SrTiO_3$: Rh prepared by PC method has good crystallinity, stable electronic states and relatively small particle sizes as presented by the previous chapter (Chapter 6). However, whether these properties play important roles in hydrogen production are largely unknown. The experimental results presented in this chapter are focused on photocatalytic activities for various samples of $SrTiO_3$: Rh synthesized under different preparation conditions. The roles of Rh doping concentration, sample calcination temperature, pH during the synthesis and preparation methods are illustrated and discussed in details. Stability of the samples was tested through 60 hours continuous photocatalytic activity testing. The behaviors of various noble metal co-catalysts on $SrTiO_3$: Rh were also investigated.

7.2 Experimental conditions

Photocatalytic reactions were carried out in a customized reactor connected to a closed gas circulation and evacuation system. For each experiment, 50 mg of the photocatalyst was dispersed in 50 ml of a CH_3OH aqueous solution (CH_3OH, 20 vol. %). The suspension was put in the dark and purged with argon while being stirred for 30 minutes, followed by a degassing procedure. Afterwards, 40 Torr of argon was introduced into the system as the carrier gas. Then, the suspension was irradiated by a 300W Xe lamp (Newport, Model 66984) equipped with an optical cutoff filter (λ>420 nm, L42, Hoya) to eliminate UV and a 10 cm water filter (λ<800 nm) to eliminate IR radiation. The evolved H_2 gas was quantified by using an inline gas chromatograph (Agilent 7890A) equipped with a thermal conductivity detector and a 5Å molecular sieve column.

For most photocatalysts, prior to photocatalytic activity testing, co-catalysts were loaded on the samples through photo-deposition to further enhance the photocatalytic activities. The detailed loading method was discussed in the previous chapter.

7.3 Results and discussion

7.3.1 Dependence of photocatalytic activity of hydrogen evolution over Pt/$SrTiO_3$: Rh prepared by the PC method on different Rh doping concentration

Six samples, synthesized by PC method, however, with different Rh doping concentrations were prepared for photocatalytic activity in hydrogen evolution testing. The detailed doping concentrations were: 0, 0.5, 0.7, 1, 2 and 5 mol % Rh. To be note, all the samples were loaded

with 0.5 wt. % Pt as co-catalyst for activity enhancement. A significant change in photocatalytic activities were observed with different Rh doping concentration, as shown in Figure 7-1.

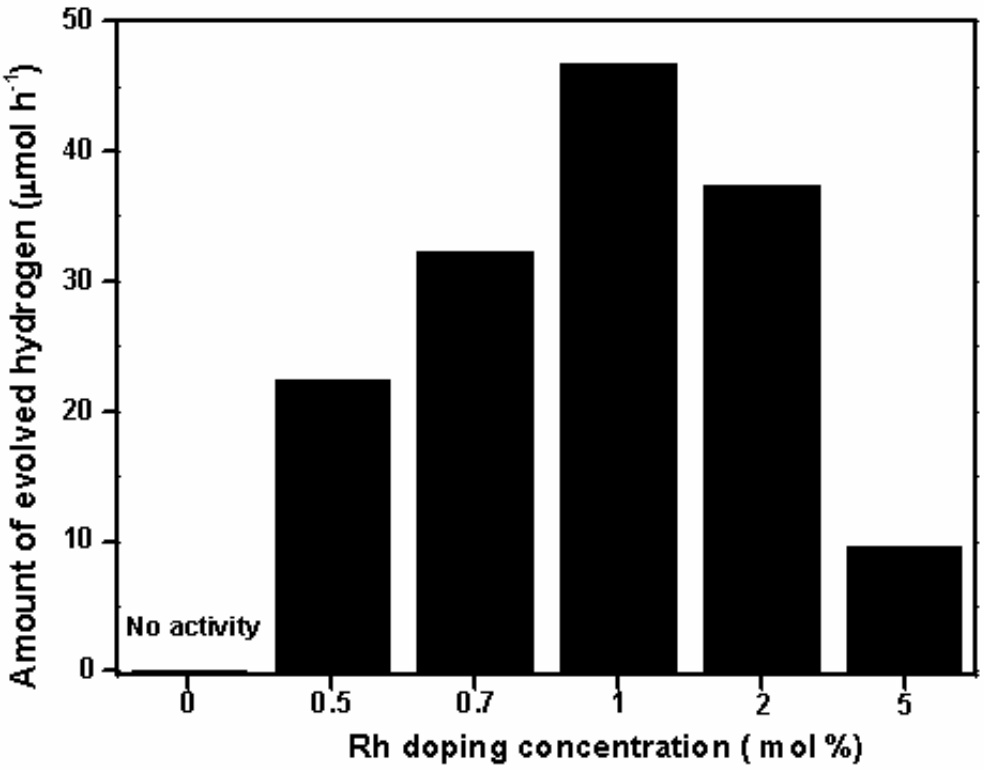

Figure 7-1 Rates of hydrogen evolution for $SrTiO_3$: Rh synthesized by PC method with different Rh doping concentrations. All the samples were loaded with Pt (0.5 wt. %) as co-catalyst. Catalyst weight: 50 mg.

Undoped $SrTiO_3$ exhibited no activity under visible light, as expected. By contrast, Pt/$SrTiO_3$: Rh (1-5 mol %) exhibits hydrogen evolution with visible light excitation, with a rate that strongly depends on doping level. When doped with only 0.5 mol % Rh, the activity increased to 23.4 $\mu molh^{-1}$. The best activity was observed at 1 mol % Rh doping, where the H_2 a production rate was 48.1 $\mu molh^{-1}$. Keeping increase of Rh doping concentration resulted in a decrease trend in photocatalytic H_2 evolution. The reasons might be various. One of the important reasons was Rh dopant could introduce in some certain degrees of lattice distortion. Defects could be evolved after the lattice of $SrTiO_3$ was distorted. With the Rh doping concentration increasing, the density of defects could be largely increased. These defects severed as recombination centers thus lowered the efficiency of electron-hole separation, and then resulted in declining of photocatalytic activity in hydrogen evolution.

7.3.2 Dependence of photocatalytic activity of hydrogen evolution over Pt/$SrTiO_3$: Rh prepared by the PC method on different calcination temperature

Calcination temperature can largely affect a photocatalyst including physical properties, chemical properties and electronic structures. Calcination temperature is very important for photocatalyst optimization and development. In this research, $SrTiO_3$: Rh (Rh = 1 mol %), the most active sample discovered from the previous chapter (1.3.1), was selected for calcination temperature effect investigation.

Several samples were prepared at different calcination temperatures: 450, 500, 600, 850 and 1000 ˚C. Before the samples were tested for photocatalytic activity in hydrogen evolution, all the samples were loaded with 0.5 wt. % Pt as co-catalyst for activity enhancement. The results are shown in Figure 7-2. No photocatalytic activity was observed for samples calcined at temperatures below 450 ˚C, which is probably related to the amorphous nature of these samples. With increasing calcination temperatures, the photocatalytic activity of $SrTiO_3$: Rh (1 mol %) catalysts also increased, reaching the maximum value at 700 ˚C (48.1 $\mu molh^{-1}$). Increasing temperatures above 700 ˚C resulted in a decrease in activity. This decrease might be related to an increase in crystallite size as indicated by XRD results (Table 7-1). The crystallite size is inversely related to illuminated surface area of photocatalysts and therefore should be linked to decrease in photocatalytic activity [1].

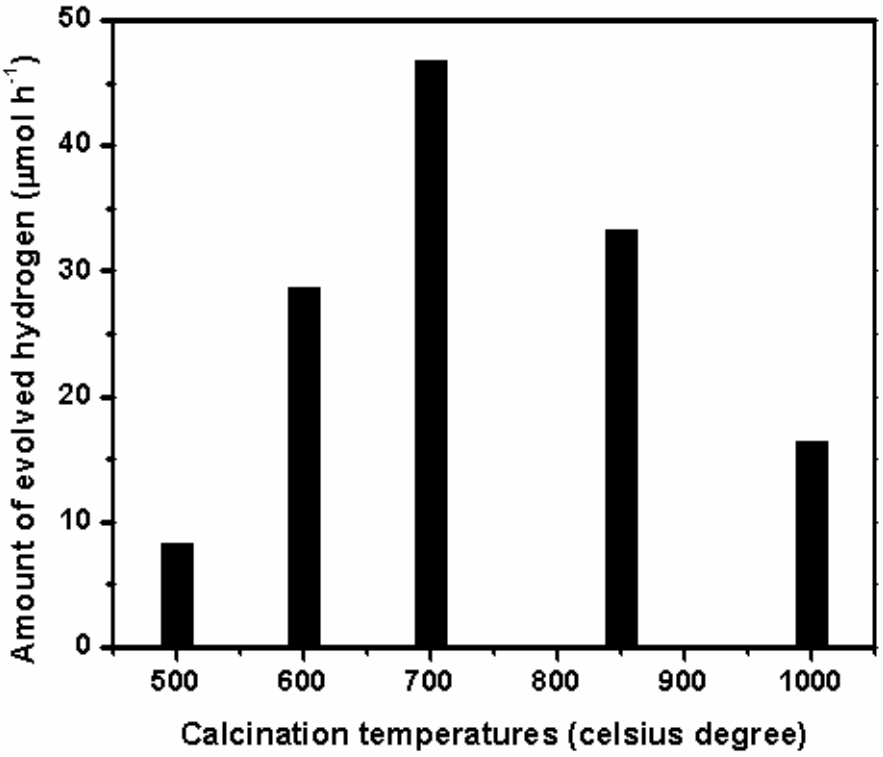

Figure 7-2 Rates of hydrogen evolution for Pt (0.5 wt. %)-SrTiO3: Rh (1 mol %) prepared by PC method and calcined at different temperatures. Catalyst weight: 50 mg.

Table 7-1 Integral breath volume-weighted crystallite size of $SrTiO_3$: Rh (1 mol %) prepared by the PC method and calcined at different temperatures.

Calcination Temperature /˚C	The integral breadth volume-weighted crystallite size (LVol-IB) / nm
500	**36**
600	**38**
700	**45**
850	**62**
1000	**96**

7.3.3 Dependence of photocatalytic activity of hydrogen evolution over Pt/$SrTiO_3$: Rh prepared by the PC method on different pH preparation conditions

To better understand the effect of pH during the synthesis, samples of $SrTiO_3$: Rh (1 mol %) prepared under different pH (pH = 1.5 (as synthesized), pH = 3, pH =5) were tested for

photocatalytic hydrogen evolution. Different amount of ammonium hydroxide solution (NH_3, 25 % by weight in water) was added into the polymeric solutions to achieve several pH values, such as pH = 3 and pH = 5, before the esterification process between citric acid (CA) and ethylene glycol (EG).

Figure 7-3 shows the photocatalytic activity for hydrogen production of 3 samples prepared under different pH conditions. Samples prepared at higher pH (pH= 3 and 5) had slightly higher photocatalytic activity for hydrogen evolution than that for sample prepared at lower pH (pH= 1.5).

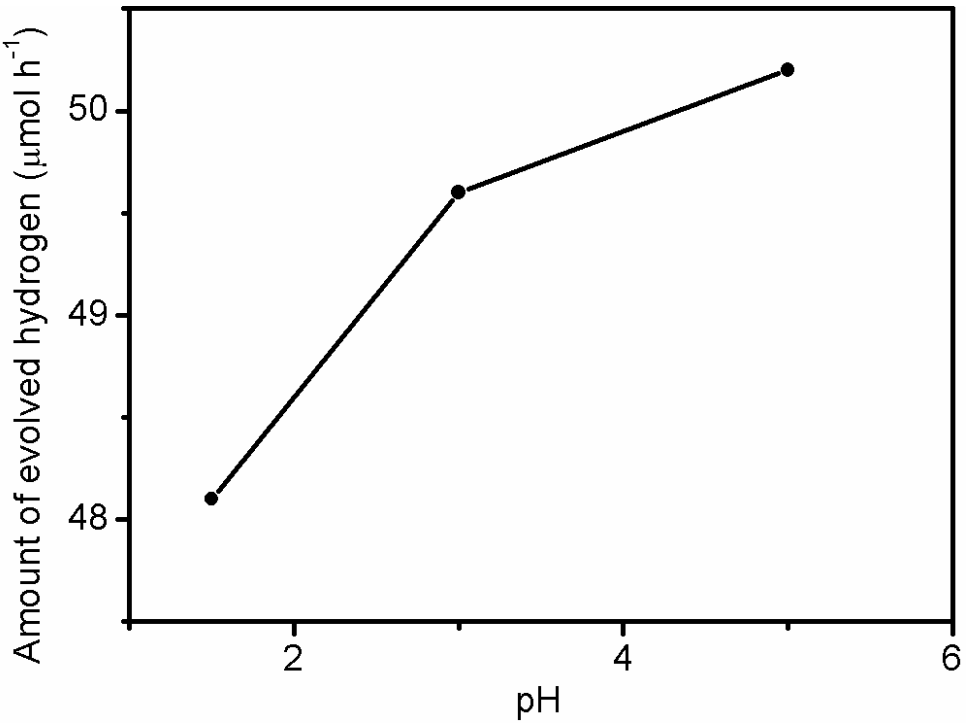

Figure 7-3 Rates of hydrogen evolution for Pt (0.5 wt. %)-$SrTiO_3$: Rh (1 mol %) prepared under different pH conditions. All the samples were loaded with Pt (0.5 wt. %) as co-catalyst. Catalyst weight: 50 mg.

In polymerizable complex process, two chemical reactions are involved. The first reaction is the chelation between complex cations and a hydroxycarboxylic acid. The second reaction is the polyesterification of excess hydroxycarboxylic acid with glycol. CA and EG are the most widely used hydroxycarboxylic acid and glycol. CA can form very stable chelating complexes with many metal ions, and EG can further stabilize the chelating complexes as it has two alcoholic hydroxyl functional groups (-OH). These function groups can form strong complexation

affinities to metal ions. During this process, pH can affect the formation of chelating complexes, through changing the stabilities of metal ions-CA complexes.

In our case, higher pH resulted in higher stability and homogeneity of Sr^{2+} and TiO^{2+}/RhO^{2+}, and also improved the homogeneity in the polyester precursor after the esterification. The higher homogeneity in the precursor solution promoted the formation of $SrTiO_3$: Rh with higher homogeneity. However, to have higher photocatalytic activity, homogeneity of the sample is just one of the many considerations. Other factors, such as surface reaction sites, electron mobility, photon absorption and electron-hole separation are also the dominants of the activity. As shown in Figure 7-3, even for the samples with better homogeneity (which were prepared at higher pH), the photocatalytic activities were still restricted. This phenomenon suggested that the homogeneity of the samples prepared by polymerizable complex method was high, even for the sample which was prepared without addition of NH_3. The homogeneity was no longer the pacing factors, other considerations, as discussed above, need to be reviewed for photocatalytic activity enhancement.

7.3.4 Dependence of photocatalytic activity of hydrogen evolution over Pt/$SrTiO_3$: Rh prepared by the SSR on different Rh doping concentration

The photocatalytic activities for hydrogen evolution on $SrTiO_3$: Rh with different Rh doping concentration prepared by SSR and hydrothermal methods are presented here. The Rh doping concentrations for these two methods were similar to the preparation conditions used for PC method. 0, 0.5, 0.7, 1, 2 and 5 mol % Rh doping concentrations were selected. The detailed procedure for SSR synthesis was presented in Chapter 6.2. Briefly, all the precursors were mixed thoroughly according to the designed stoichiometric ratios. The mixtures were subsequently underwent 10 hours heat treatment at the designated temperatures to allow efficient diffusion and phase formation. After different $SrTiO_3$: Rh samples with various Rh doping concentrations were prepared, 0.5 wt. % Pt was deposited on the samples as a co-catalyst for activity enhancement.

Figure 7-4 shows the photocatalytic activity in hydrogen evolution of 0.5 wt. % Pt/$SrTiO_3$: Rh (Rh = 0-5 mol %) prepared by the SSR method under visible light.

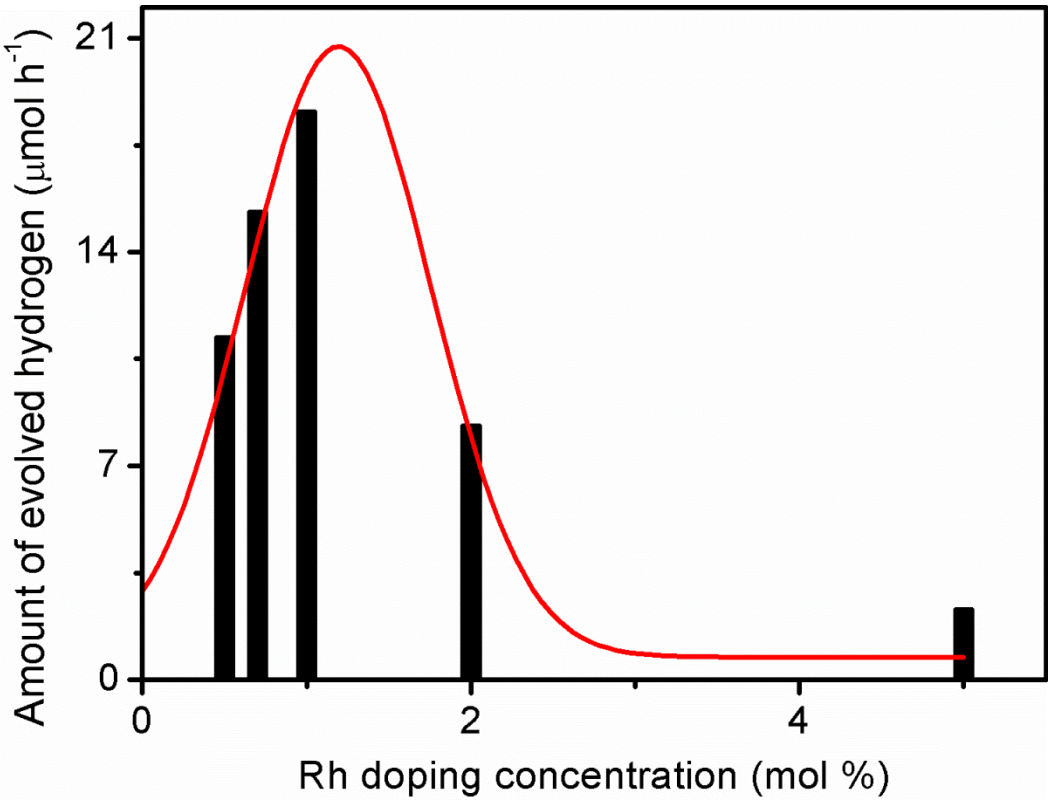

Figure 7-4 Rates of hydrogen evolution for $SrTiO_3$ synthesized by SSR method with different Rh doping concentrations. All the samples were loaded with Pt (0.5 wt. %) as co-catalyst. Catalyst weight: 50 mg.

As expected, without Rh doping, $SrTiO_3$ showed no activity. After doping with 0.5 mol Rh %, the sample was capable of producing of 11.2 $\mu molh^{-1}$ of H_2. The highest rate of H_2 evolution of 18.6 $\mu molh^{-1}$ was observed at 1 mol % Rh doping. The activity decreased dramatically at higher Rh doping concentrations. A comparison of photocatalytic activities of 1 mol % Rh doped and 5 mol % Rh doped $SrTiO_3$ samples prepared by SSR and PC methods is shown in Figure 7-5.

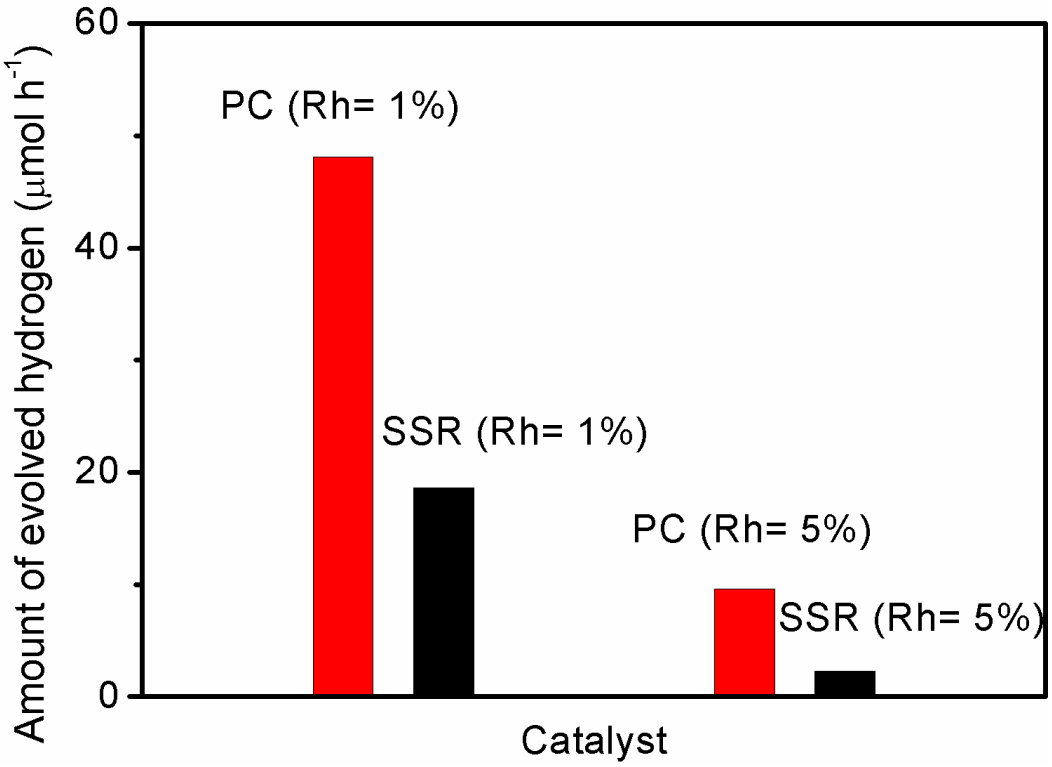

Figure 7-5 Activity comparison of $SrTiO_3$: Rh (Rh = 1 and 5 mol %) prepared by PC and SSR method. All the samples were loaded with Pt (0.5 wt. %) as co-catalyst. Catalyst weight: 50 mg.

As for the PC method, the sample with 1 mol % Rh doping concentration has 5 times activity of that with 5 mol % Rh doping concentration. When in SSR method case scenario, the activity of the sample with 1 mol % Rh overwhelmed that of the sample with 5 mol % Rh for approximately 10 times. The decrease of the activity for the two preparation methods could be different. The dominant reason in activity decrease at higher doping concentrations for the PC method is believed to be high defect density, as discussed in Chapter 3. However, for the SSR method, the reason might be a combination of high defect density and Rh species surface aggregation. In chapter 6, we carefully investigated $SrTiO_3$: Rh prepared by the SSR method by XPS for surface electronic states. We found abundant Rh species in the range of 1-10 nm to the surface of the sample. Whether these aggregated Rh species can provide intermediate energy levels remains a question, however, these aggregated Rh species can certainly compromised the interaction between photons and $SrTiO_3$ photocatalyst.

7.3.5 Dependence of photocatalytic activity of hydrogen evolution over Pt/$SrTiO_3$: Rh prepared by the SSR on different calcination temperatures

$SrTiO_3$: Rh (1 mol %) prepared by the SSR method is subjected calcination temperature investigation. The calcination temperatures chosen for the SSR method were 700, 800, 900, 1000, 1100 and 1200 ℃. The photocatalytic activity in hydrogen evolution is presented in Figure 7-7. When the calcination temperatures were 700 and 800 ℃, the sample only showed traceable photocatalytic activity in hydrogen evolution. There are two reasons to explain this phenomena : (1) The crystallinity is poor thus remains a lot of recombination centers, the efficiency of electron-hole separation is very low for effective photocatalytic hydrogen evolution; (2) The Rh dopant has not properly diffused into the lattice of $SrTiO_3$. The hydrogen evolution rate increased as calcination temperature increased, finally reached 18.6 $\mu mol \cdot h^{-1}$ when the calcination temperature was 1000 ℃. Further increased the calcination temperature resulted in a decrease in activity. This might be bigger particles were formed, which had smaller surface area and less surface active sites for photocatalytic hydrogen evolution.

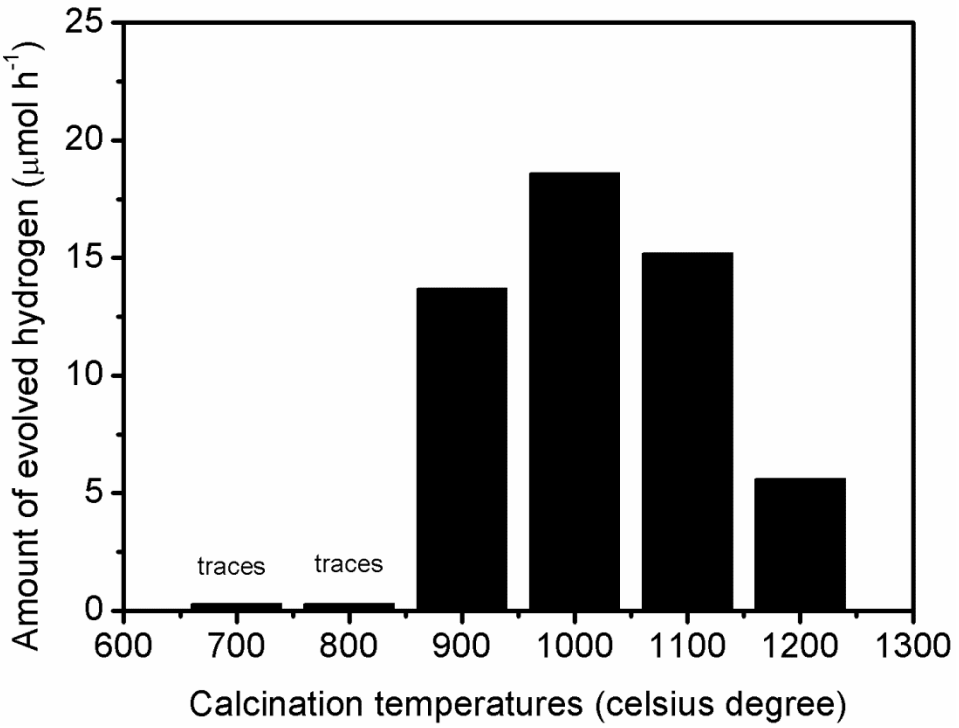

Figure 7-6 Rates of hydrogen evolution for Pt (0.5 wt. %)-SrTiO3: Rh (1 mol %) prepared by SSR method and calcined at different temperatures. Catalyst weight: 50 mg.

7.3.6 Photocatalyst stability for Pt (0.5 wt. %)-SrTiO3: Rh (1 mol %) prepared by the PC method

Whether a photocatalyst is stable or not is a very important question. Even with the existence of sacrificial reagents, some photocatalysts can experience significantly activity decrease, raise concerns in various perspectives, such as cost and commercialization potentials. Thus, stability examination, or deactivation testing, is very important for a photocatalyst.

Figure 7-8 shows the time course in photocatalytic hydrogen evoltion of $Pt/SrTiO_3$: Rh (1 mol %) prepared by the PC method. We found a nearly linear correlation between the irradiation time and H_2 evolution. Even after 3 cycles, the H_2 evolution rates were nearly identical, suggesting good catalyst stability under operating conditions.

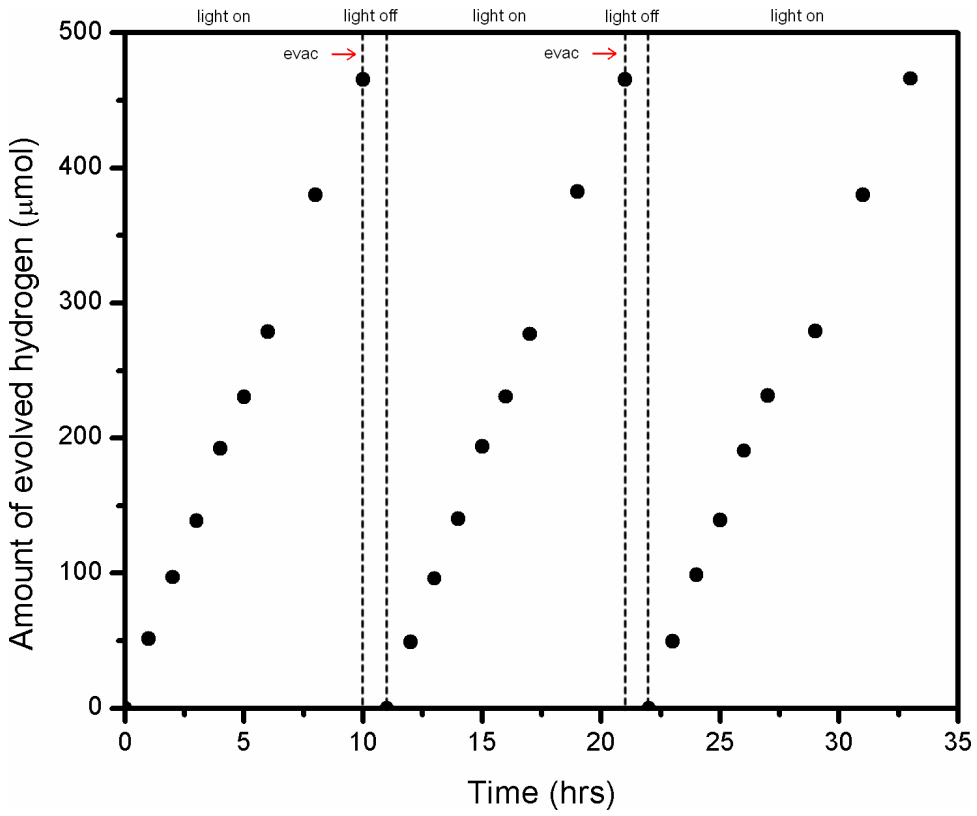

Figure 7-7 Time course of hydrogen production over Pt (0.5 wt. %) - $SrTiO_3$: Rh (1 mol %) with 3 times cycling. Catalyst weight: 50 mg.

The long term performance of this photocatalyst is shown in Figure 7-9 where the H_2 evolution activity is followed over the course of 60 hours. Only near the end of this period did we observe a deviation from a linear rate of H_2 production, again confirming the excellent

stability of this catalyst. In support of the stability measurements, the UV-Vis diffuse reflectance spectra of the sample showed no detectable changes before and after the photocatalytic reaction (not shown). This observation is different from those described in Kudo's work, where a decrease in UV-Vis signal intensity at 580 nm for SSR sample was detected after photocatalytic reaction conducted under similar conditions [2]. This might indicate that our sample prepared by PC method had a better stability as compared to Kudo's samples. The only difference between Kudo's and our sample testing was a much longer testing time (approximately 3 times longer), which make the stability argument for our samples even stronger.

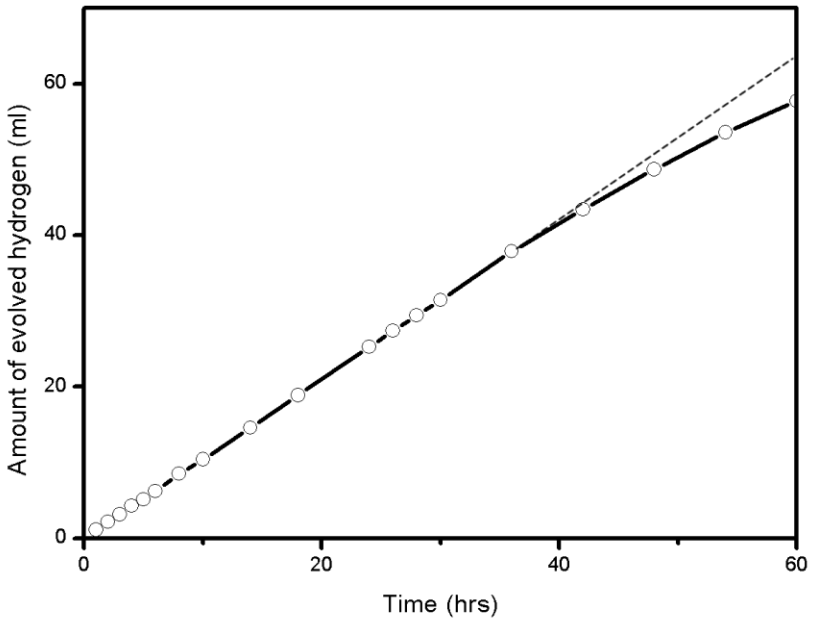

Figure 7-8 Long term stability testing of Pt (0.5 wt. %) - $SrTiO_3$: Rh (1 mol %). Catalyst weight: 50 mg.

7.3.7 Co-catalyst optimization

For photocatalytic activity in hydrogen evolution optimization, co-catalyst was also taken into account. Pt was considered as an effective co-catalyst for various photocatalyst systems. It was very common to use Pt as co-catalyst to further enhance the activities of the photocatalysts because Pt is an excellent hydrogen evolution promoter. However, if too many Pt particles are loaded on the surface of a photocatalyst, Pt can block the light, weaken the interaction between the light and the photocatalyst, and thus decrease the photocatalytic activity. This process is often

called surface shield effect. The optimum Pt loading amount was varied based on different reports, sometimes even seemed contradictory. In this research, different Pt loadings were applied onto $SrTiO_3$: Rh for photocatalytic activity in hydrogen evolution comparison. Pt loadings of 0.1, 0.25, 0.5, 0.75, 1 and 2 wt. % were selected and subsequently loaded onto the photocatalysts through photodeposition. Detailed preparation information for co-catalyst loading can be referred in Chapter 6.2. Figure 7-10 shows the hydrogen production rates of the photocatalysts with different Pt co-catalyst loadings. Among various loadings, 0.5 wt. % exhibited the best activity. The reason might be this loading achieved a balance between creating enough activation sites for hydrogen evolution and minimizing the surface shield effect [3]. Higher Pt loadings resulted in enhanced surface shield effects which attributed to a falling in hydrogen evolution efficiency.

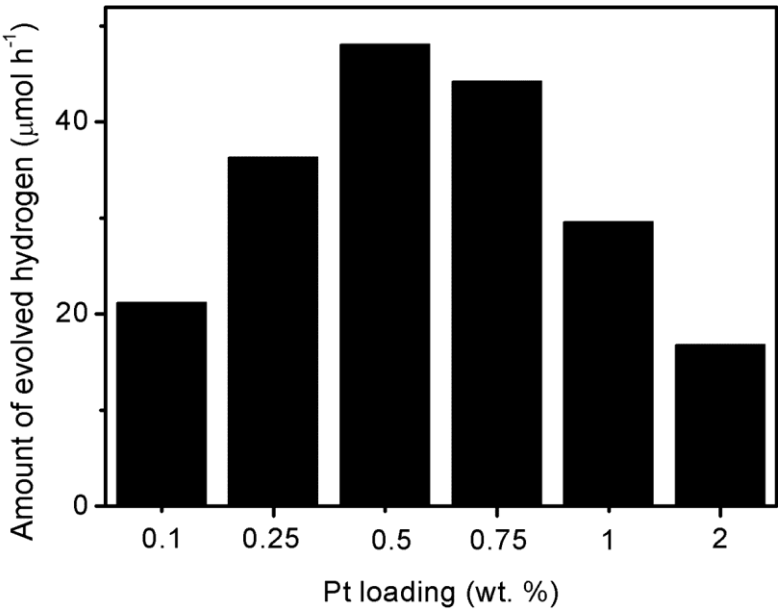

Figure 7-9 Rates of hydrogen evolution for Pt -SrTiO3: Rh (1 mol %) prepared by PC method with different Pt loading. Catalyst weight: 50 mg.

Some reports showed that Pt as a co-catalyst not only can promote hydrogen production reaction, but also serves a catalyst for back reaction. To investigate the role of co-catalyst with our photocatalyst, other co-catalysts (Ru, Au, Pd) were loaded onto $SrTiO_3$: Rh for photocatalytic hydrogen evolution testing and stability testing. 0.5 wt. % of different co-catalysts were loaded onto the samples through photodeposition. Figure 7-11 shows the photocatalytic

hydrogen evolution rates of $SrTiO_3$: Rh prepared by the PC method loaded with various co-catalysts over 60 hours. Pt still presented the highest activity among all the tested co-catalysts.

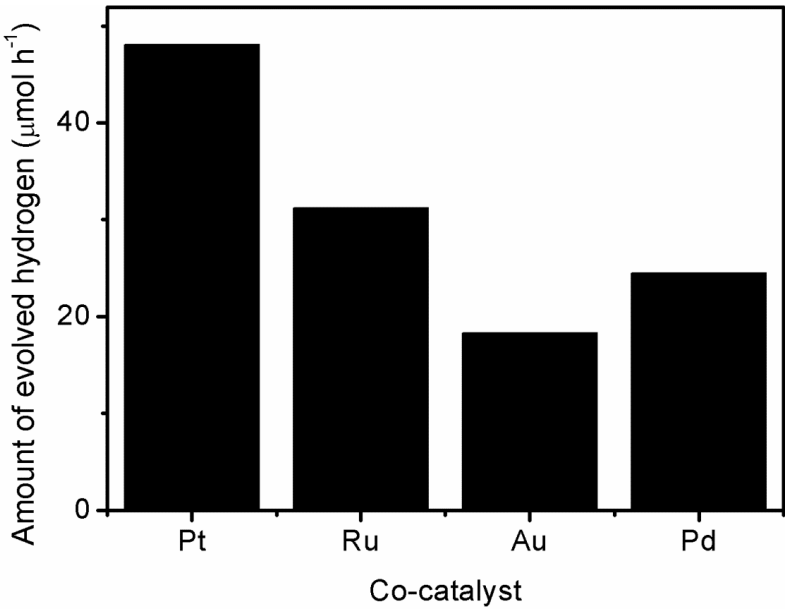

Figure 7-10 Rates of $SrTiO_3$: Rh prepared by the PC method loaded with various co-catalysts. Catalyst weight: 50 mg.

7.3.8 Comparison of photocatalytic activity of hydrogen evolution over Pt/$SrTiO_3$: Rh (1 mol %) prepared by the SSR, hydrothermal and PC method

We compared three photocatalysts prepared by the three different methods used in this work (PC, SSR, hydrothermal). According to the results presented in Figure 7-12, the $SrTiO_3$: Rh (1 mol %) with 0.5 wt. % Pt as co-catalyst prepared by the PC method had the highest hydrogen evolution activity. The activities of the samples without Pt as co-catalyst prepared by the different methods were also showed in Figure 7-13. Even without Pt as co-catalyst, $SrTiO_3$: Rh samples prepared by all three methods were still able to evolve hydrogen under visible light, however, with much lower hydrogen production rates, as shown in Figure 7-13. Among these three methods, the PC method still showed merit over the other two.

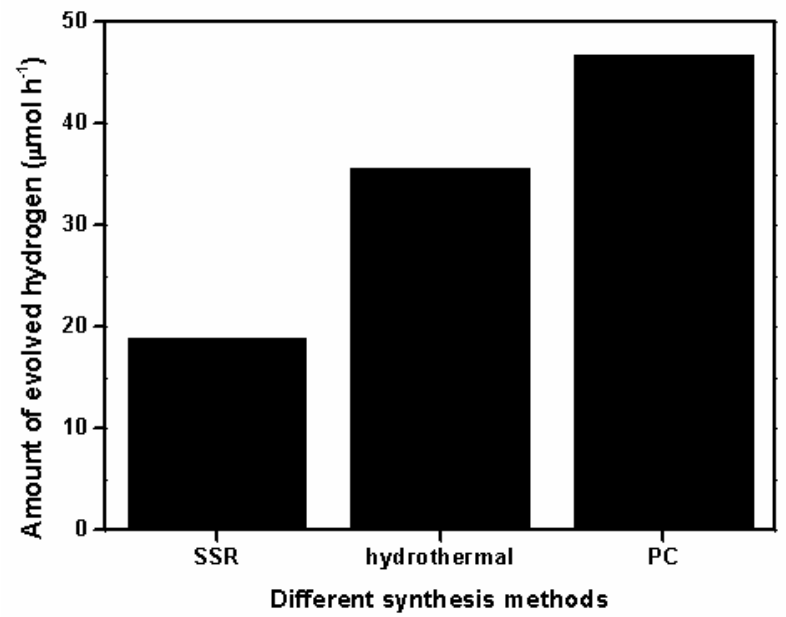

Figure 7-11 Rates of hydrogen evolution of Pt (0.5 wt. %) - $SrTiO_3$: Rh (1 mol %) prepared by different methods. Catalyst weight: 50 mg.

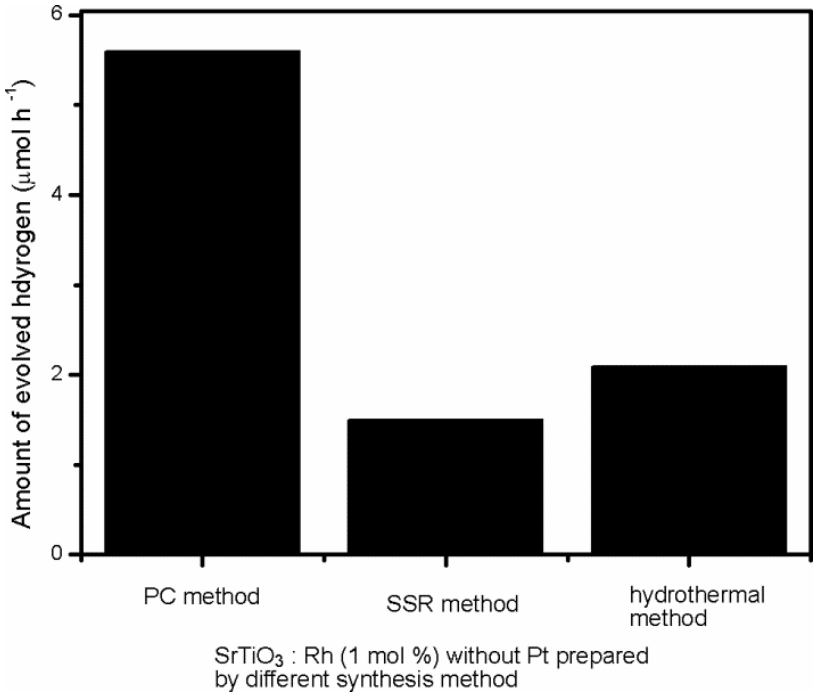

Figure 7-12 Hydrogen evolution rate of SrTiO3: Rh (1 mol %) without Pt as co-catalyst prepared by different synthesis methods. Catalyst weight: 50 mg.

Several factors are likely to contribute to the higher performance of the PC prepared samples. Firstly, the crystallite sizes of the PC prepared $SrTiO_3$: Rh samples were the smallest among the

three samples as indicated by XRD and TEM measurements. As the particle size decreases, the reactive surface area increases, which can lead to a higher reaction rate. Secondly, a better uniformity of Rh doping within the lattice of PC sample, as compared to that of SSR sample, may also play a role in improving activity. Based on the XPS results described earlier, the Rh^{4+} cations are located predominantly within $SrTiO_3$ lattice for the PC prepared samples. By contrast, the XPS results for the SSR samples showed that Rh^{4+} cations are located both in the lattice and on the surface, with the latter showing up as metallic Rh^0 after high temperature annealing. The lattice distribution of Rh^{4+} cations is likely to be crucial for the creation of spatially uniform donor states in the bandgap, from which visible light activity is derived. Overall, our results suggest that the PC synthesis method yields a superior Rh-doped $SrTiO_3$ photocatalyst due to the formation of smaller crystallites (higher surface area) and a more complete incorporation of the Rh^{4+} cations into the bulk lattice.

References

[1] H. Kotani, R. Hanazaki, K. Ohkubo, Y. Yamada, S. Fukuzumi, Size and shape dependent activity of metal nanoparticles as hydrogen evolution catalysts: mechanistic insights into photocatalytic hydrogen evolution, Chemistry-A European Journal, 17 (2011) 2777-2785.
[2] R. Konta, T. Ishii, H. Kato, A. Kudo, Photocatalytic activities of noble metal ion doped $SrTiO_3$ under visible light irradiation, Journal of Physical Chemistry B, 108 (2004) 8992-8995.
[3] B. Sun, A.V. Vorontsov, P.G. Smirniotis, Role of platinum deposited on TiO_2 in phenol photocatalytic oxidation, Langmuir, 19 (2003) 3151-3156.

Chapter 8

Photocatalytic Hydrogen Evolution for Sub-nanometer Noble Metal Loaded CdS

8.1 Chapter introduction

It is believed that co-catalysts can lower activation energy for H_2 or O_2 evolution and serve as the active sites for H_2 or O_2 generation [1]. Many co-catalyst were found be efficient to promote photocatalytic reactions including metal oxides such as NiO, RuO_2 [2]; noble metals, such as Pt, Ru, Rh and Pd [3-6]; metal sulfides, such as MoS_2 [7] WS_2 [8] as well as core-shell structures, such as Rh/Cr_2O_3 [9]. However, various issues have also been reported regarding these co-catalysts. For example, there are concerns about metal oxide co-catalysts long term stability [1]. Noble metals as Pt, Pd, and Rh are excellent promoters for H_2 evolution, however, they can also facilitate water formation reaction (back reaction) from H_2 and O_2 [1, 10], thus reducing the beneficial effects of their deposition. In contrast to the above mentioned co-catalysts, semiconductor surface modification with gold nanoparticles of approximately 20 nm in size has been shown to lead to a comparable (to Pt) activity for H_2 production with much lower rates of back reaction [11]. Utilizing even smaller Au particles can potentially bring some additional benefits. For example, there are reports indicating that Au nanoparticles loaded on TiO_2 [12, 13] and perovskite titanate ($K_2La_2Ti_3O_{10}$) [14] can be promising photocatalysts for water splitting reactions. These reports were focused on the average Au particle size above 3 nm. However, exploring the sub-nm range of Au co-catalysts for water splitting has never been attempted before and photocatalytic properties of such materials are currently unknown.

8.2 Experimental conditions

8.2.1 Catalyst preparation

8.2.1.1 Preparation of GaP

Gallium phosphide (GaP, ≥99.99%) was obtained from Aldrich. 1 g of GaP powder agglomerate was ball milled for 15 mins at 2000 rpm. After milling the powder was collected and used without further treatment.

8.2.1.2 Preparation of GaP/TiO_2

GaP/TiO_2 photocatalysts were synthesized by the researchers from University of Cambridge, UK. Different GaP loading amount, 0.1, 0.2, 0.3, 0.5, 1, 2 and 3 wt. % GaP were coupled with TiO_2. The samples were tested for photocatalytic activity without further treatment.

8.2.1.3 Preparation of CdS

Sodium sulfide (Na_2S, ≥98.0%) and Cadmium acetate dihydrate ($Cd(CH_3COO)_2•2H_2O$, ≥98%) were obtained from Alfa Aesar and Aldrich, respectively, and used without further treatment.

CdS nanoparticles were prepared by the following method. 10 g of Na_2S and $Cd(CH_3COO)_2•2H_2O$ were dissolved in 100 ml de-ionized water in two separate beakers. A solution of sodium sulfide (Na_2S) was added to cadmium acetate solution ($Cd(CH_3COO)_2•2H_2O$) by using a syringe pump (the injection speed of 0.2 ml/min) under vigorous stirring. The molar ratios were 1:1 and the mixture was stirred for 24 hours. Then the resulting sample was centrifuged, washed with deionized water for 3 times, dried at 60 ˚C overnight and calcined at 400 ˚C for 45 minutes.

8.2.1.4 Preparation of sub-nm Au NPs / CdS

Sub-nm gold particles synthesis was based on the following approach. $Au(PPh_3)Cl$ was dissolved in $CHCl_3$ to reach a final concentration of 10^{-3} mol/L. About 10^{-3} mol/L $P(Ph)_2(CH_2)_4P(Ph)_2$ was subsequently added to the mixture to achieve the target cluster size. Finally, $5 • 10^{-3}$ mol/L of the reducing agent (aborane-tert-butylamine complex) was added under continuous stirring for 24 hours at room temperature.

To modify CdS surface with nanoparticles, about 200 mg of CdS was added to 20 ml of dichloromethane, followed by addition of Au NPs precursors. The gold deposition procedure on CdS powders was achieved by varying the ratios of CdS and Au NPs precursors developed in the previous step. The mixture was stirred overnight, followed by thermal activation (150℃, 2h) in vacuo. The final powder was then washed with acetone.

8.2.1.5 Preparation of sub-nm Pt NPs / CdS

Sub-nm Pt NPs were synthesized by a modified inverse micelle encapsulation method to achieve particle size with high uniformity. Briefly, diblock copolymers Poly(styrene)-block-poly-(2vinylpyridine) were dissolved in toluene. Toluene is a non-polar solvent which facilitates the formation of spherical nanocages (reverse micelles). By modifying metal-salt/polymer-head (P2VP) ratio, the particle size of Pt NPs can be adjusted. $H_2PtCl_6·6H_2O$ was used as the metal-salt and the ratio of $H_2PtCl_6·6H_2O$ to P2VP was selected as 0.1 to attain a sub-nm size of the Pt NPs. After the complete dissolution of P2VP and the metal-salt, the solution was mix with CdS and stir dried overnight for NPs deposition. Samples with different sub-nm Pt NPs loading

amount (0.5, 0.7, 1, 2, 5 wt. %) were prepared. The samples were subjected to heat at 400 ℃ for 24 hours for encapsulating polymer removal, and subsequently reduced in H2 at 400 ℃ for 2 hours. 5 wt. % sub-nm Pt NPs deposited on Al_2O_3 was prepared for TEM characterization.

8.2.1.6 Preparation of regular size noble metals (Au, Pt, Ru, Pd, Rh)/CdS

Different noble metals, including Au, Pt, Ru, Pd and Rh, were loaded on CdS by photo-deposition method using $HAuCl_4$, $H_2PtCl_6 \bullet 6H_2O$, $RuCl_3$, $PdCl_2$ and $RhCl_3$ aqueous solutions, respectively.

8.2.2 Characterization

UV-Vis optical absorption spectrum of unsupported Au clusters was obtained by Ultraviolet-visible spectroscopy (Thermo Evolution 3000). Au cluster was suspended in a reducing agent (aborane-tert-butylamine complex) and transferred to a quartz cubicle. The sample was scanned by a UV-Vis spectrometer from 200 - 800 nm with a step size of 2 nm/s.

Sub-nm Au/CdS samples and sub-nm Pt/Al_2O_3 were characterized by a Scanning Transmission Electron Microscopy (Hitachi HD2700C) with a probe aberration-corrector. Specimen for STEM was prepared by suspending the sample in ethanol. Then a droplet of the as prepared suspension solution was transferred to a copper grid coated with an amorphous carbon support and ready for STEM observation. We have used an electron probe of 1.3 Å at a semi-collection angle between 114 and 608 mrad. Transmission Electron Microscopy (TEM) images were obtained using a JEOL2100F (200 kV) microscope.

8.2.3 Photocatalytic testing for hydrogen production

Photocatalytic testing was carried out in a customized reactor connected to a closed gas circulation and evacuation system. 100 mg of catalyst was suspended in 200ml of aqueous solution containing 0.25 M Na_2S and 0.35 M Na_2SO_3, which acted as sacrificial reagent. The suspension was put in the dark and purged with argon while being stirred by magnetic stir bar for 30 min, which was followed by degassing procedure. 40 Torr argon was introduced into the system as carrier gas. Then the suspension was irradiated by a 300W Xe lamp (Newport, Model 66984) equipped with an optical cutoff filter (λ>420 nm, L42, Hoya) to eliminate ultraviolet light and a 10 cm water filter (λ<800 nm) to eliminate IR. The amount of H2 produced was analyzed

using an online gas chromatography unit (Agilent 7890A) equipped with a thermal conductivity detector and a 5Å molecular sieve column.

8.3 Results

8.3.1 Semiconductor photocatalyst selection for photocatalytic hydrogen production

As co-catalyst needs to be loaded on a semiconductor for photocatalytic reaction test, it is important to select a proper semiconductor photocatalyst for co-catalyst investigation. The photocatalyst need to meet several criteria, such as suitable bandgap and bandgap positions, chemical and mechanical stability, easy preparation and low cost. CdS and GaP have suitable bandgap to be activated by visible light while their reduction potentials are more negative than hydrogen formation potential. Therefore these semiconductors are theoretically suitable for sacrificial photocatalytic hydrogen production. Both CdS and GaP were investigated for their photocatalytic activity. Figure 8-1 shows the time course of hydrogen production on CdS and GaP with the existence of electron donors.

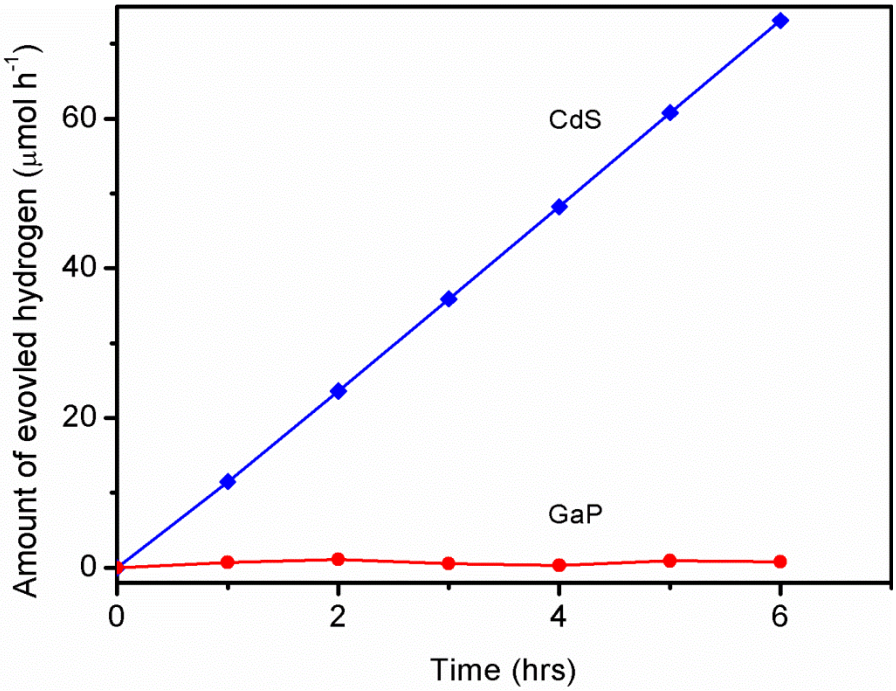

Figure 8-1 Time course of hydrogen production on CdS and GaP. (Catalyst weight 100 mg. 0.25 M Na_2S and 0.35 M Na_2SO_3 was used as electron donors for CdS, 0.5 M methanol was used as electron donors for GaP).

CdS showed very linear hydrogen production rate with the existence of electron donors. The average hydrogen production rate over 6 hours was about 12μmol•h^{-1}. GaP showed very poor photocatalytic activity even with the existence of sacrificial reagents. It was very challenging to quantify the rate of hydrogen production on GaP. The traceable fluctuation of the activity might come from instrument error or contaminations.

Samples of different loading amount of GaP coupled with TiO2 were also tested for photocatalytic hydrogen evolution. Figure 8-2 shows the photocatalytic hydrogen evolution rates of the samples loaded with different amount of GaP.

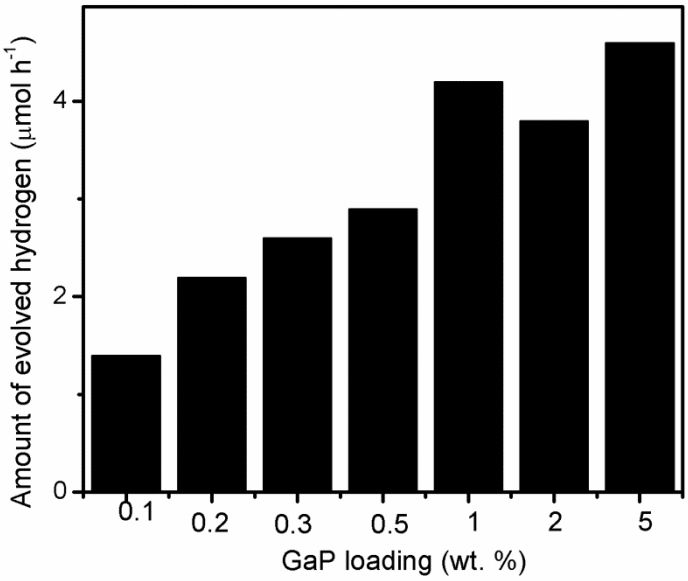

Figure 8-2 Rates of photocatalytic hydrogen production of TiO_2 loaded with different amounts of GaP. (Catalyst weight 100 mg. 0.5 M methanol was used as electron donors).

Photocatalytic hydrogen evolution activities of TiO_2 loaded with different amount of GaP did not present a clear statistical trend, nor were the activities comparable with CdS for photocatalytic hydrogen production. Although it appeared that the photocatalytic activities were enhanced when different amounts of GaP coupled with TiO_2, more optimization and investigations are still needed. It is necessary to choose a simple yet promising photocatalyst for noble metal co-catalyst investigation. Therefore, in this chapter, CdS was selected as the semiconductor photocatalyst for all the co-catalyst investigations.

8.3.2 Sub-nm Au NP particle size and its optical and electronic characteristics

In order to understand the role of Au particle size in photocatalytic activity, we have conducted a detailed characterization of both supported and unsupported Au samples using STEM, TEM and UV-Vis spectroscopy. Figure 8-3 shows a STEM image of unsupported Au clusters. The as-synthesized Au clusters have a relatively homogenous distribution. The insert of Figure 8-3 gives a close look of a Au cluster.

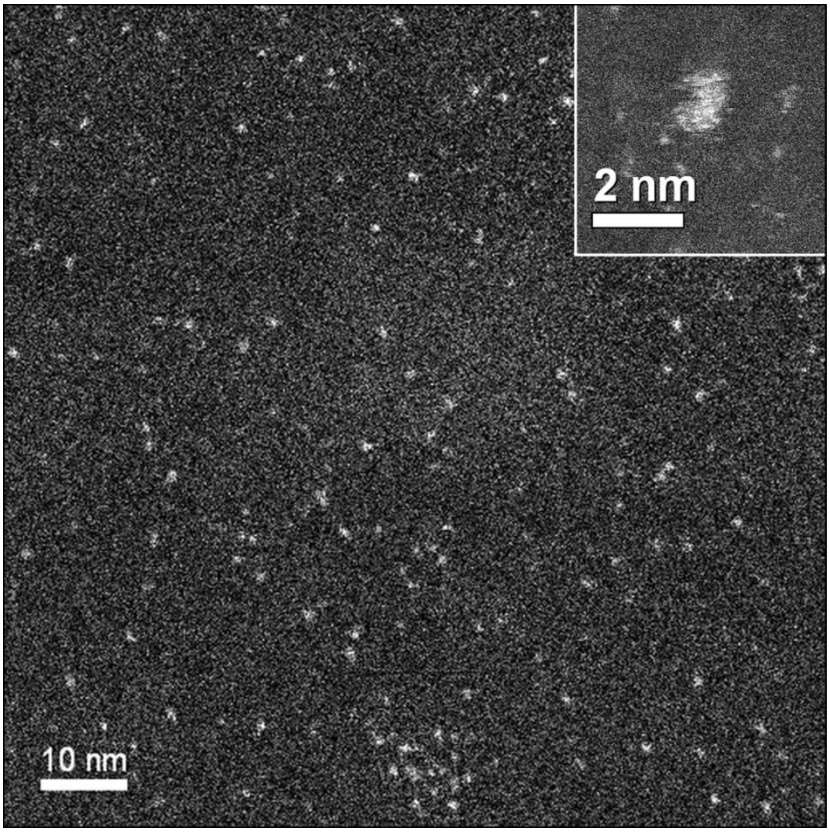

Figure 8-3 STEM image of unsupported Au clusters. Insert shows higher resolution image of sub-nm Au cluster.

The size distribution of unsupported Au clusters is shown in Figure 8-4.

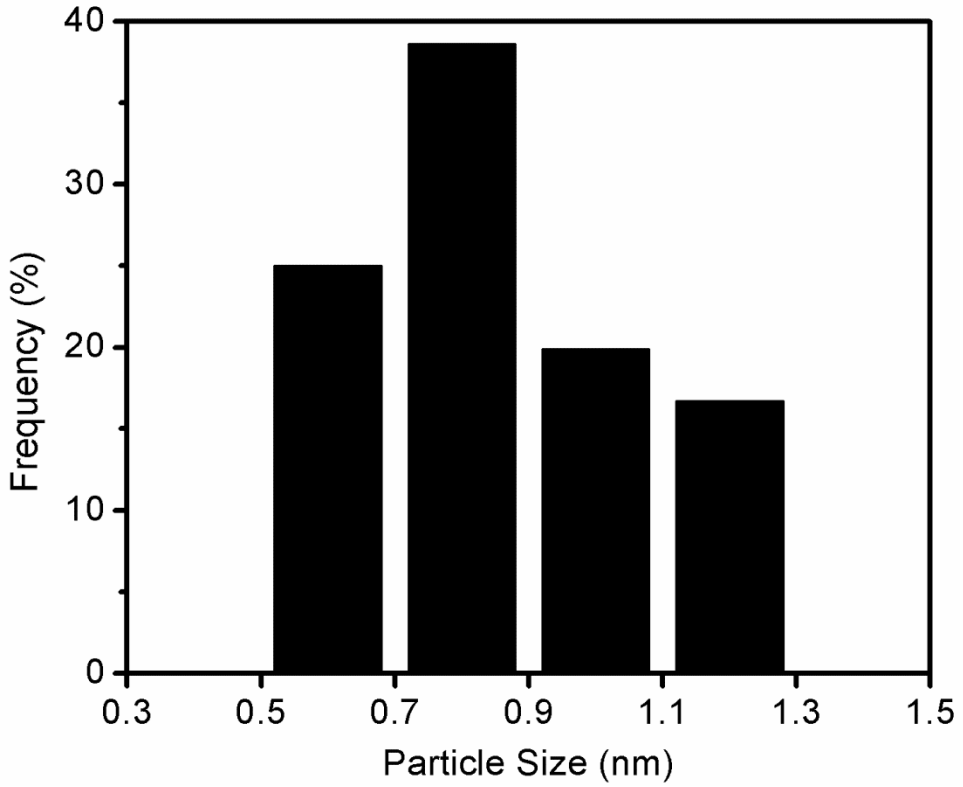

Figure 8-4 Particle size distribution of unsupported sub-nm Au NPs with average Au size of about 0.8 ± 0.1 nm.

Figure 8-4 and the previous work on unsupported clusters [15] indicated that the average particle size of unsupported Au was about 0.8 ± 0.1 nm as determined by STEM, which can be attributed to abundance of Au11 – Au13 clusters [16, 17]. We also found that the precursor solution contained both single atoms and clusters up to 11-13 gold atoms in size, as determined by Matrix-Assisted Laser Desorption/Ionization-Time of Flight Mass Spectrometer (MALDI-TOF) measurements [15]. A detailed analysis of UV-Vis data of unsupported Au clusters showed a prominent peak at 410 nm. The computed optical spectrum for mixed ligand protected Au^{11+} and Au^{9+} clusters, with two dominating peaks at 420 nm and 300 nm, in reasonable agreement with UV-Vis data.

A close inspection of the corresponding excitations show significant Au 5d → 6sp transition characters and metal-to-ligand charge transfer transition characters, respectively. DFT calculation was introduced in assistance of Au electronic structure understanding. All the work of computational calculations of noble metal co-catalysts were a result of the cooperation with Dr. Yan Li from Brookhaven National Laboratory. The DFT calculations of unsupported Au

clusters indicated that there is a substantial difference in both shape and electronic properties between charged and neutral bare Au clusters as well as between bare and ligand-protected ones, which might affect the shape of supported co-catalysts. For example, the minimum energy structure of the bare Au^{11-} cluster is planar with a computed gap of 1.0 eV, while that of Au^{11+} is three-dimensional with a DFT gap of 1.7 eV.

Additionally the density of states of deprotected Au clusters indicate the appearance of HOMO-LUMO gap of about 2 eV (Au^{11+}), as shown in Figure 8-5, which can affect the charge transfer from photoexcited CdS to Au. All these factors might need to be taken into account to explain the extraordinary activity of sub-nm Au clusters discovered in our work.

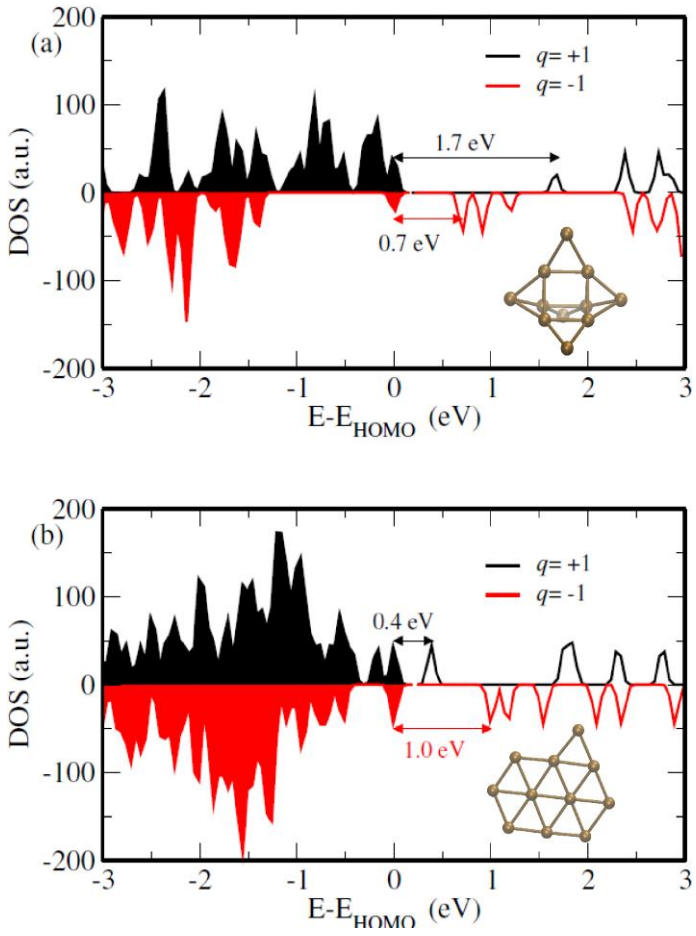

Figure 8-5 Computed density of states (DOS) of bare Au_{11} clusters. (a), Au_{11}^{+} (3D, gap = 1.7 eV). (b), Au_{11}^{-} (2D, gap = 1.0 eV). For comparison, DOS of the same clusters but with opposite charges, i.e. 3D Au_{11}^{-} (gap = 0.7 eV) and 2D Au_{11}^{+} (gap = 0.4 eV), are also presented.

Figure 8-6 shows the STEM-high angle annular dark field (HAADF) image of 5 wt. % Au/CdS. Figure 8-7 confirms that the average particle size of the samples was around 0.95 ± 0.1 nm. The Au particle size distribution in the sample indicated that only minor agglomeration of Au clusters has occurred after their deposition and de-protection as compared to unsupported clusters. Moreover, in order to explore particle stabilities, we subjected our samples to different thermal activation temperatures ranging from 130 ℃ to 180 ℃. However, we did not observe any detectable changes in terms of particle sizes.

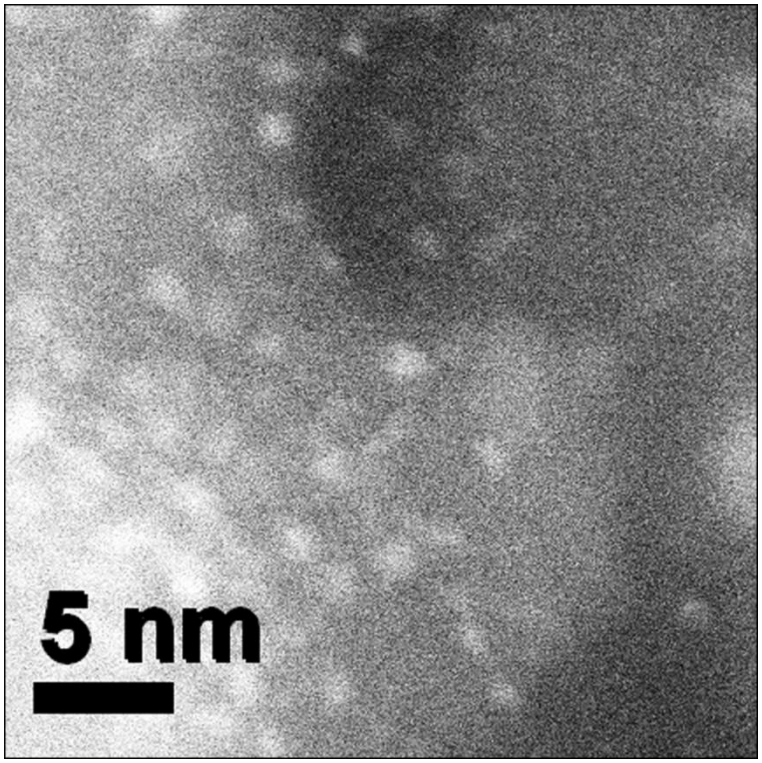

Figure 8-6 Scanning transmission electron micrograph of 5 wt. % sub-nm Au NPs loaded on CdS.

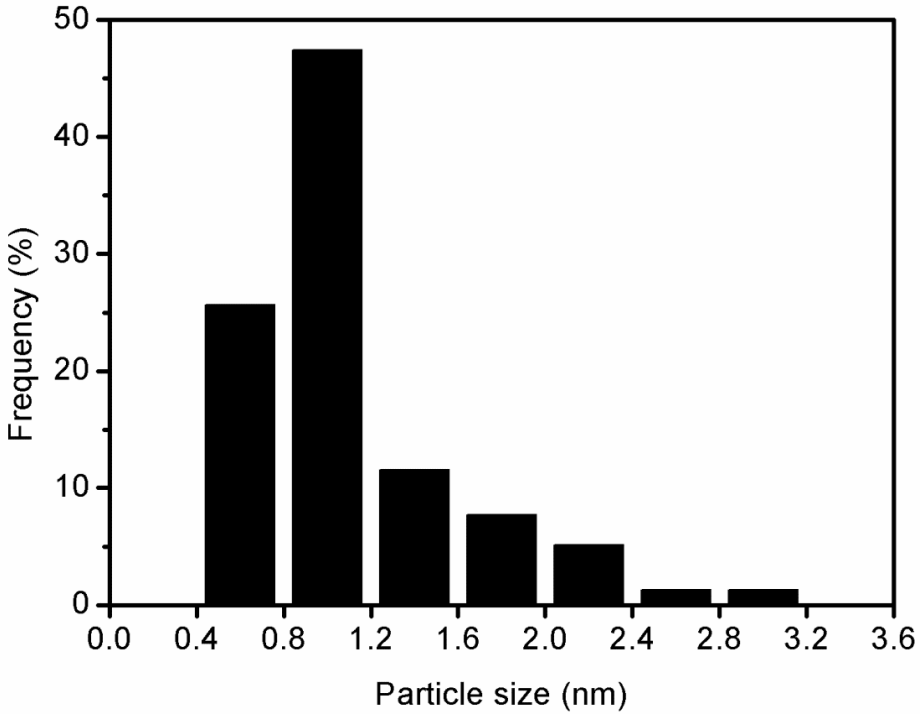

Figure 8-7 Particle size distribution of sub-nm Au loaded on CdS with average Au size of about 0.95 ± 0.1 nm (particle size distribution is based on several STEM images).

8.3.3 Sub-nm Pt NP particle size

Sub-nm Pt NPs were deposited on Al_2O_3 and characterized by TEM. Figure 8-8 shows the TEM image of 5 wt. % sub-nm Pt/Al_2O_3.

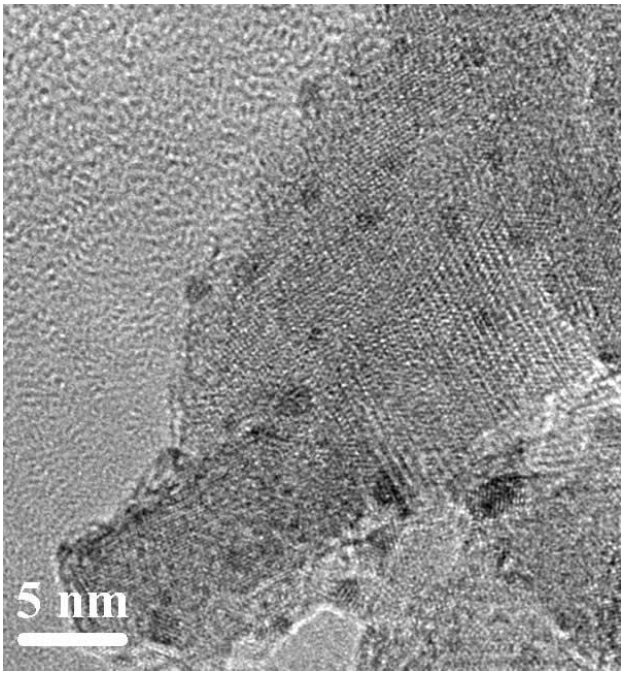

Figure 8-8 Transmission electron micrograph of 5 wt. % sub-nm Pt loaded on Al_2O_3.

The as prepared sample has a narrow particle size distribution of 0.8-1.2 nm. This particle size distribution (Figure 8-9) indicates that Pt NPs were uniformly dispersed on the support and the copolymer removal did not induce significant agglomeration.

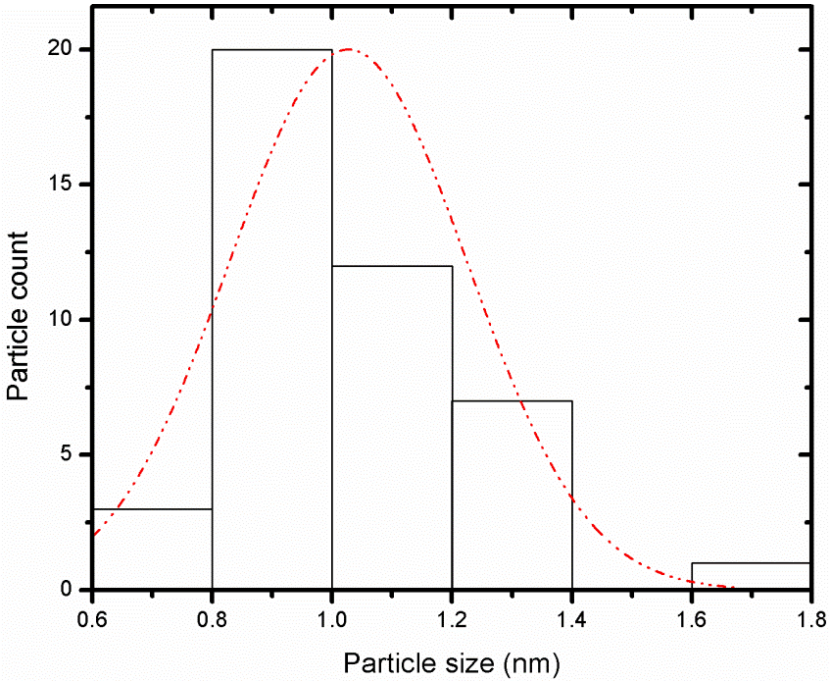

Figure 8-9 Size distribution of sub-nm Pt NPs deposited on Al_2O_3.

8.3.4 Photocatalytic activity of sub-nm Au/CdS for hydrogen evolution

Figure 8-10 shows the rates of H_2 evolution on sub-nm Au/CdS with different amounts of Au loadings. The results indicated that sub-nm gold particles can provide an enormous improvement in photocatalytic H_2 production under visible light. For comparison, the rate of H_2 evolution on pure CdS is also plotted. As expected, unmodified CdS photocatalyst exhibited very low photocatalytic activity for H_2 evolution (ca. 12 μmmol•h^{-1}), which is consistent with the previously published reports [4, 7]. In contrast to unsupported CdS, sub-nm Au modified photocatalysts exhibited a remarkably improved activity even at very low gold loadings. The most active catalyst was 1 wt. % Au modified CdS, which showed about 35 times improvement in H_2 production rate (ca. 404 μmol•h^{-1}) as compared to that of unmodified CdS. We have repeated the experiment 3 times to confirm this very significant result (as indicated by the error bars in Figure 8-10). A further increase in Au loading resulted in decrease in photocatalytic activity, probably due to reduction of illuminated area of CdS (due to Au coverage) and potential agglomeration of sub-nm Au clusters.

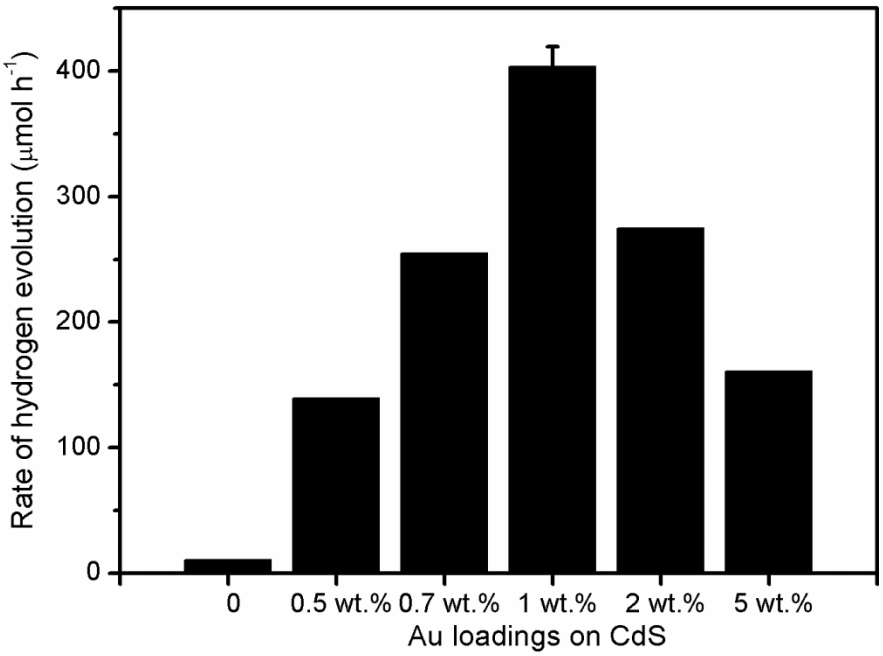

Figure 8-10 Rates of H_2 evolution on sub-nm Au/CdS with different amounts of Au loadings.

Figure 8-11 shows H_2 evolution as a function of time for the most active sub-nm Au/CdS sample, where we cycled this catalyst 3 times to determine its stability and reactivity. The

sample showed almost linear concentration dependence for all 3 cycles. Even after 18 hours of reaction there was no significant deactivation of the catalyst. The robustness in catalytic performance can be attributed to stability of both sub-nm Au clusters and CdS. Under normal conditions, CdS tends to undergo photo-corrosion [18], however, the presence of sacrificial reagents (Na_2SO_3 and Na_2S) can significantly slow this process [19].

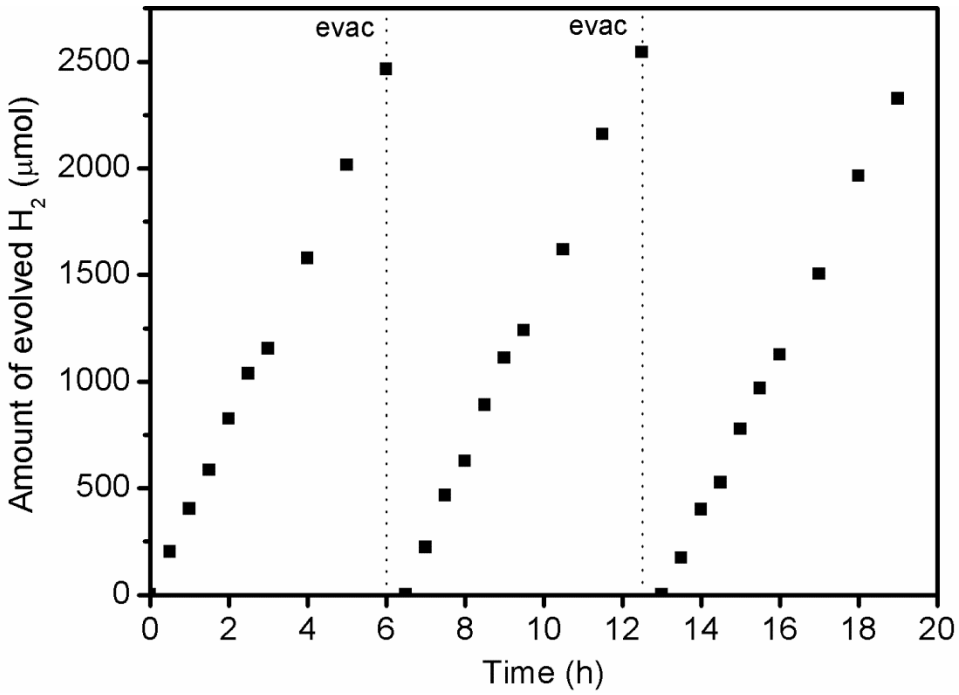

Figure 8-11 Stability test for 1 wt. % sub-nm Au/CdS.

8.3.5 Photocatalytic activity of different sizes Au/CdS for hydrogen evolution

One important question is whether the activity of small Au clusters is different from that of larger particles. In order to address this question we subjected the most active sample (1 wt. % sub-nm Au/CdS) to heat treatment, which resulted in Au agglomeration as indicated by our STEM results. Figure 8-12(a) shows the STEM image of this sample after the heat treatment. The average Au particle size of heat-treated catalyst was about 9.0 ± 0.3 nm, as shown in Figure 8-11(b).

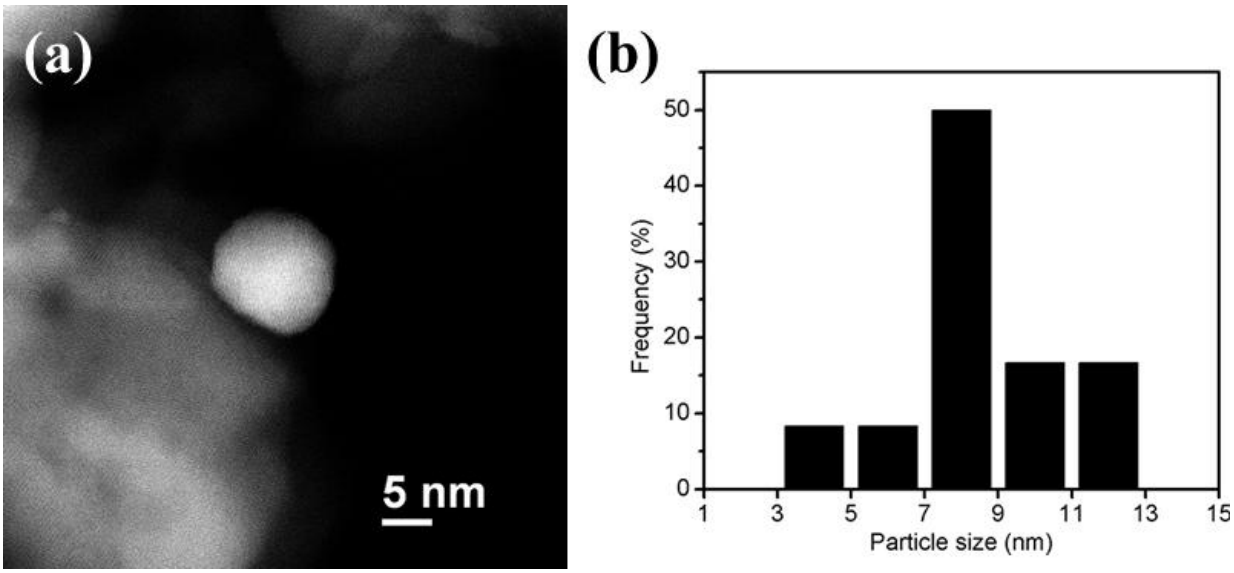

Figure 8-12 STEM image and particle size distribution of large size Au/CdS sample. (a) STEM image showing 9 nm Au loaded on CdS. (b) Particle size distribution of 9 nm Au nanoparticles, average size = 9.0 ± 0.3 nm (particle size distribution is based on several STEM images).

In order to gain even better understanding of the size dependent catalytic activity, we used photo-deposition method to produce intermediate size Au particles. Figure 8-13(a) shows the TEM image of Au particles prepared by photo-deposition method, where the average Au particle size achieved by this method was 3.0 ± 0.1 nm (Figure 8-13(b)).

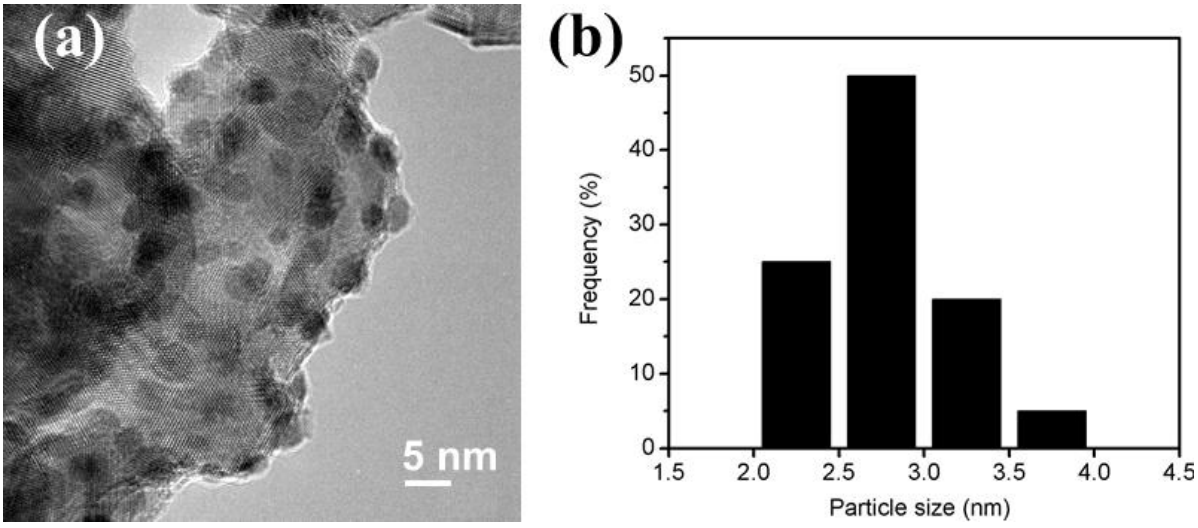

Figure 8-13 STEM image and particle size distribution of intermediate size Au/CdS sample. (a) TEM image showing 3 nm Au loaded on CdS. (b) Particle size distribution of 3 nm Au

nanoparticles, average size = 3.0 ± 0.1 nm (particle size distribution is based on several TEM images).

Figure 8-14 shows activity of CdS samples modified with Au nanoparticles of difference sizes.

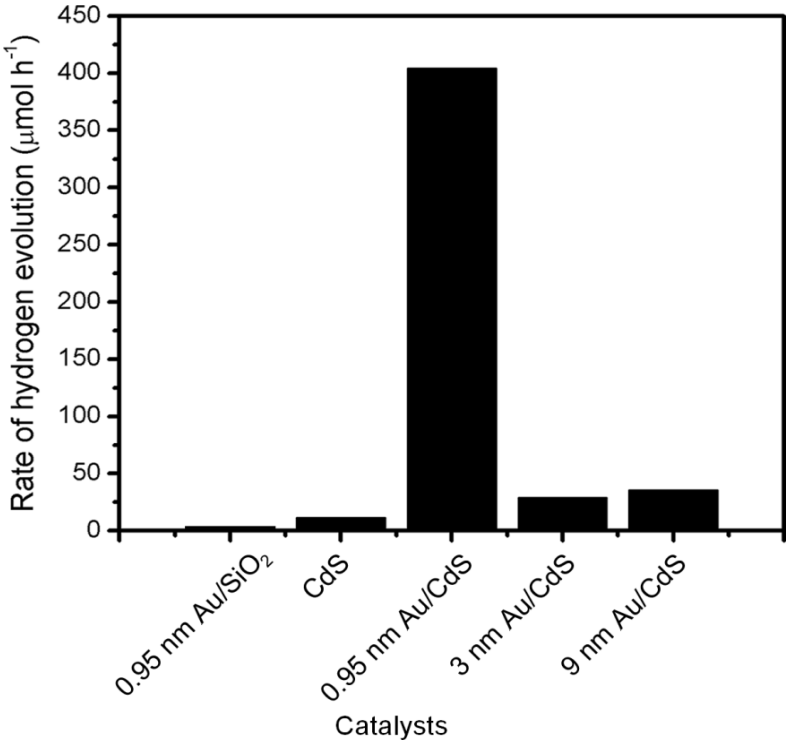

Figure 8-14 Hydrogen evolution rates for Au/CdS with different sizes of Au nanoparticles.

It is apparent that sub-nm Au modified CdS had about 11 times higher activity than that of the sample modified with 9 nm Au. The photocatalytic activity of sample modified with 3 nm Au was found to be comparable to that of 9 nm Au sample, confirming that sub-nm particles are indeed unique in their remarkable behavior. To confirm that Au nanoparticles themselves did not exhibit a photocatalytic activity, sub-nm Au particles (1 wt. %) were deposited on SiO_2, which is known to be inactive for water splitting reaction. No hydrogen evolution was observed for Au/SiO_2 composite catalyst. Although for larger metal particles a correlation between perimeter/surface area of metal nanoparticles and activity has been proposed [20, 21], that was done for larger particles exhibiting metallic properties. In our case, following the overly simplistic method used by Bowker [22] used for larger particles, the total perimeter of all sub-nm Au particles for the same Au loading was around 80 times longer than that of 9 nm Au, while the total surface area of sub-nm Au was around 9 times higher than that of 9 nm Au. However, the

fact that activity of 3 nm Au particles was almost the same as that of 9 nm particles, shows that a simple correlation between surface area and/or perimeter is not relevant in our case. This is understandable, given the appearance of DFT gap for smaller Au particles.

8.3.6 Photocatalytic activity of sub-nm Pt/CdS for hydrogen evolution

CdS loaded with different amount of sub-nm Pt NPs were investigated for photocatalytic activity in hydrogen evolution. Figure 8-15 shows the rates of hydrogen production of on sub-nm Pt/CdS with different amounts of Pt loadings.

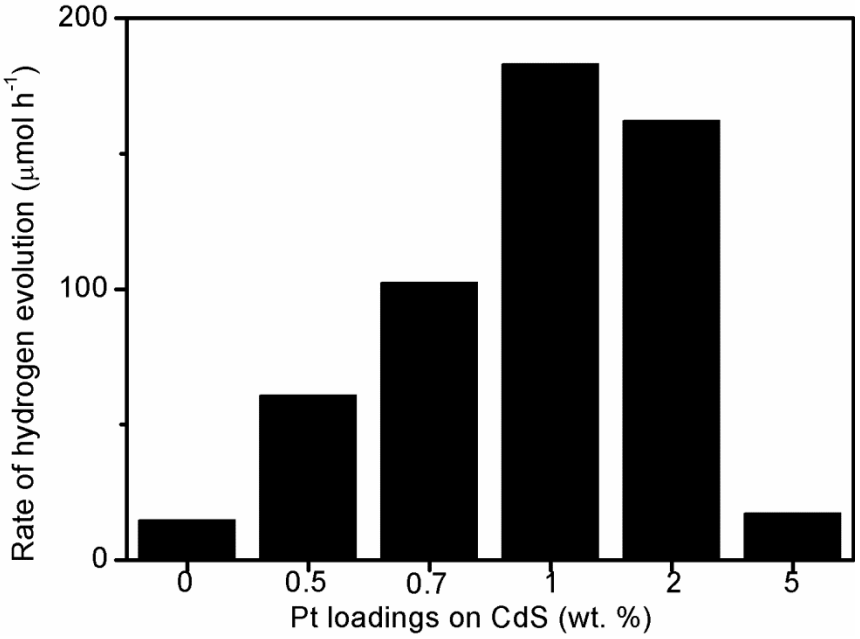

Figure 8-15 Rates of H_2 evolution on sub-nm Pt/CdS with different amounts of Pt loadings.

Sub-nm Pt NPs can largely enhance the hydrogen production rate of CdS. At 0.5 wt. % loading with sub-nm Pt NPs, the hydrogen production rate of CdS was 60.7 μmol•h^{-1}. The hydrogen production rate peaked at 183.0 μmol•h^{-1} when the loading amount of sub-nm Pt NPs was 1 wt. %. This amounts to enhancement factor of 15 times as compared to unmodified CdS (12 μmol•h^{-1}). Increasing the loading amount of sub-nm Pt NPs resulted a dramatic decrease in rate of hydrogen production, probably due to a reduction of the exposed surface area of CdS.

The most active sample, 1 wt. % sub-nm Pt/CdS was selected for long term stability test. Similar to the stability test for 1 wt. % sub-nm Au/CdS, 1wt. % sub-nm Pt/CdS sample was subjected to 3 hydrogen evolution/evacuation cycles (Figure 8-16).

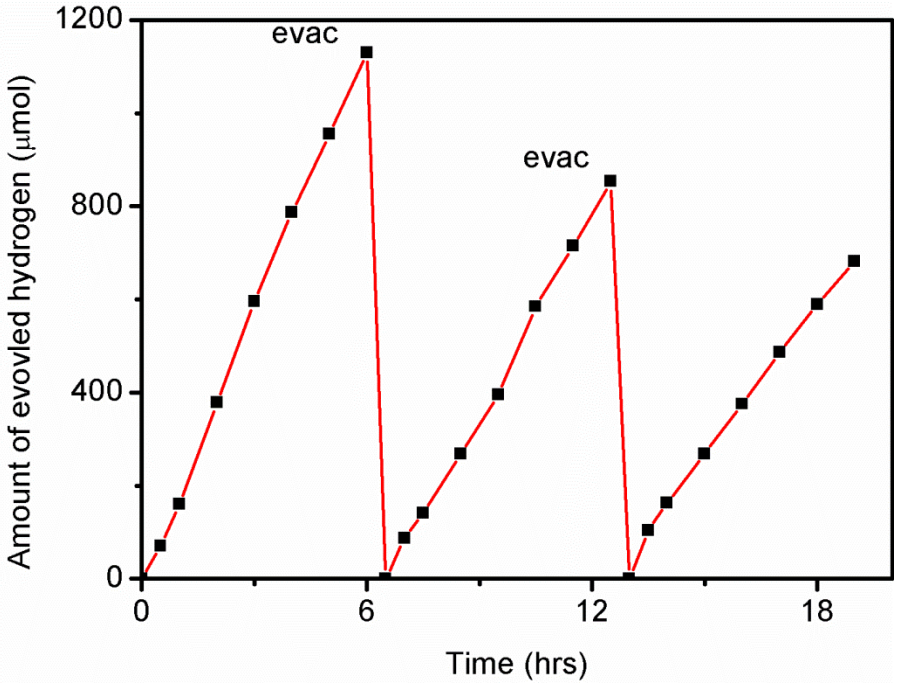

Figure 8-16 Stability test for 1 wt. % sub-nm Pt/CdS.

The sample showed relatively linear hydrogen production rate in the first 6 hours. However, the sample was not as robust as sub-nm Au/CdS. From the stability test, catalyst degradation was clearly observed. The average hydrogen production rate for the first 6 hours was 183.0 μmol•h^{-1}, and decreased to 142.2 μmol•h^{-1} in the second cycle finally reaching 113.6 μmol•h^{-1} in the third cycle. The reason for catalyst degradation might be attributed to agglomeration of sub-nm Pt NPs on CdS, however more studies are needed to clarify the mechanism for photocatalytic activity reduction.

8.3.7 Photocatalytic activity of regular size noble metals (Pt, Pd, Ru, Rh)/CdS for hydrogen evolution

Finally, to compare the activity of sub-nm Au with other co-catalysts, we have prepared CdS loaded with other noble metal co-catalysts. These included Pt, Ru, Pd and Rh modified CdS, where we kept a comparable co-catalyst loading (1 wt. %), which was also similar to the loading of the most active Au/CdS sample. As indicated earlier, the above-mentioned co-catalysts are known to promote H_2 evolution. To prepare these composite materials, we employed the same photodeposition method as the one we used to produce 3 nm Au nanoparticles modified CdS described above. Figure 8-17 to Figure 8-20 shows TEM characterizations and particle size

distributions of Pt/CdS, Ru/CdS, Pd/CdS and Rh/CdS samples. The average particle size of loaded co-catalysts ranged between 2.0 and 3.7 nm.

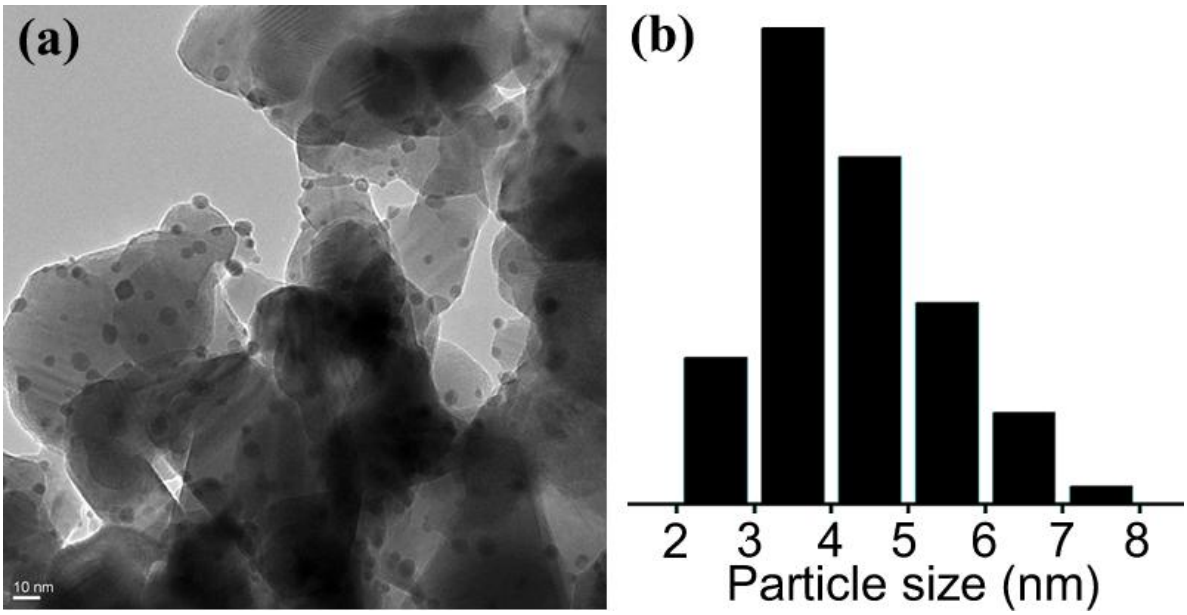

Figure 8-17 TEM image and size distribution of Pt nanoparticles. (a) TEM image; (b) Size distribution of Pt nanoparticles showing average particle size = 3.7 nm.

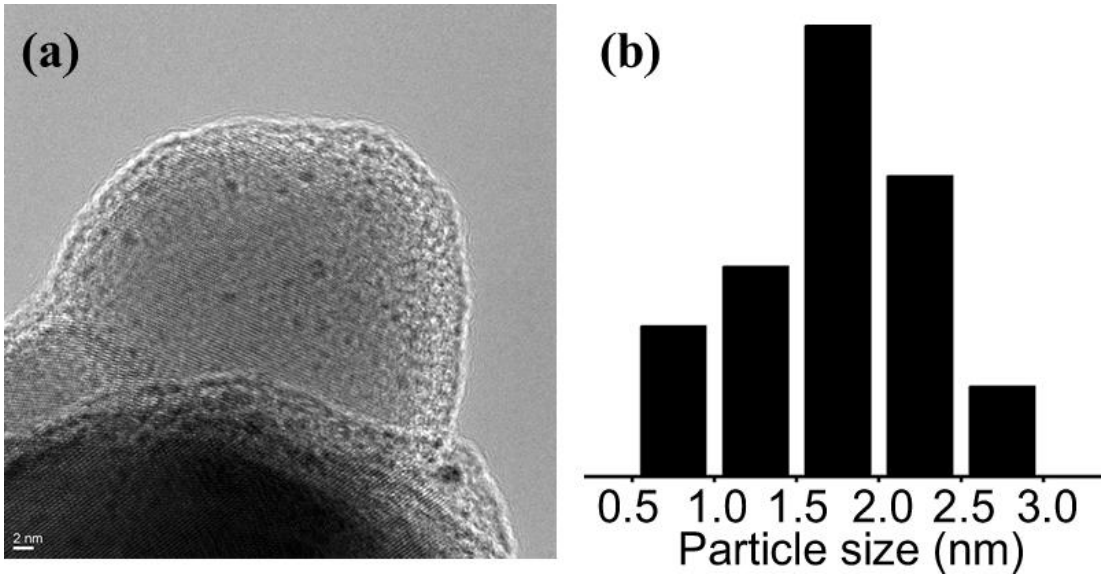

Figure 8-18 TEM image and size distribution of Ru nanoparticles. (a) TEM image; (b) Size distribution of Ru nanoparticles showing average particle size = 2.0 nm.

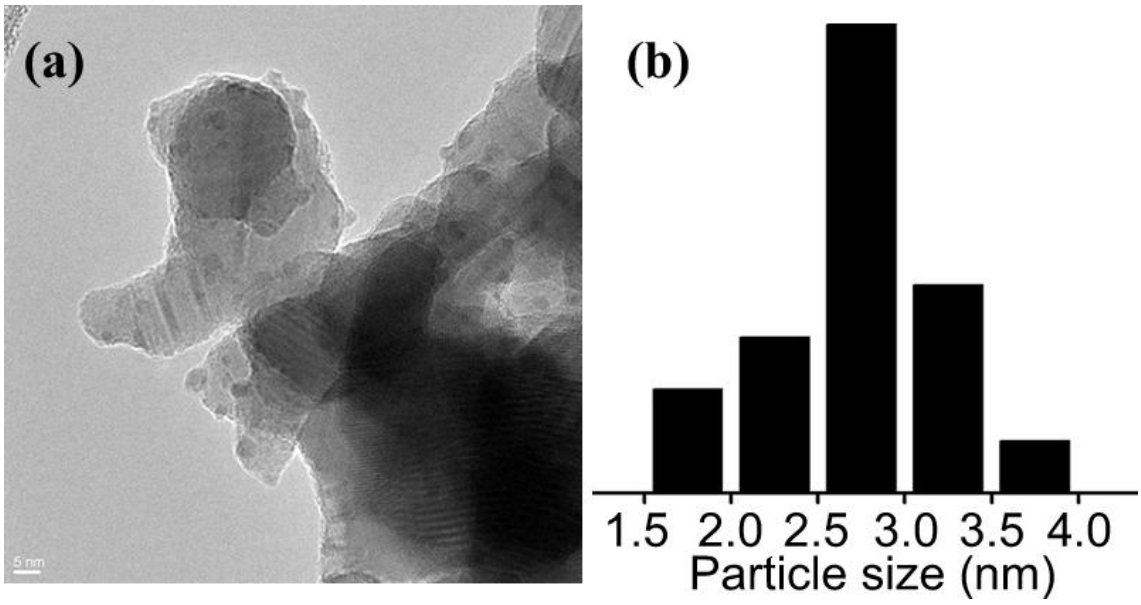

Figure 8-19 TEM image and size distribution of Pd nanoparticles. (a) TEM image; (b) Size distribution of Ru nanoparticles showing average particle size = 3.2 nm.

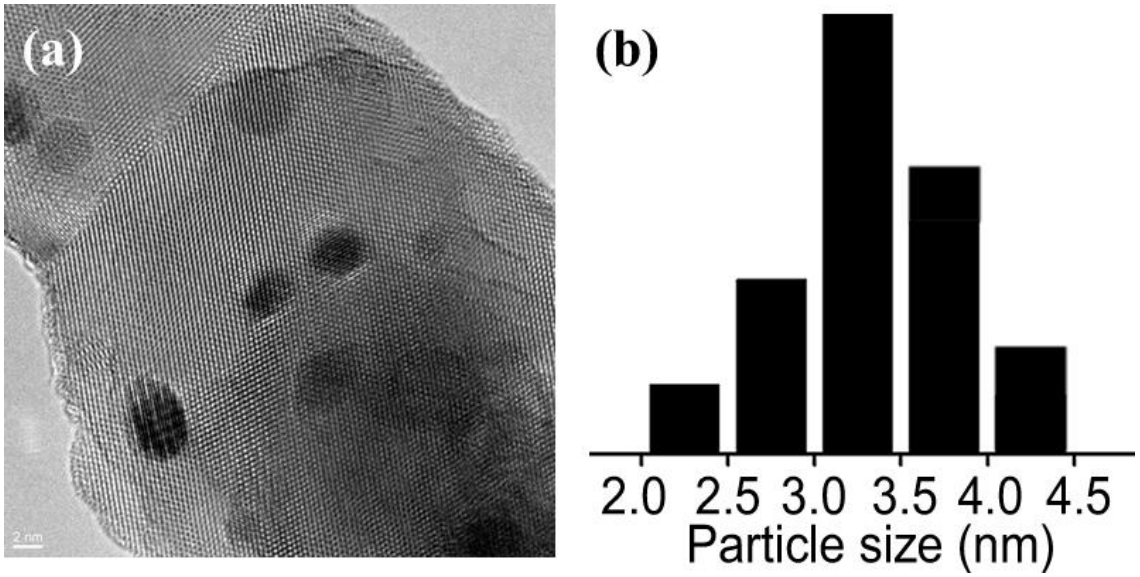

Figure 8-20 TEM image and size distribution of Rh nanoparticles. (a) TEM image; (b) Size distribution of Rh nanoparticles showing average particle size = 3.6 nm.

A comparison of H_2 evolution rates between these catalysts and 3 nm Au modified CdS showed that the activity of 3 nm Au was better than that of Pd/CdS and Rh/CdS, while Au/CdS activity being somewhat worse than that of Pt/CdS and Ru/CdS (Figure 8-21). A careful examination of CdS particle sizes for the above mentioned catalysts indicated that the CdS particle size remained the same despite undergoing various nanoparticles deposition, heat

treatment and washing procedures. This indicates the differences in catalytic behavior can be primarily attributed to co-catalysts.

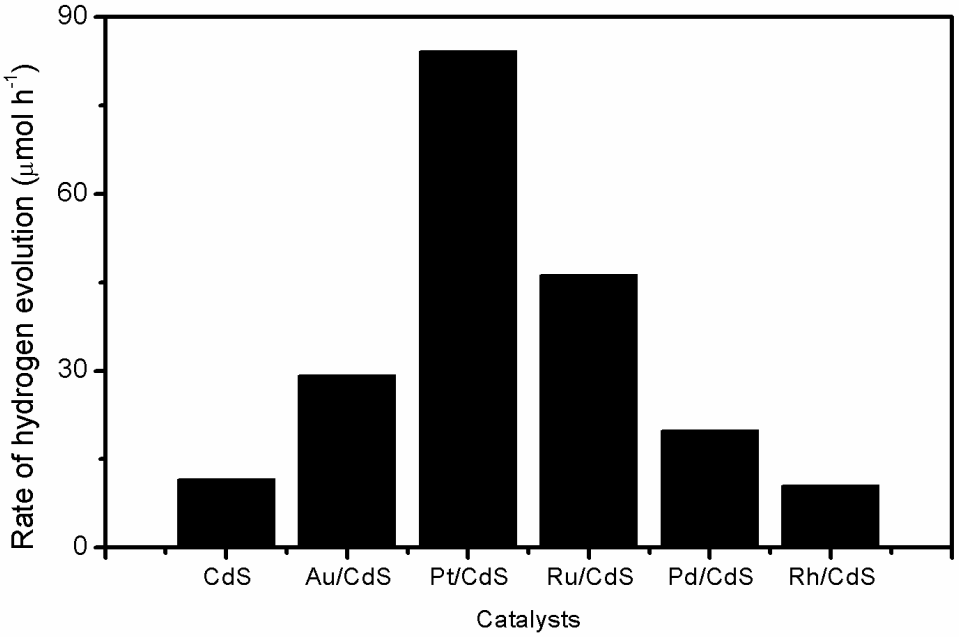

Figure 8-21 Rates of hydrogen production from different noble metal co-catalysts loaded on CdS. The average particle size of Au, Pt, Ru, Pd and Rh was 3.0 nm, 3.7 nm, 2.0 nm, 3.2 nm and 3.6 nm, respectively.

8.4 Discussion

The reason for striking photocatalytic activity of sub-nm co-catalysts is currently unknown, given a surprising absence of relevant literature on Au11 catalytic activity. For example, the observations of Au3-Au11 electrocatalytic activity for O_2 reduction do not have a significant relevance to this study [23]. Moreover, the known charge separation properties of larger Au nanoparticles in composite Au/CdS systems [24, 25] cannot be used to approximate the behavior of sub-nm Au particles described in this work, given the appearance of HOMO-LUMO gap for sub-nm particles. Although size-dependent shifts in the Fermi level were observed for Au nanoparticle deposited on TiO_2, where the transient absorption measurements were done for the Au particles sizes down to 5 nm [26, 27], this mechanism of enhancement can only partially account for enhancement of H_2 evolution of 3 nm Au modified CdS described in this paper and might not be applicable for smaller particles. The effects of localized surface plasmon resonance

(LSPR) for larger Au particles have been discussed in literature, however, the role of this mechanisms in catalytic activity of sub-nm clusters is unclear, given that such clusters are not metallic [28]. It is crucial to mention that both shape and electronic structure of supported Au particles can have profound effect on their catalytic activity. A charge on Au clusters can affect the work function of CdS surface and charge transfer mechanisms, ultimately affecting the overall activity for hydrogen production. The research on plasmon resonance in Au/CdS colloidal nanocomposites showed that the key optoelectronic properties of composite heterostructures comprising electrically coupled metal and semiconductor domains are significantly different from those weak inter-domain coupling systems [29]. It was indicated the quantum confinement of CdS was effectively decreased by charging of gold domains under illumination. Shape is also an important fact which contributes to the photocatalytic activity. The studies indicating a correlation between supported Au particle shape (2D and 3D) and particle charge were done on a limited number of oxides and they might not be directly applicable for the gold -metal sulfide composite semiconductor described here [30, 31]. Also, there are several studies on significant catalytic activity of 2D gold clusters due to presence of low coordinated Au atoms [32, 33] and our calculations described above indeed indicate a feasibility of both 2D and 3D geometry of the unsupported clusters. However, the importance of this phenomenon in photocatalysis needs further investigation, given that the published studies were not conducted for light-activated catalytic reactions. In order to clarify the remarkable activity of small Au nanoparticles, work is currently underway to investigate the energy level alignment and possible charge transfer process at the interface of deprotected Au nanoparticles and the CdS substrate. Moreover, additional experiments to explore photocatalytic properties of other metals synthesized in sub-nm form, for example, sub-nm Pt and sub-nm Pd, are currently in progress.

References

[1] K. Maeda, K. Domen, Photocatalytic water splitting: Recent progress and future challenges, J Phys Chem Lett, 1 (2010) 2655-2661.

[2] Z.G. Zou, J.H. Ye, K. Sayama, H. Arakawa, Direct splitting of water under visible light irradiation with an oxide semiconductor photocatalyst, Nature, 414 (2001) 625-627.

[3] H.G. Kim, D.W. Hwang, J.S. Lee, An undoped, single-phase oxide photocatalyst working under visible light, J. Am. Chem. Soc., 126 (2004) 8912-8913.

[4] H. Park, W. Choi, M.R. Hoffmann, Effects of the preparation method of the ternary $CdS/TiO_2/Pt$ hybrid photocatalysts on visible light-induced hydrogen production, J. Mater. Chem., 18 (2008) 2379-2385.

[5] I. Tsuji, H. Kato, A. Kudo, Visible-light-induced H_2 evolution from an aqueous solution containing sulfide and sulfite over a $ZnS\text{-}CuInS_2\text{-}AgInS_2$ solid-solution photocatalyst, Angew Chem Int Edit, 44 (2005) 3565-3568.

[6] H. Kaga, K. Saito, A. Kudo, Solar hydrogen production over novel metal sulfide photocatalysts of $AGa_2In_3S_8$ (A = Cu or Ag) with layered structures, Chem Commun, 46 (2010) 3779-3781.

[7] X. Zong, H.J. Yan, G.P. Wu, G.J. Ma, F.Y. Wen, L. Wang, C. Li, Enhancement of photocatalytic H_2 evolution on CdS by loading MOS_2 as cocatalyst under visible light irradiation, J. Am. Chem. Soc., 130 (2008) 7176.

[8] C. Li, X. Zong, J.F. Han, G.J. Ma, H.J. Yan, G.P. Wu, Photocatalytic H_2 evolution on CdS loaded with WS_2 as cocatalyst under visible light irradiation, J Phys Chem C, 115 (2011) 12202-12208.

[9] K. Maeda, K. Teramura, D.L. Lu, N. Saito, Y. Inoue, K. Domen, Roles of Rh/Cr_2O_3 (core/shell) nanoparticles photodeposited on visible-light-responsive $(Ga_{1-x}Zn_x)(N_{1-x}O_x)$ solid solutions in photocatalytic overall water splitting, J Phys Chem C, 111 (2007) 7554-7560.

[10] K. Maeda, K. Teramura, D.L. Lu, N. Saito, Y. Inoue, K. Domen, Noble-metal/Cr_2O_3 core/shell nanoparticles as a cocatalyst for photocatalytic overall water splitting, Angew Chem Int Edit, 45 (2006) 7806-7809.

[11] A. Iwase, H. Kato, A. Kudo, Nanosized Au particles as an efficient cocatalyst for photocatalytic overall water splitting, Catal Lett, 108 (2006) 6-9.

[12] G.L. Chiarello, L. Forni, E. Selli, Photocatalytic hydrogen production by liquid- and gas-phase reforming of CH_3OH over flame-made TiO_2 and Au/TiO_2, Catal. Today, 144 (2009) 69-74.
[13] O. Rosseler, M.V. Shankar, M.K.L. Du, L. Schmidlin, N. Keller, V. Keller, Solar light photocatalytic hydrogen production from water over Pt and Au/TiO_2(anatase/rutile) photocatalysts: Influence of noble metal and porogen promotion, J Catal, 269 (2010) 179-190.
[14] Y.W. Tai, J.S. Chen, C.C. Yang, B.Z. Wan, Preparation of nano-gold on $K_2La_2Ti_3O_{10}$ for producing hydrogen from photo-catalytic water splitting, Catal. Today, 97 (2004) 95-101.
[15] S. Zhao, G. Ramakrishnan, D. Su, R. Rieger, A. Koller, A. Orlov, Novel photocatalytic applications of sub-nanometer gold particles for environmental liquid and gas phase reactions, Appl Catal B-Environ, 104 (2011) 239-244.
[16] M.F. Bertino, Z.M. Sun, R. Zhang, L.S. Wang, Facile syntheses of monodisperse ultrasmall Au clusters, J Phys Chem B, 110 (2006) 21416-21418.
[17] J.C. Idrobo, W. Walkosz, S.F. Yip, S. Ogut, J. Wang, J. Jellinek, Static polarizabilities and optical absorption spectra of gold clusters (Au_n, n=2-14 and 20) from first principles, Phys Rev B, 76 (2007).
[18] D. Meissner, R. Memming, B. Kastening, Photoelectrochemistry of cadmium-sulfide .1. reanalysis of photocorrosion and flat-band potential, J Phys Chem-Us, 92 (1988) 3476-3483.
[19] A. Kudo, Y. Miseki, Heterogeneous photocatalyst materials for water splitting, Chem. Soc. Rev., 38 (2009) 253-278.
[20] G.P. Wu, T. Chen, W.G. Su, G.H. Zhou, X. Zong, Z.B. Lei, C. Li, H_2 production with ultra-low CO selectivity via photocatalytic reforming of methanol on Au/TiO_2 catalyst, Int J Hydrogen Energ, 33 (2008) 1243-1251.
[21] P.K. He, J.J. Yang, D.M. Xang, X.H. Wang, M. Zhang, Photocatalytic decomposition of gaseous ozone on Au/TiO_2, Chinese J Catal, 27 (2006) 71-74.
[22] M. Bowker, D. James, P. Stone, R. Bennett, N. Perkins, L. Millard, J. Greaves, A. Dickinson, Catalysis at the metal-support interface: exemplified by the photocatalytic reforming of methanol on Pd/TiO_2, J Catal, 217 (2003) 427-433.
[23] M. J Rodriguez-Vazquez, M.C. Blanco, R. Lourido, C. Vazquez-Vazquez, E. Pastor, G.A. Planes, J. Rivas, M.A. Lopez-Quintela, Synthesis of atomic gold clusters with strong electrocatalytic activities, Langmuir : the ACS journal of surfaces and colloids, 24 (2008) 12690-12694.

[24] W.-W. Zhao, J. Wang, J.-J. Xu, H.-Y. Chen, Energy transfer between CdS quantum dots and Au nanoparticles in photoelectrochemical detection, Chem Commun, 47 (2011) 10990-10992.
[25] W.-T. Chen, T.-T. Yang, Y.-J. Hsu, Au-CdS Core-Shell Nanocrystals with Controllable Shell Thickness and Photoinduced Charge Separation Property, Chemistry of Materials, 20 (2008) 7204-7206.
[26] V. Subramanian, E.E. Wolf, P.V. Kamat, Catalysis with TiO_2/gold nanocomposites. Effect of metal particle size on the Fermi level equilibration, J. Am. Chem. Soc., 126 (2004) 4943-4950.
[27] B.Z. Tian, J.L. Zhang, T.Z. Tong, F. Chen, Preparation of Au/TiO_2 catalysts from Au(I)-thiosulfate complex and study of their photocatalytic activity for the degradation of methyl orange, Appl Catal B-Environ, 79 (2008) 394-401.
[28] T. Torimoto, H. Horibe, T. Kameyama, K. Okazaki, S. Ikeda, M. Matsumura, A. Ishikawa, H. Ishihara, Plasmon-enhanced photocatalytic activity of cadmium sulfide nanoparticle immobilized on silica-coated gold particles, J Phys Chem Lett, 2 (2011) 2057-2062.
[29] E. Khon, A. Mereshchenko, A.N. Tarnovsky, K. Acharya, A. Klinkova, N.N. Hewa-Kasakarage, I. Nemitz, M. Zamkov, Suppression of the plasmon resonance in Au/CdS colloidal nanocomposites, Nano Lett, 11 (2011) 1792-1799.
[30] T. Risse, S. Shaikhutdinov, N. Nilius, M. Sterrer, H.J. Freund, Gold supported on thin oxide films: from single atoms to nanoparticles, Accounts of chemical research, 41 (2008) 949-956.
[31] M.A. Brown, F. Ringleb, Y. Fujimori, M. Sterrer, H.-J. Freund, G. Preda, P. Gianfranco, Initial formation of positively charged gold on MgO(001) thin films: Identification by experiment and structural assignment by theory, J. Phys. Chem. C, 115 (2011) 10114-10124.
[32] M.S. Chen, D.W. Goodman, The structure of catalytically active gold on titania, Science, 306 (2004) 252-255.
[33] M. Valden, X. Lai, D.W. Goodman, Onset of catalytic activity of gold clusters on titania with the appearance of nonmetallic properties, Science, 281 (1998) 1647-1650.

Chapter 9

Concluding Remarks and Future Work

9.1 Concluding remarks

There is a pressing need to develop new alternatives to fossil fuels, which can address the future energy needs. Using water as sustainable source of fuel, solar light and catalysts can be such an alternative, given that we can increase the quantum efficiency of the process. This dissertation has focused on development of new photocatalysts for photocatalytic hydrogen production leading to eventual goal of efficient water splitting to hydrogen and oxygen. The main strategies to develop a visible light driven photocatalyst for photocatalytic water splitting and/or hydrogen evolution were focused on co-catalyst development and bandgap tuning via doping. Co-catalyst loading is a widely used technique for photocatalytic activity enhancement. Noble metal co-catalysts have attracted a lot of attention in the recent decades. Recent studies have revealed noble metal co-catalysts not only can lower the activation energy and serve as active sites for increased activity, but also can result in other phenomena facilitating catalytic reactions, such as appearance of surface plasmon resonance and enhanced interactions with the reactants. This study has introduced a new concept of sub nanometer noble metal co-catalysts for enhancement of photocatalytic activity. The results described in this dissertation revealed that sub nanometer noble metal nanoparticles can enhance the photocatalytic activity for hydrogen evolution under visible light irradiation by more than an order of magnitude (35 times). These are very exciting and novel results which have never been described in literature. The fundamental mechanisms explaining such an enhancement still need to be development, which can be a focus of a future work. In addition to using CdS as a standard photocatalyst we also used more advanced approaches to develop perovskite based materials. In this work we have successfully introduced polymerizable complex method to synthesize perovskite structure materials. Perovskite structure materials are well known for their long stability, good photo responses, easy synthesis and relatively low cost. $SrTiO_3$ is one of the most representative ones. However, the wide bandgap of $SrTiO_3$ limited its photocatalytic applications under visible light. Utilizing Rh doping, the absorbance edge was shifted to visible region, allowing activation of the catalyst by visible light irradiation. In comparison with several standard methods of making doped materials, we found that $SrTiO_3$: Rh synthesized by polymerizable complex had smaller nanoparticle sizes and higher photocatalytic activity in hydrogen evolution compared to conventional synthesis methods. In order to understand the role of physicochemical parameters on photocatalytic activity, the samples were characterized by various methods. We also studied

the effects of sample preparation conditions on photocatalytic activity where we linked samples' physicochemical parameters to their catalytic activities.

9.2 Future challenges

This dissertation has made a significant progress in designing better catalysts. However, many challenges still remain in this field. Firstly, design of photocatalysts which have good electron-hole separation characteristic and provide proper sites for both reduction and oxidation reactions remains challenge. Although considerable progress has been made to enhance the photocatalytic activity in water splitting and hydrogen evolution, a successful photocatalyst has not been yet developed (QE > 10% under visible light). Chemical composition, particle size, interface characteristics and co-catalyst selection need to be considered comprehensively in design of photocatalysts for water splitting and hydrogen evolution. Chemical composition determines the light absorbance edge and photo response of a semiconductor. To effectively utilize visible light, the bandgap of the semiconductor needs to be less than 3.0 eV and the over potentials of hydrogen reduction reaction and water oxidation need to be satisfied simultaneously for overall water splitting. This requires a careful examination of different elements in photocatalyst design. The interfacial characteristics are critical for electron-hole pair separation and recombination, particularly under the highly corrosive conditions of photochemical reactions. Co-catalysts can improve the photocatalytic activity, however, they can also be recombination centers of photogenerated electron-hole pairs and promote back reactions. It is desirable to design co-catalysts for reduction reaction and oxidation reaction separately and minimize these negative effects. Unfortunately, previous efforts to optimize one consideration of as discussed above always introduced in other new challenges. New strategies and new methods are clearly needed to construct novel heterogeneous photocatalysts with ideal optical absorption, efficient carrier generation and separation, and rapid hydrogen and oxygen evolution on the surface of the photocatalysts. To achieve this, more systematic investigations and further efforts on photocatalyst development will be valuable.

Secondly, a fundamental understanding of surface and interface characteristics is essential for the optimization of photocatalysts and co-catalysts. For example, understanding the bonding structures between co-catalysts and semiconductor can provide conceptions of charge transfer and transport behaviors. Particle sizes and shapes of the co-catalysts need to be considered because they can largely affect the active facets. Interface characteristics of heterostructure

semiconductors can influence charge generation, separation and transportation. Thus, more efforts in computational and theoretical calculations are needed to solve these fundamental challenges. The detailed mechanism studies are necessary to further actuate this field.

Thirdly, stability is and will be one main challenge for photocatalyst development. A photocatalyst with very high efficiency is still useless if the lifetime of the catalyst is too short. For majority systems, chemical corrosion and/or photodegradation of photocatalysts are difficult to avoid. The extended photocatalyst stability has only been achieved in a few examples to date, which however often requires highly complicated synthetic processes. To develop a stable photocatalytic system with high efficiency and low-cost will be the central task to realize a practically viable photocatalyst for solar fuel production.